平成 26 年度博士論文

Characteristics of epithermal Au and porphyry Cu-Mo mineralizations of the Chatree deposit, central Thailand

タイ国中部チャットリー金鉱床の浅熱水性金鉱化作用と斑岩銅-モリブデン鉱化作用の特徴

タンワッタナヌクン　ラダ-

Tangwattananukul Ladda

博士工　9512002

秋田大学大学院

工学資源学研究科博士後期課程

資源学専攻

ABSTRACT

The Chatree Au-Ag deposit in Petchabun Province, in the central Thailand is an epithermal vein-type deposit in Triassic age. The size and vertical extension of area of gold mineralization is almost 3 km long, 1.5 km wide and 200 m deep. The total production from 2001 to 2013 was 40 tons of gold and 180 tons of silver. Two mineralization styles that are epithermal Au-Ag and porphyry Cu-Mo mineralization are present in the Chatree mining area. Epithermal Au-Ag deposit, such as the Q prospect and A, C, H, D, Kw and Ke pits of the Chatree deposit, is distributed from north to central part. On the other hand, Cu-Mo mineralization is recognized in the N and V prospects in the southern part of the Chatree deposit.

Geology around the Chatree epithermal gold deposit is composed of volcanic and sedimentary rocks ranging from Carboniferous through Permian to Triassic. The sedimentary strata of Carboniferous and Permian ages are thought to be present in deeper part of the Chatree deposit. The geology of the Chatree deposit mainly consists of andesite and rhyolite volcanics. The andesitic volcanic rocks are dominant at the lower part of volcanic succession, which includes monomictic andesitic breccia, polymictic andesitic breccia and volcanic sedimentary breccia in ascending order. The rhyolitic tuff unconformably overlies the andesitic volcanic succession. The Au-bearing quartz veins of the Chatree deposit are mainly hosted in polymictic andesitic breccia and volcanic sedimentary breccia.

The Au-bearing quartz vein is characterized by veins, veinlets and network-type veins consisting of large amounts of quartz and calcite with small amounts of illite, adularia, chlorite and sulfide minerals. Based on crosscutting relationships of the Au-bearing quartz veins of the A pit and the Q and B prospects, the Au-bearing quartz veins are classified into

five stages. Quartz veins of Stage 1 and network-type veins of Stage 4 at A pit and the Q and B prospects are characterized by intense gold mineralization. The quartz veins containing electrum are characterized by microcrystalline and flamboyant textures that suggest rapid crystal growth from supersaturated hydrothermal solution. Coexistence of laumontite and illite in the Au-bearing quartz vein of Stage Q4 at the Q prospect suggests that the Au-bearing quartz vein of Stage Q4 was formed about 200^0C. Occurrence of boiling is suggested in the Au-bearing quartz veins of Stage Q4 based on the presence of flamboyant texture and higher oxygen isotopic ratio of quartz (15.0‰). The total pressure of formation of the Au-bearing quartz veins of Stage Q4 at the Q prospect is estimated to be approximately 20 bars. The Au-bearing quartz vein of the Q prospect was formed about 200 m below the paleosurface.

Cu-Mo mineralization is present in granodiorite porphyry and andesitic volcanic rocks of the N and V prospects at the southern part of the Chatree deposit. The Cu-Mo mineralization took place about 5 Ma (244±1 Ma) later than epithermal gold deposit (250±1 Ma). The quartz veins of Cu-Mo mineralization consist of a large amount of quartz with small amounts of chlorite, pyrite, chalcopyrite, molybdenum and pyrrhotite. Fluid inclusions of the Cu-Mo mineralization can be divided into liquid-rich two phases fluid inclusion (1 wt% NaCl eq.) and multiphase solid-bearing fluid inclusions (30-44 wt% NaCl eq.). The assemblages of the fluid inclusions are consistent with the assemblage of vapor and fluid after phase separation of magmatic fluid. These conditions the halite-bearing fluid inclusion at the N prospect is thought to be 420 bars at the temperature 450^0C. Cu-Mo-bearing quartz veins took place at 1 km below the paleosurface.

The $^{87}Sr/^{86}Sr$ ratios of least altered andesite lava, strongly altered andesite lava and quartz veins were examined in the Au-mineralization. The strongly altered andesite lavas

(0.707070-0.708765) near the Au-bearing quartz veins have higher initial $^{87}Sr/^{86}Sr$ ratios than least altered andesite lava (0.705118-0.705309). The initial $^{87}Sr/^{86}Sr$ ratios of the strongly altered andesite suggest that the hydrothermal solution forming the altered andesite lavas has higher $^{87}Sr/^{86}Sr$ ratios.

The Au-bearing quartz veins and barren calcite veins have different initial $^{87}Sr/^{86}Sr$ ratios. The initial $^{87}Sr/^{86}Sr$ ratios of the Au-bearing quartz veins of Stage 1 (0.706949) and network-type veins of Stage 4 (0.708254-0.717607) are higher than those of calcite veins of Stage 5 (0.704843-0.705146). There is a possibility that the hydrothermal system forming the Au-bearing quartz veins is different from the hydrothermal system forming barren calcite vein in later stage in the Chatree deposit. The initial $^{87}Sr/^{86}Sr$ ratios of the Au-bearing network-type veins of Stage 4 and the strongly altered andesite lava at the A pit and Q prospect are similar to initial $^{87}Sr/^{86}Sr$ ratios sedimentary and metamorphic rocks. The fact suggests that the hydrothermal solution association with Au-mineralization reacted with sedimentary strata in deeper part in the Chatree area.

The Au-bearing quartz veins and altered andesite volcanics formed immediately after formation of new fracture tend to have higher $^{87}Sr/^{86}Sr$ ratios. This tendency suggests that Au-bearing hydrothermal solution stored in deeper section of the Chatree deposit, under high pressure condition and also reacted with sedimentary strata of Carboniferous and/or Permian. Then the hydrothermal solution in the deeper section was intermittently transported to the shallow section as a result of development of fissures. Structural control such as the development of fissure from deeper to shallower sections is one of important factor for the formation of Au mineralization in the Chatree deposit in addition to presence of source of gold.

TABLE OF CONTENTS

LIST OF FIGTURES

LIST OF TABLES

Chapter 1: Introduction

1.1 Introduction

Epithermal Au deposit can be classified high sulfidation and low sulfidation. Epithermal ore and porphyry ore deposits related with magmatism are thought to be formed in upper crust by fluid such as of magmatic origin (Hedenquist and Lowensten, 1994; Hedenquist et al., 1998) and meteoric water (Seal and Rye, 1992). High-sulfidation epithermal deposits and porphyry deposits show a close spatial and temporal relationship (Sillitoe, 1983; Hedenquist et al., 1998). These deposits have genetic link associated with processes of phase separation between hypersaline liquids and vapor at high temperatures and during subsequent cooling (Heinrich, 2005). However, the evidence of association of magmatic components with low-sulfidation epithermal ore deposit is elusive.

The Chatree Au-Ag deposit in Thailand is one of low-sulfidation epithermal Au deposit in the Southeast Asia (Salam et al., 2013; Tangwattananukul et al., 2014). The Chatree mining area is located in central part of the Loei-Phetchabun-Nakorn Nayok volcanic belt. Ore deposit in the volcanic belt consists of Cu-Au skarn, porphyry Cu-Au and epithermal Au deposit from Laos through Thailand to Cambodia. The Chatree gold deposit is located in Phetchabun Province, central Thailand about 300 km north of Bangkok (Fig. 1.1). The mineralized area of the gold deposit is about 7.5 km by 2.5 km (Fig. 1.2). The total amount of metal at the Chatree deposit has been estimated to be 156 tons of gold and 1089 tons of silver based on data for the total amount of ore (145 Mt) with average grades of 1.07 g/t Au and 7.5 g/t Ag (Lunwongsa et al., 2010). The aim of this study is to elucidate the formation environment and evolution of the hydrothermal system of epithermal Au and Cu-Mo mineralization deposits in the Chatree deposit.

1.2 Discovery and development

Gold has been found in Thailand for many centuries. Placer gold occurs in alluvium and weathering residuum. The primary gold is found in several parts of Thailand such as Phetchabune, Loei and Lopburi provines. Folk-lore describes colluvium and alluvial gold workings by the Japanese during World War II in areas to the east and south of the present day Chatree mine (Diemar and Diemar, 1999). However, systematic exploration did not occur until 1987 after the Thailand Government allowed foreign enterprises to survey for gold. The Thai Goldfields Limited team, a wholly owned subsidiary of Epoch Mining NL explored along the Loei-Phetchabun belt for porphyry copper and related epithermal gold mineralization from 1987 to 1993. Exploration methods include mapping, panning, soil sampling, trenching, auger drilling and diamond core drilling. Gold was firstly recorded at Khao Mo (presently A pit in the Chatree mining area) in Phetchabune province, central part of the Thailand (Fig. 1.2). The Khao Mo prospect was recognized as a high-potential area of epithermal gold mineralization. The characteristics of mineralized veins are banded colloform and crustiform veins.

During 1991 and 1992, Department of Mineral Resources (DMR) prospected for gold in the Chatree district by conducting soil sampling and electromagnetic conductivity surveys (De Little, 2005). In 1992, Kingsgate Limited (Ltd.) acquired Thai Gold field Ltd. from Epoch Mining NL and formed the wholly owned Akara Mining Ltd which then conducted grid based auger laterite geochemical survey in 1996, leading to the discovery of ores in C, D, H and J vein zones, which are presently being mined (James and Cumming, 2007). Construction proceeded smoothly in the following few years and mining was commenced in early 2001. Since commissioning of the Chatree Mining Complex in 2001 to 2013, the mining has produced over 1.3 million Oz of gold and over 5.8 million Oz of silver.

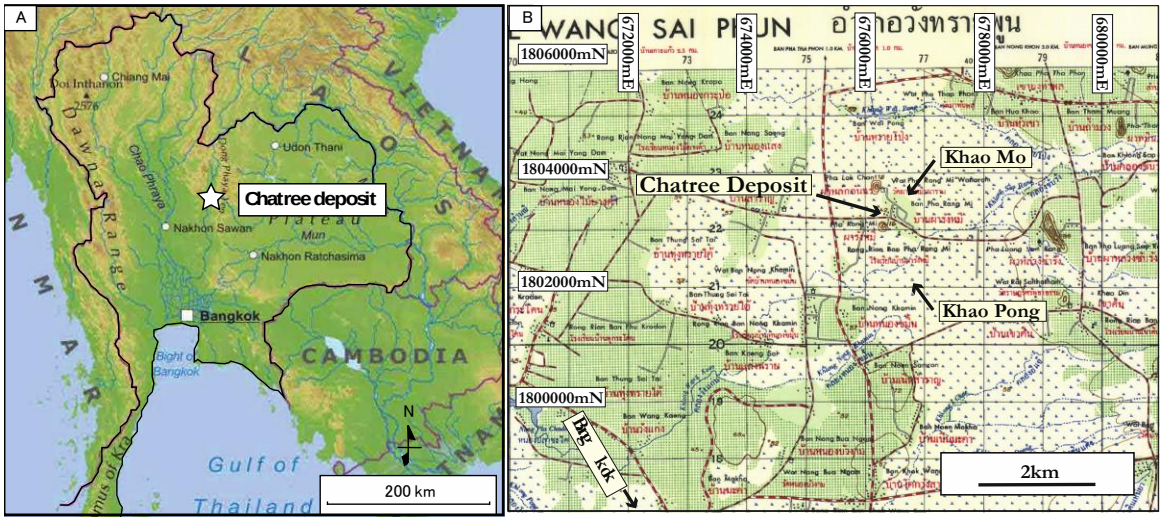

Figure 1.1 (A) Index map of Thailand showing location of study area in the Chatree deposit, central part of Thailand. (B) Topographic map showing the location of the Chatree deposit, Khao Mo (North) and Khao Pong (South).

The Chatree mine was well known as one of the lowest production cost gold mines in the world, due to a number of favorable factors such as excellent access, an existing power line across the property, cheap labor and the shallow depth of mining activity. The Chatree mine is composed of Q, A, A-East, C, K, H-West, K, K-West, P, J, S and D pits.

1.3 **Previous works**

Gatinsky (1978), Bunopas (1991) and Bunopass and Vella (1983) clarified the geologic history of Thailand based on plate tectonic models. They concluded that Thailand consists of two separate micro-continents, the Shan-Thai and the Indochina Terranes, which were cratonic fragments of Gondwana in the Precambrian to Lower Paleozoic. During the Middle Paleozoic to Lower Triassic, Shan-Thai and Indochina terranes were rifted into the Paleo Thethys Ocean. These terranes moved closer together until later suturing occurred.

Barr and McDonald (1991) introduced tectonostratigraphic terranes to determine an early Mesozoic tectonic model for Thailand. They proposed the existence of a fold belt; the so-called Sukhothai fold belt, separating the Shan-Thai and the Indochinian (Indochina) terranes. These blocks have collided together along the Nan-Uttaradit-Sra Kaeo suture.

Metcalfe (1996) and Charusiri (2002) proposed that the Indochina and Shan-Thai terranes rifted and separated from Gondwana during three episodes; Devonian, the Late-Early Permian and the Late Triassic-Late Jurassic. Tethyan oceanic basin opened during the rifting. Southeast Asia was bounded by suture zones that represent the remnants of various Tethyan basins by strike slip faults. The Shan-Thai and Indochina were believed to have been separated by the Paleo-Tethys Ocean, which opened in the Middle-Late Devonian and closed during the Triassic.

Cumming (2006) undertook a project on the geology, mineralogy, geochemistry of the Chatree gold deposit. Rock units were separated into four stratigraphic units; fiamme breccia, epiclastic and volcaniclastic sedimentary, polymictic and monomictic andesitic

breccia and andesite. Salam et al. (2008) proposed that gold mineralization consists of five stages gold-bearing mineralization including quartz-carbonate- (K-feldspar) -chlorite-epidote veins (stage 2) and quartz-calcite veins (stage 4). The $\delta^{18}O$ values of the Chatree ore fluid range between -1 and +6‰ suggesting that the ore-bearing hydrothermal fluid overlaps with both meteoric and magmatic compositions. Salam (2008) suggested that the gold mineralization at the Chatree was related to water-rock interaction and mixing of meteoric and magmatic fluids. The $\delta^{18}O$ values from quartz-calcite veins of the stage 2 range from +8.1‰ to +12.3‰. The lowest oxygen isotope values of quartaz are spatially more and less confined to the prominent structure in the center of the major ore zone.

Mori et al. (2009) studied the chemical composition of volcanic rocks and gold mineralization. They proposed that andesite and granodiorite are derived from the same magma source. Ore-forming fluids could be the mixture of Mg- and CO_2-rich of low temperature and low salinity meteoric water with magmatic fluid of higher temperatures and high salinity.

Salam et al. (2013) suggested that the volcanic sequence is subdivided into four stratigraphic units and two volcanic suites. The Late Permian Suite 1 volcanic unit was sourced from a more depleted mantle compared to the overlying Early Triassic Suite 2 volcanic units. Suite 1 units were probably formed immediately after the beginning of subduction and the creation of a new island arc. Early Triassic Suite 2 units were erupted during ongoing subduction when the system had achieved a steady state. The Chatree gold mineralization occurred during the switch between the two mantle sources and this switch of magma source is marked by a mixed volcano-plutonic magmatism at the Permo-Triassic boundary.

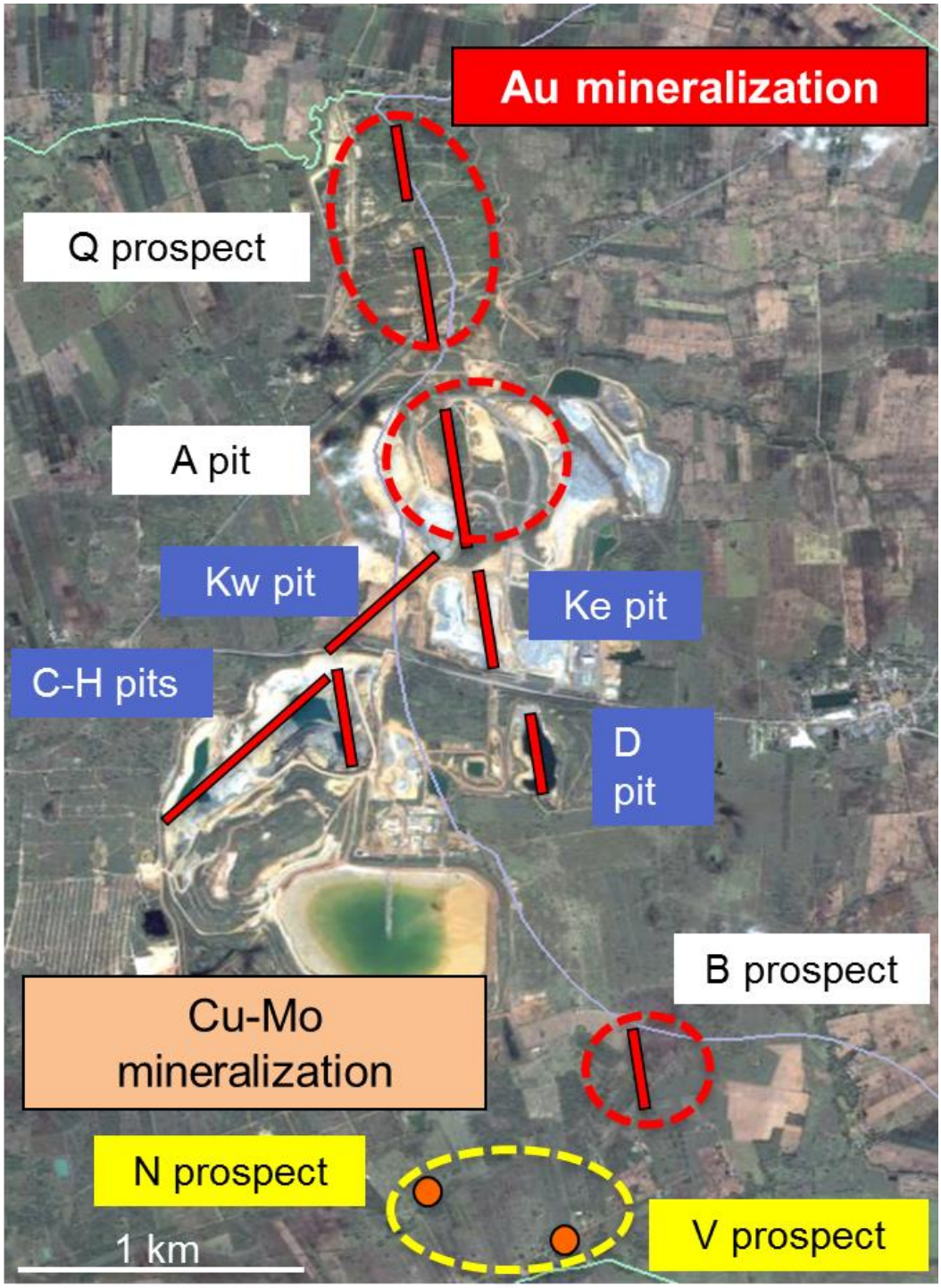

Figure 1.2 There are several open pits and prospects. Au-mineralization is mainly formed in the central to northern parts of the deposit. Cu-Mo mineralization is recognized in the southern parts such as the N and V prospects.

1.4 Aims

The aim of this study was to elucidate the style of Au mineralization and Cu-Mo mineralization and to estimate the formation condition including temperature and depth of the Au-bearing quartz veins and Cu-Mo-bearing quartz veins of the Chatree deposit based on data of classification of mineralization stages, mineral assemblage, textures of quartz and oxygen isotopic ratios of quartz.

More specific aims were to elucidate if there is a genetic relationship between epithermal Au and Cu-Mo mineralization deposits in the Chatree area, and characterize of andesite lava, granodiorite and the Au-bearing quartz veins. The purposed of this project was also to understand the evolution of the hydrothermal system.

Chapter 2: Geology

2.1 Geologic setting

The Loei-Phetchabun-Nakorn Nayok volcanic belt (Jungyasuk and Kositanont, 1992; Charusiri, 2002) (Fig. 2.1) was formed during and prior to the closure of Tethys (Meltcalfe, 2006) and modified during the extension of SE Asia during the collision of India and Eurasia (Barr and McDonald, 1991). The Loei-Phetchabun -Nakorn Nayok volcanic belt is thought to have been originated as a result of the northward subduction of a large oceanic basin (Paleo-Thethys) beneath the Indochina Terrane during the Late Permian and Triassic (Intasopa, 1992; Metcalfe, 1996). The closure of this oceanic basin is thought to be caused by the northwards drift of the Shan Thai terrane and eventual collision with Indochina (Metcalfe, 2006).

Both the Shan-Thai and Indochina Terranes are thought to be allochthonous Gondwana cratonic fragments (Bunopas and Vella, 1983; Hutchinson, 1989; Bunopas, 1991). Both the Shan-Thai and the Indochina Terrane contain Early to Late Paleozoic clastic sedimentary rocks, platform carbonates and deep water clastic sedimentary rocks. The Indochina terranes have been overlain by Triassic volcanic rocks and intruded by Triassic granites. In the Shan-Thai terrane, the Paleozoic rocks were intruded by Triassic and Cretaceous granites (Dunning et al., 1995). All of these rocks were overlain by sedimentary units of the Triassic-Jurassic Khorat Group.

Volcanic rocks in Thailand may be divided into four belts from west to east such as Chiang Rai-Chiang Mai Volcanic Belt, Chiang Khong-Chanthaburi Volcanic Belt, Loei-Phetchabun-Nakhon Nayok Volcanic Belt and Sra Kaew Volcanic Belt (Fig. 2.1). The study area is in the central portion of the Loei-Phetchabun-Nakhon Nayok Volcanic Belt. The

Loei-Phetchabun-Nakhon Nayok (LPN) Volcanic Belt is composed of acidic to basic lavas and pyroclastic rocks compositionally equivalent to the lavas. The volcanic rocks of the LPN Volcanic belt is distributed from Loei area to Sra Kaew. Intasopa and Dunn (1994) considered that the volcanic rocks in this belt are Devonian rhyolite (Rb-Sr isochron age of 374±33 Ma), Middle Devonian-Lower Carboniferous basalt and Permo-Triassic andesite. Panjasawawong et al. (2006) reported that the volcanic rocks in the area are composed of basaltic pillow lava, hyaloclastic and pillow breccia. The basalts were classified into transitional tholeitic basalt, tholeitic micrograbbro and calc-alkalic basalt/andesite. The tholeitic basalt and tholeitic micrograbbro are in the mid-oceanic ridge basalt (MORB) field. The calc-alkalic basalt/andesite is interpreted as oceanic island arc lavas (Jungyusuk and Khositanont, 1992). The arc lavas might have been built on an oceanic basement in an oceanic basin or in a mature back-arc basin. Promo-Triassic volcanic rocks are widely distributed from the Loei though Phechabun to Nakorn Nayok areas.

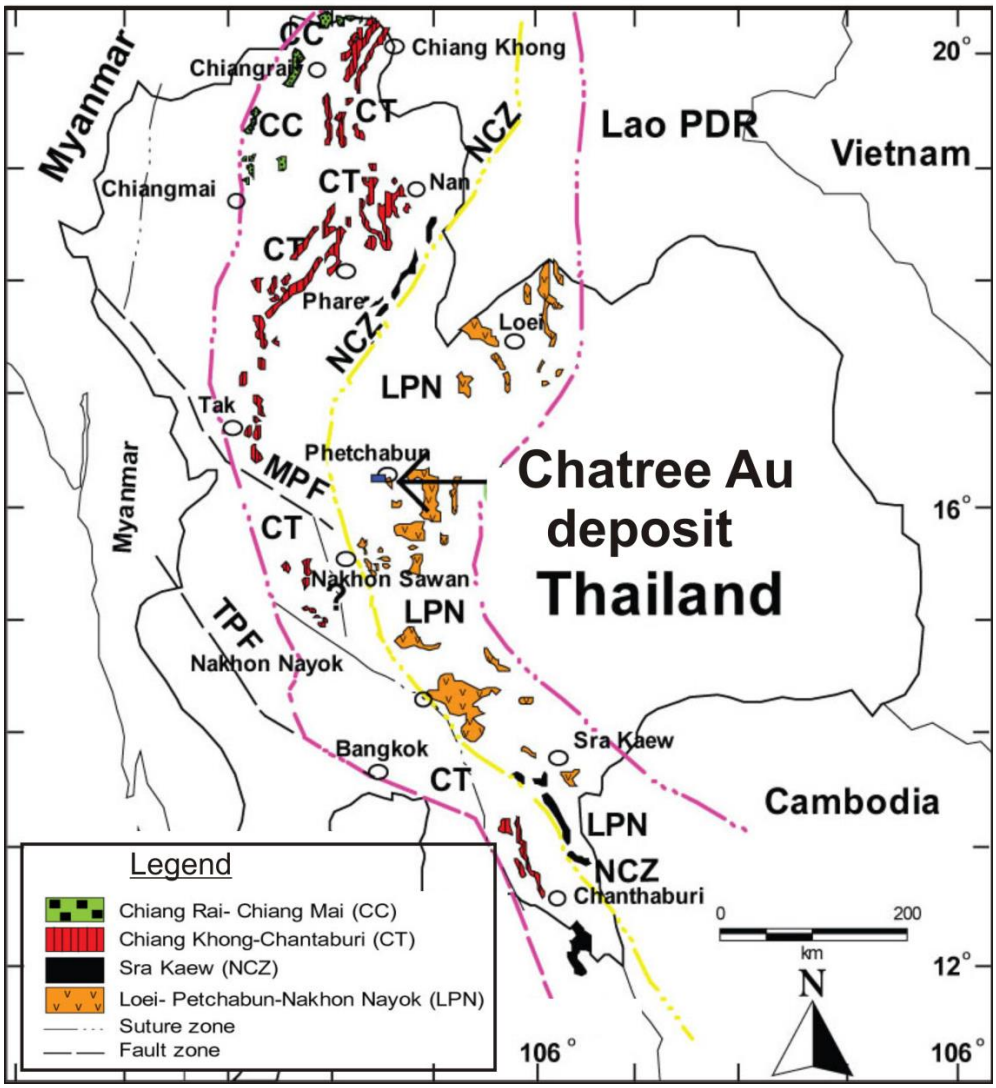

Figure 2.1 Distribution of volcanic belts in Thailand and the Chatree gold deposit (Intasopa, 1993; Jungyusuk and Khositanont, 1992; Panjasawatwong et al., 2006; Barr and Charusiri, 2010). Volcanic belts can be separated into Chiang Rai - Chiang Mai (CC), Chiang Khong – Chantaburi (CT), Sra Kaew (NC) and Loei – Phetchabun – Nakhon Nayok (LPN) belts. The Chatree gold deposit is located in the LPN belt.

2.2 Mineral deposit of the Loei-Phetchabun volcanic belt

The Loei-Phetchabun-Nakorn Nayok volcanic belt extends from Loei province through Phetchabun to Sra Kaew province. Ore deposits of the belt consist of a variety of mineral deposits including Cu-Au skarn, porphyry Cu-Au and epithermal gold deposits (Fig. 2.2). The ore deposits are related to volcanic-plutonic rocks in this belt in Late Permian to Early Jurassic age.

Skarn deposits are characterised by Cu-Au exoskarn in the calcareous host rocks in contact with dioritic intrusion such at Puthep (PUT1 and PUT2), Loei province. Cu-Au mineralization is related to dioritic and granodioritic rocks. These intrusions were emplaced into Carboniferous sedimentary rocks including siltstone, limestone and sandstone. U-Pb zircon dating of the PUT1 intrusion yielded middle Triassic age (242.4±1.3 Ma); laser ablation $^{40}Ar/^{39}Ar$ dating of biotite from the same intrusions indicates 248±2 and 247±6 Ma. The Re-Os dating of molydenite is between the zircon and biotite age at 245.9±0.9 Ma indicating that mineralization and intrusion appear to have occurred during 248-242 Ma (Zaw et al., 2007).

Phu Thap Fah gold skarn deposit in Loei area is hosted in a Permian sedimentary sequence consisting of shale, crystalline limestone, muddy sandstone, carbonaceous siltstone and shale that were intruded by Early Triassic granodiorite (U-Pb zircon age 245±3 Ma) and Late Triassic andesitic dike (U-Pb zircon age 221±5 Ma). The skarn mineralization is characterized by early development of andraditic garnet-clinopyroxene skarn followed by retrograde alteration and mineralization. The retrograde skarn assemblage consists of amphiboles, epidote, chlorite, carbonate and quartz. Gold occurs as electrum, gold-bismuth and gold-bismuth-telluride associations and the greater part of the gold is confined to massive pyrrhotite and pyrite with chalcopyrite in the retrograde zone (Zaw et al., 2008).

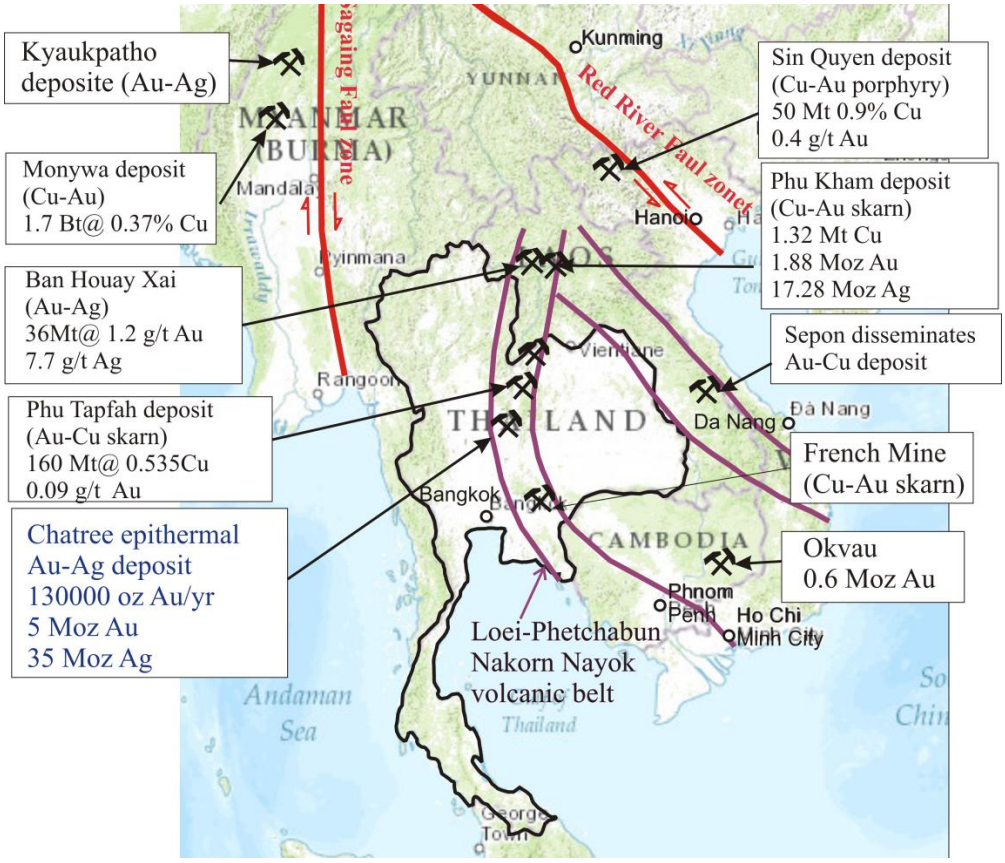

Figure 2.2 Map shows the potential of ore mineralization in the Thailand, Laos, Cambodia, Vietnam and Myanmar. This belt, which was formed in Laos through Thailand to Cambodia contains of Au-Cu porphyry, Au-Cu skarn and epithermal gold deposits.

The epithermal mineralization in the Upper Permian and Triassic between Phichit and Phetchabun discovered in the late 1982 has been developed into a mine at Chatree deposit. The gold-bearing quartz veins are characterized by quartz-adularia-calcite vein, breccias and stockworks (Tangwattananukul et al., 2014). The Au-bearing quartz veins occur in volcanic sedimentary rocks, polymictic andesitic breccia and monomictic andesitic breccia. The $^{40}Ar/^{39}Ar$ dating of adularia of the Au-bearing quartz veins is 250.9±0.8 Ma (Salam et al., 2013). Fe-Cu-Au deposit occurs along the Loei-Phetchabun-Nakhon Nayok volcanic belt. The U-Pb zircon age of the plutonic rocks associated with these small Fe-Cu skarn deposit are 245 to 241 in Khao Lak deposit (Salam et al., 2013).

2.3 Regional geology of the Chatree area

The Loei-Phetchabun-Nakhon Nayok Volcanic belt is approximately 600 km long and 50 km wide. The belt is composed of calc-alkaline volcanic rocks, sedimentary rocks and intrusive rocks. It was formed as a result of amalgamation of micro-continental blocks and volcanic arc remnants (Intasopa and Dunn, 1994; Charusiri et al., 2002). Volcanic rocks in the belt are felsic to mafic volcanic rocks that were emplaced during several episodes of volcanic activities from Middle Devonian to Late Paleogene (Jungyusuk and Khositanont, 1992). The dominant volcanic rocks in the belt are andesite and basaltic andesite lavas. These volcanics were intruded by micrograbbro, diorite and granodiorite (Fig. 2.3). The gold mineralization at the Chatree deposit is spatially and chronologically associated with calc-alkaline volcanic rocks formed during the period of Carboniferous to Early Triassic (Jungyusuk and Khositanont, 1992; Diemar et al., 2000).

The geology of "Chon Dean"-"Thab Khlo" districts, in which the Chatree deposit is located, consists of sedimentary, volcanic and granitic rocks ranging from Carboniferous to Triassic ages. The Carboniferous strata consist of conglomerate, sandstone, shale, slate, chert, limestone, rhyolitic breccia and rhyolite (DMR, 1976; Salam et al., 2013). The Carboniferous unit of sedimentary strata consists mainly of limestone containing crinoids and coral fossils suggesting Lower to Middle Carboniferous (Department of Mineral Resource (DMR), 1976) (Fig. 2.3). The upper Carboniferous-Permian unit of sedimentary strata is composed of sandstone, shale, conglomerate and chert. The deposition age of sedimentary rock was 327±7 Ma (U-Pb detrital zircon by Zaw et al., 2007). Rhyolitic breccia and rhyolite associated with the Carboniferous sedimentary rocks near Khao Sai and Wang Yai have been dated at 323±5 Ma and 321±5 Ma, respectively (Zaw et al., 2007). Granites intruded in this unit. Massive limestone from early to middle Permian is distributed in the eastern part of the

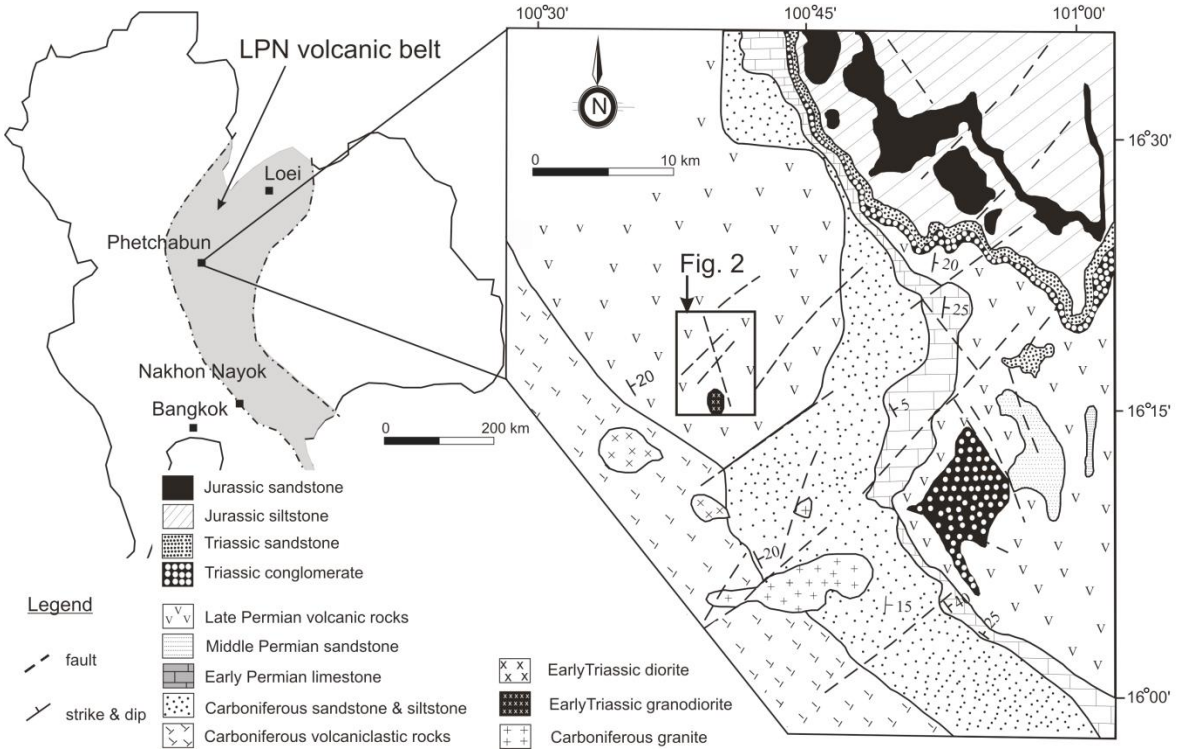

Figure 2.3 Geologic map of the Chatree deposit is located in the Loei-Phetchabun-Nakorn Nayok volcanic belt (DMR, 1976). Carboniferous sedimentary rock was overlain by permian volcanic rocks. Volcanic rocks around the Chatree area were intruded by granodiorite and diorite.

area. These Carboniferous and Permian strata are overlain by Permian to Triassic andesite to basaltic andesite flows, volcanic breccias and epiclastic sedimentary strata that are host rocks of the Au-bearing quartz veins at the Chatree deposit (Jungysuk and Khositanont, 1992). Early Triassic granodiorite and diorite intruded into the Permian -to- Triassic strata in the western and southern parts of the Chatree mining area. Triassic -to- Jurassic strata consist sandstone, conglomerate and siltstone (red beds) of the Khorat Group, which occur north of the Chatree deposit. The strata are thick sequences of intra-continental- derived sedimentary strata that unconformably overlie Permian-Triassic volcanic rocks.

Chapter 3: Geology, petrography and geochemistry of the Chatree mining area

3.1 Geology of the Chatree gold deposit

The geology around the Chatree mining area consists of Carboniferous sedimentary rocks, Early Permian limestone and Late Permian andesite lavas that are overlain by Triassic volcanic rocks and sedimentary rocks. Distribution of Carboniferous volcanogenic sedimentary rocks and Lower Permian limestone are shown in Fig. 2.3. Carboniferous sedimentary rocks are composed of siltstone, sandstone and limestone. Carboniferous sedimentary rocks are unconformably overlain by Permian andesite lavas of the Chatree deposit. Early Permian limestone is distributed in eastern part of the Chatree deposit with extension from north to south. Early Permian limestone contains warm water Tethyan macro faunas (Fontaine et al., 1991). Late Permian andesite lavas is the host rocks of the Chatree deposit. Rhyolitic tuff is distributed in the north of the Chatree mining area. Triassic volcanic rocks are composed of andesite lavas. Triassic sedimentary rocks consist of conglomerate and sandstone. The geology around the Chatree deposit suggests that the Chatree deposit is thought to be formed mostly under marine environment in Permian age and subaerial environment in Triassic age.

The geology of the Chatree mining area was divided into four units from Units 4 to 1 in ascending order (Figs. 3.1-3.4) (Salam et al., 2008; Cumming et al., 2008). The Unit 4 is composed of andesite lavas, monomictic andesitic breccias and minor polymictic andesite breccias. The U-Pb zircon age of andesite lava of Unit 4 was determined to be 258±3 and 250±6 Ma, corresponding to Late Permian (Zaw et al., 2007; Salam et al., 2008). The Unit 3

consists of polymictic andesitic breccia and polymictic andesitic basalt breccia that are partly interbedded and overlain by volcaniclastic sandstone, laminated carbonaceous mudstone and minor calcareous siltstone. The Unit 2 consists mainly of fine-grained epiclastic and minor sedimentary rocks including laminated siltstone, mudstone and carbonaceous to calcareous fossiliferous siltstone, and polymictic and monomictic rhyolitic breccia. The Unit 1 consists of rhyolitic tuff intercalated with siltstone and mudstone. This unit unconformably overlies the lower units. The gold-bearing quartz veins are mostly developed in the polymictic andesitic breccia of the Unit 3 and volcanic sedimentary breccia of the Unit 2.

In addition, there are young andesitic and basaltic dikes cutting all of the older rocks (Units 4 to 1). The andesite-basaltic andesite dikes trend toward NE and EW s (Fig. 3.1). Andesitic and basaltic dikes were dated between 238 and 244 Ma (Salam et al., 2013). Granodiorites are exposed approximately 2 km south of the Chatree deposit. The ages of granodiorite, as determined by method of U-Pb radiometric age using LA-ICP-MS, are 238±5 and 243±5 Ma (Salam et al., 2013). Cu-Mo mineralization is recognized in the granodiorite. The ages of molybdenite from the Cu-Mo-bearing quartz veinlets in the granodiorite determined by Re-Os radiometric method is 244±1 Ma (Salam et al., 2013). The age data of Cu-Mo mineralization at the N prospects suggest that the Cu-Mo mineralization is younger than the Au-mineralization of Chatree Au deposit.

An anticline trending N-S is present in the central part of the Chatree mining area. Strikes of major faults also trend toward NNW-SSE.

The Chatree deposit consists of seven open pits and four defined prospects. The A pit and Q prospect are located in the northern part of the deposit, the C, H, D, Kw and Ke pits are distributed in the central part of the deposit, and the B, N and V prospects occur in the southern part of the deposit (Fig. 3.1). The length and width of veins vary from 100 to 300 m

and 0.5 to 3 m, respectively. The veins dip from 65° to 85° to the west. Vertical extension of the veins ranges from 50 to 200 m. Current mining activity is focused on several mineralized veins, referred to as A, C, D, H, K pits and Q prospect (Fig. 3.1).

Geology and lithology of the A pit and the Q and B prospects were constructed on the basis of observation of host rocks and drilling cores in the open pits and prospects. Geology of the Chatree Au deposit consists of Units 4, 3, 2 and 1 in ascending order (Fig. 3.3). The Unit 4 consists of andesite lava and monomictic andesitic breccia. The Unit 4 is dominantly developed in the central area such as the C and H pits. The Unit 3 consists of thick polymictic andesitic breccia. The Unit 2 is composed of fine-grained volcaniclastic and epiclastic sandstone and siltstone. The Unit 1 is rhyolitic tuff. Rhyolitic tuff overlie unconformably over the Unit 2. Geology of the Q prospect is composed of the Units 3, 2 and 1 in ascending order (Figs. 3.3 and 3.4). The Unit 3 consists of thick polymictic andesitic breccia. The Unit 2 is divided into two subunits: Units 2a and 2b in ascending order. The Unit 2a consists of fine-grained volcaniclastic and epiclastic sandstone and siltstone, and the Unit 2b consists of monomictic rhyolitic breccia. The Unit 1 is composed of rhyolitic tuff. Andesite and basaltic andesite dikes cut strata from Units 3 to 1 at the Q prospect. The Au-bearing quartz veins occur in Units 3, 2a and 2b at the Q prospect (Fig. 3.3). The A pit is composed of the Units 3 to 1. The Unit 3 consists of polymictic andesitic breccia. The Unit 2 consists of fine-grained volcanic sedimentary rocks, epiclastic sandstone and mudstone including coral and fossil. The Au-bearing quartz veins occur in the Units 3 to 1 at A pit. The B prospect is located in the southern part of the Chatree mining area. The geology of B prospect is composed of the Units 3 and 2. The Unit 3 is composed of polymicit andesitic breccia. The Unit 2 is a thick sequence consisting of fine-grained volcaniclastic and siltstone.

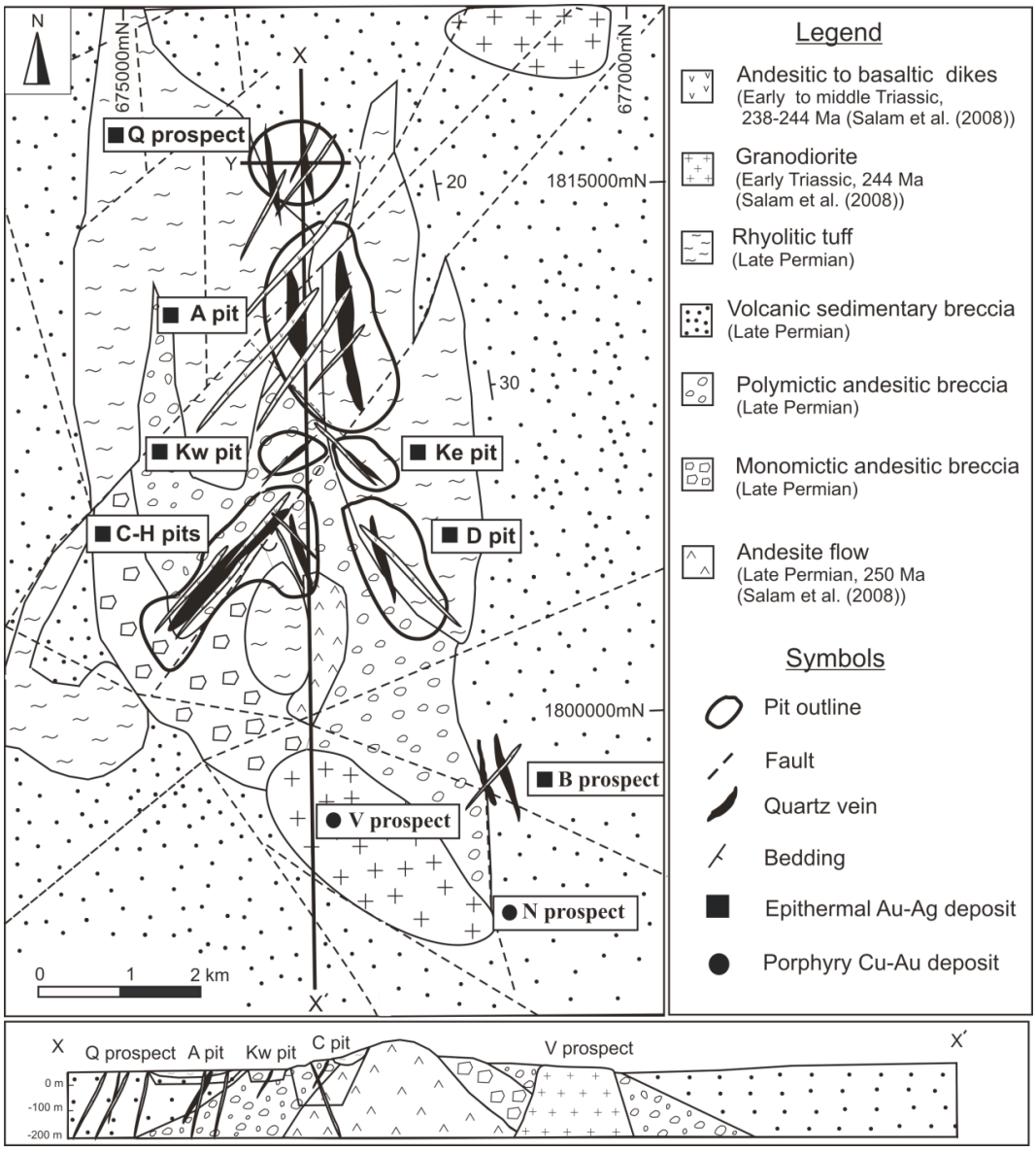

Figure. 3.1 Geologic map and cross section of the Chatree deposit. The locations of open pits and prospects of epithermal Au-Ag mineralization and Cu-Mo mineralization are shown in the map (Salam et al., 2008). The Au-bearing quartz veins are distributed from central to north (the C-H, Ke, D, A pits and Q prospect) of the Chatree mining area. The Cu-Mo-bearing quartz vein is located in the N and V prospects in the southern part of the Chatree mining area.

The N and V prospects are located in the southern part of the Chatree mining area. The geology of the N and V prospects consists of andesite lava and granodiorite porphyry. Andesite lava was intruded by granodiorite porphyry.

Figure. 3.2 Exposure of andesite lava (Unit 4) in the C pit covered by polymictic andesitic breccia (Unit 3), volcanic sedimentary rock (Unit 2) and rhyolitic tuff (Unit 1).

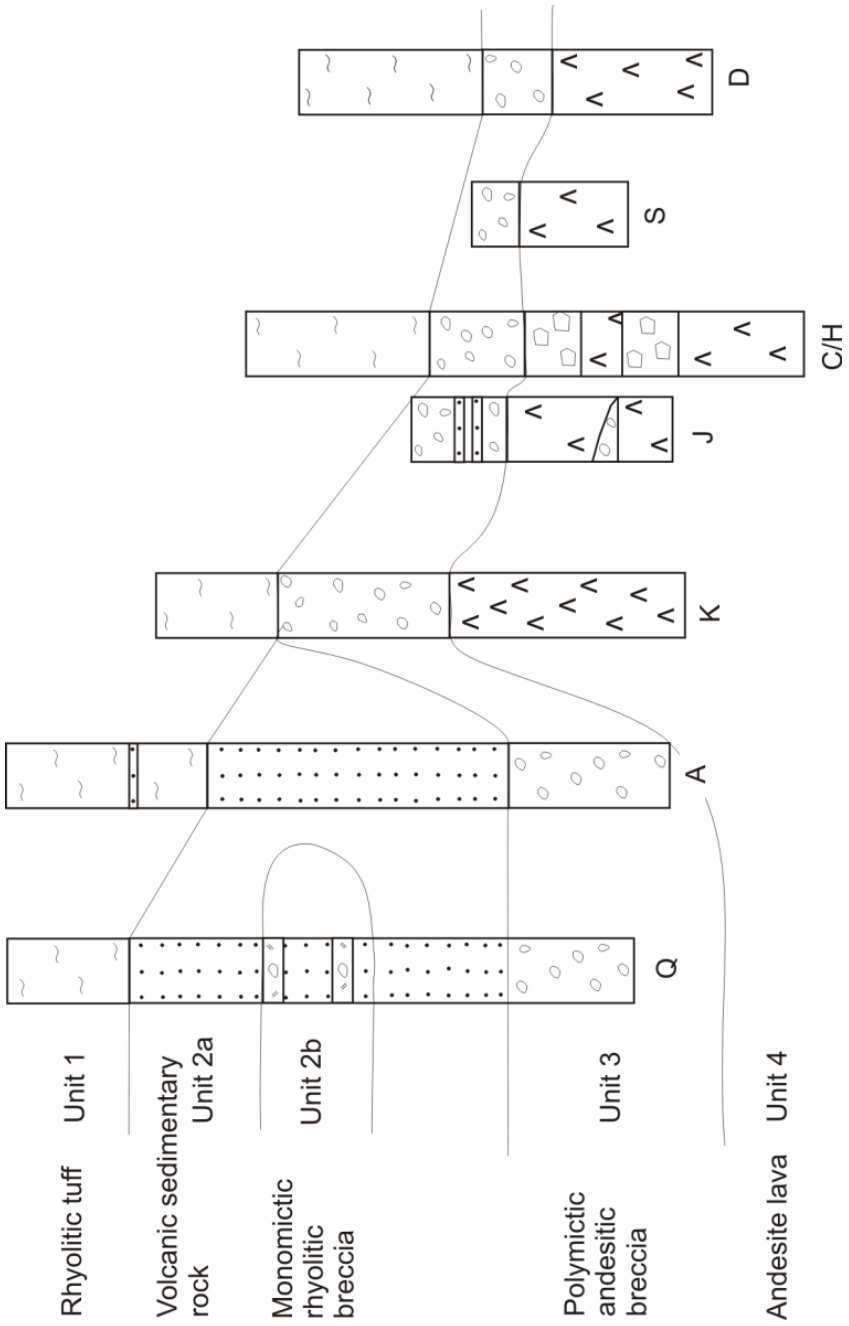

Figure 3.3 Geologic columns showing stratigraphy from the Q prospect to D pit consisting of andesite lava (Unit 4), polymictic andesitic breccia (Unit 3), volcanic sedimentary breccia (Unit 2a) and rhyolitic tuff (Unit 1) in ascending order (Cumming et al., 2008). Monomictic rhyolitic breccia (Unit 2b) is in the Q prospect. Andesite lava is thick in the central part of the area including K, J, C/H, S and D pits (Cumming et al., 2008).

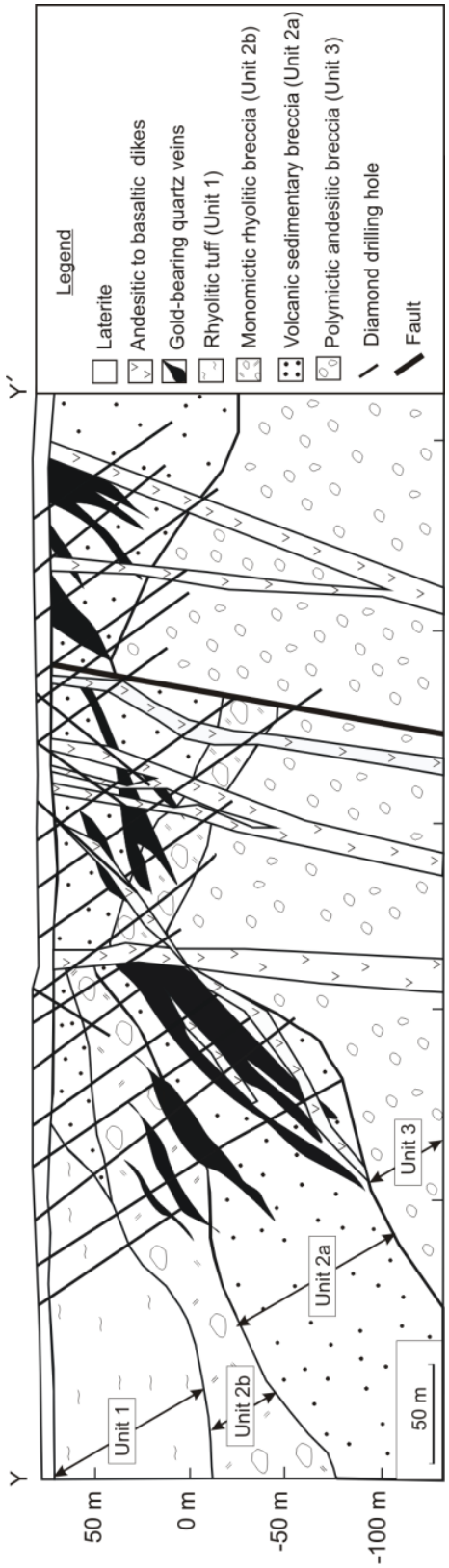

Figure 3.4 Cross section of the Q prospect. Y-Y′ corresponds to Y-Y′ in Fig. 3.1. Gold-bearing quartz veins occur mainly in volcanic sedimentary breccia (Unit 2a) and monomictic breccia (Unit 2b). Veins dip to the west (65^0-75^0) and cut by andesite dike.

3.1.1 Petrology of volcanic and plutonic rocks in the Chatree mining area

Volcanic rocks in the Chatree mining area consist of andesite lavas and post-mineralization andesitic dikes. Andesite lavas in the Chatree deposit occur from north to south of the area. Andesite lava is emplaced in north to central area as host rock of Au mineralization (Fig. 3.1). On the other hand, granodiorite porphyry that is related with Cu-Mo mineralization occurs in southern part of the Chatree deposit (Fig. 5.1).

Andesite lavas occur predominantly in southern part of C-H pits (Fig. 3.1). Andesite lava of Unit 4 is characterized by intersertal and porphyritic textures with euhedral to subhedral phenocrysts of plagioclase (1-5 mm), apatite and ilmenite (Fig. 3.5A). Groundmass is composed of fine-grained plagioclase. Ilmenite is replaced by sphene (Fig. 3.5B).

Andesite lava in the N prospect is characterized by green to dark green color and aphanitic texture. It consists of plagioclase (0.5-3 mm in diameter), magnetite (0.1-0.5 mm in diameter) and ilmenite and pyrite. Groundmass is comprised of plagioclase showing flow banding and porphyritic textures (Fig. 3.5C).

Polymicitc andesitic breccias consist of grey, green and red, variably- altered clasts. Clasts consist of mainly plagioclase andesite and hornblende andesite and minor of basaltic andesite and mudstone. The clasts are poorly- sorted, sub-rounded to angular and range from 0.5 to 3 cm in diameter. There are both matrix supported and clast supported.

Post-mineralization andesitic dikes cut the Au-bearing quartz veins and all of the rock units. It is characterized by porphyritic texture of plagioclase (<3 mm in diameter), trachytic texture of plagioclase, hornblende and pyroxene (Fig. 3.5D).

Intrusive rocks in the Chatree mining area are granodiorite porphyry in the southern part of the Chatree deposit and diorite away from the Chatree deposit. Cu-Mo mineralization

is related with granodiorite porphyry in southern part of the area. The granodiorite porphyry intruded into andesite lava. Granodiorite porphyry is composed of plagioclase (<3 mm in diameter), quartz, biotite, magnetite, ilmenite, pyrite and chalcopyrite. Granodiorite porphyry is characterized by porphyritic texture of plagioclase (<3 mm in diameter) in fine-grained groundmass of quartz. Plagioclase is subhedral to euhedral shape of oligoclase to andesine (Fig. 3.5E). Albite and caldsbad-albite twins are common. Sericite replaced some part of plagioclase crystals. Quartz phenocryst is 0.2 to 1.0 mm in diameter and has anhedral to subhedral shape and showing corroded texture. Biotite is replaced by chlorite.

Diorite exposed away from the Chatree mining area is characterized by major coarse-grained plagioclase, minor K-feldspar, hornblende, biotite, quartz, magnetite, ilmenite and chalcopyrite. Diorite is cut by pegmatite vein.

3.2 Analytical technique for XRF and ICP-MS analysis

Samples collected for the volcanic and intrusive rocks were selected for whole-rock geochemistry analyses determined by XRF and ICP-MS methods at Akita University. Major and trace element analyses were performed by glass bead method using Rigaku X-Ray fluorescence spectrometer (ZSX Primus II) at Akita University. Powder samples were grinded with alcohol for 3 minutes. The powder samples were kept in drying oven overnight or 12 hour at 35°C. The samples were kept in oven at temperature of 110°C overnight to measure amount of absorbed water ($H_2O(-)$). The loss on ignition (LOI) was determined by heating of 1-2 g of powder sample at the temperature of 900°C for 7 hours. Glass bead was prepared by mixture of 0.8 g of heated powder samples, 3 g of $Li_2B_4O_7$ and 1 g of $LiBO_2$.

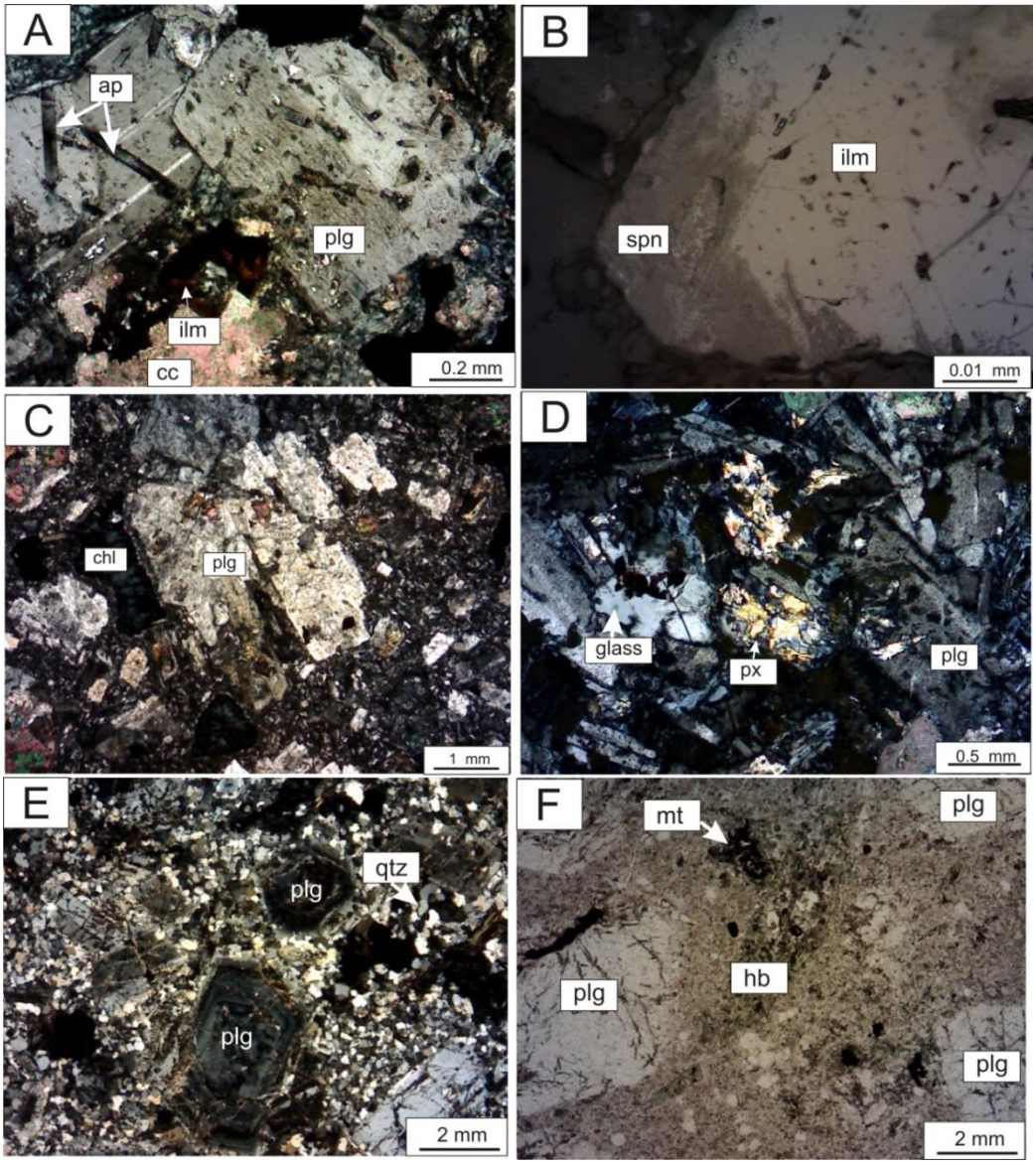

Figure 3.5 Photomicrographs showing mineral assemblages and textures of volcanic rocks and granodiorite porphyry in the Chatree area. (A) Andesite lava (Unit 4) consists of plagioclase and apatite. (B) Ilmenite is replaced by sphene. (C) Andesite lava at the N prospect showing porphyritic texture. (D) Post-mineralization andesite dike from the A pit shows relict texture of clinopyroxene. (E) Granodiorite porphyry in the N prospect showing oscillatory zoning of plagioclase. (F) Granodiorite porphyry consists of plagioclase phenocryst, biotite and magnetite. Abbreviations: plg = plagioclase, qtz = quartz, px = pyroxene, hb = hornblende, mt = magnetite, ilm = ilmenite, chl = chlorite, ap = apatite and spn = sphene.

Solution samples were prepared to determine concentration of trace elements. The analyses of the solution samples were carried out using ICP-MS (Agilent 7500cc) at Akita University. ICP-MS analyses were carried out by the method described by Sato et al. (1999).

3.3 Geochemisty of volcanic and intrusive rocks around the Chatree mining area

Major, minor and trace elements of representative rocks samples are shown in Tables 1 to 4. Harker diagrams of weakly altered andesite lava, strongly altered andesite lava, rhyolitic tuff, post-mineralization andesite dikes and granodiorite porphyry are shown in Figs. 3.6 and 3.7. The SiO_2 contents of the weakly altered andesite lava (Unit 4) from the Q prospect and C pit range from 51.9 to 52.5 wt%, TiO_2 from 0.4 to 2.9 wt%, Al_2O_3 from 14.8 to 18.2 wt%, t-Fe_2O_3 from 8.9 to 12.5 wt%, MnO from 0.2 to 0.3 wt%, MgO from 4.0 to 4.9 wt%, CaO from 4.8 to 5.3 wt%, Na_2O from 2.5 to 4.9 wt%, K_2O from 1.4 to 5.5 wt%, and P_2O_5 from 0.3 to 0.4 wt%. The SiO_2 contents of andesite lava from N and V prospects range from 54.0 to 64.6 wt%, TiO_2 from 0.4 to 0.7 wt%, Al_2O_3 from 16.9 to 23.1 wt%, t-Fe_2O_3 from 8.2 to 10.0 wt%, MnO from 0.1 to 0.2 wt%, MgO from 2.9 to 6.0 wt%, CaO from 2.3 to 7.4 wt%, Na_2O from 0.3 to 4.6 wt%, K_2O from 0.6 to 2.4 wt% and P_2O_5 about 0.1 wt%.

The SiO_2 contents of rhyolitic tuff range from 67.7 to 77.1 wt%, TiO_2 from 0.2 to 0.4 wt%, Al_2O_3 from 6.5 to 16.1 wt%, t-Fe_2O_3 from 2.3 to 6.5 wt%, MnO from 0.1 to 0.2 wt%, MgO from 1.6 to 12.6 wt%, CaO from 0.9 to 4.6 wt%, Na_2O from 0.1 to 4.6 wt%, K_2O from 0.5 to 4.4 wt%, and P_2O_5 from 0.1 to 0.2 wt%.

The SiO_2 contents of post-mineralization andesite dike range from 53.2 to 54.2 wt%, TiO_2 from 1.3 to 1.4 wt%, Al_2O_3 from 17.2 to 17.9 wt%, t-Fe_2O_3 from 8.8 to 10.5 wt%, MnO from 0.1 to 0.2 wt%, MgO from 3.9 to 5.4 wt%, CaO from 4.1 to 6.0 wt%, Na_2O from 3.9 to 5.0 wt%, K_2O from 0.4 to 2.4 wt% and P_2O_5 from 0.3 to 0.4 wt%.

The SiO_2 contents of granodiorite porphyry range from 68.0 to 68.1 wt%, TiO_2 from 0.4 to 0.5 wt%, Al_2O_3 from 17.1 to 17.4 wt%, t-Fe_2O_3 from 3.4 to 3.6 wt%, MnO about 0.1 wt%, MgO from 1.2 to 1.3 wt%, CaO from 3.5 to 4.1 wt%, Na_2O from 4.7 to 4.8 wt%, K_2O from 0.3 to 0.6 wt% and P_2O_5 from 0.1 to 0.2 wt%.

The TiO_2, t-Fe_2O_3, Al_2O_3, MgO and MnO contents of andesite lava and post-mineralization andesite dike decrease with increasing SiO_2 content. However, age difference between the andesite lavas and post-mineralization andesite dike is about 6 Ma (Salam et al., 2013). Therefore, this decreasing tendency is different from magmatic differentiation. Na_2O and K_2O contents are poorly correlated with SiO_2 content suggesting the influence of hydrothermal alteration.

The bivariate plots of the trace elements as a function of SiO_2 content of weakly altered andesite lava, weakly altered rhyolite, post-mineralization andesite dike and strongly altered granodiorite porphyry show the decrease of Sr, V, Zr, Y and Rb contents with increasing SiO_2 content (Fig. 3.7). Cu contents of strongly altered granodiorite porphyry are higher than andesite lava. This fact suggests that there is copper mineralization in the granodiorite porphyry. Zn, Ni and Pb content of the weakly altered andesite lava and weakly altered rhyolitic tuff decrease with increase in SiO_2 content. Ba contents of the weakly altered andesite lava, weakly altered rhyolitic tuff, strongly altered rhyolitic tuff are scattered widely and suggest an effect caused by the hydrothermal solution.

The volcanic rocks in the Chatree mining area was affected by hydrothermal solution. The Na_2O contents of the strongly altered andesite and strongly altered granodiorite are low, while Na_2O contents of the weakly altered andesite lavas and post-mineralization andesite dike are higher than those of the strongly altered andesite lavas. The andesite lava and post-mineralization andesite dikes have higher values for loss on ignition varying from 2.3 to 6.7 wt %, implying that they are also somewhat altered. Alteration of volcanic rock is determined by the alteration index (AI) (Ishikawa et al., 1976) and the chloride-carbonate-pyrite index (CCPI) (Large et al., 2001). The alteration box plot (Large et al., 2001) have

been used to determine the intensity of sericite, chlorite, carbonate and pyrite that replace feldspars and glass associated with periods of hydrothermal alteration.

Alteration index (AI) (Ishikawa et al., 1976) is defined as:

$$AI = 100 \times (K_2O+MgO) / (K_2O+MgO+Na_2O+CaO).$$

Chlorite-carbonate-pyrite index (CCPI) (Large et al., 2001) is defined as:

$$CCPI = 100 \times (MgO+FeO) / (MgO+FeO+Na_2O+K_2O).$$

where FeO is total $FeO+Fe_2O_3$ content of the rocks.

Hydrothermal alteration is principally related to the breakdown of plagioclase, other rock-forming minerals and volcanic glass in the primary volcanic rocks which were replaced by sericite, chlorite, pyrite and quartz (Fig. 3.8). Change of concentrations of K_2O, Na_2O, MgO and CaO are related to the breakdown of plagioclase and volcanic glass which are replaced by sericite and chlorite (Ishikawa et al., 1976; Large et al., 2001). MgO and FeO components are accommodated in Mg-Fe chlorite that replaced albite, K-feldspar or sericite. Therefore, the relationship among K_2O, Na_2O, MgO, FeO and CaO contents can be used to monitor the degree of alteration. Diagram of alteration index (AI) and chlorite-carbonate-pyrite index (CCPI) discriminates altered or unaltered volcanic rocks. Diagenetic alteration of volcanic rocks is also discriminated from hydrothermal alteration based on the AI and CCPI indexes.

Andesite lavas and post-mineralization andesite dikes from the Chatree mining area plotted in least altered box, suggesting the rocks are least altered. However, the strongly altered andesite lavas (light green) are plotted in the strongly altered chlorite-sericite-pyrite area (Fig. 3.8). The strongly altered rhyolitic tuff (Sample no. F1 and St17Ae) is plotted

near the chlorite alteration. Therefore, primary igneous characteristics of these rocks are examined on the basis of characteristics of immobile elements.

TiO_2 and Zr contents of andesite lava, rhyolitic tuff, post-mineralization andesite dike and granodiorite porphyry were plotted in the Fig. 3.9. Zr/TiO_2 ratios of weakly altered andesite lava, post-mineralization andesite dikes and strongly altered granodiorite porphyry show different trends. The weakly altered andesite lava has smaller Zr/TiO_2 ratios, while the granodiorite porphyry has higher Zr/TiO_2 ratios. The Zr/TiO_2 ratio of andesite lava is different from the Zr/TiO_2 ratio of granodiorite porphyry. The ratios of the post-mineralization andesite dikes are plotted between the ratios of andesite lava and granodiorite porphyry. The ratios of rhyolitic tuffs show the same Zr/TiO_2 ratios of granodiorite porphyry. Zr and TiO_2 contents of strongly altered andesite lava are low. However, the Zr/TiO_2 ratios of strongly altered andesite lavas are similar to the Zr/TiO_2 ratios of weakly altered andesite lava. The strongly altered andesite lava and weakly altered andesite lava are same andesite lava.

Chondrite-normalized (Boyton, 1984) REE patterns of andesite lavas, rhyolitic tuff, post-mineralization andesite dikes and granodiorite porphyry are shown in Fig. 3.10. The weakly altered andesite lava shows flat patterns with positive Eu anomaly. The weakly altered rhyolitic tuffs exhibit slightly higher REE contents with negative Eu anomaly than the strongly altered rhyolitic tuffs. Altered rhyolitic tuff shows flat REE patterns. The post-mineralization andesite dike is characterized by LREE-enriched pattern with no Eu anomaly. The chondrite-normalized REE patterns of granodiorite porphyry show more LREE-enriched patterns. The chondrite-normalized REE patterns of these rocks indicate that four separate magmatic activities are present at the Chatree mining area.

Table 1 Chemical compositions of major oxide (in wt. %) and trace elements composition (in ppm) of volcanic rocks and granodiorite porphyry determined by XRF.

Area	C pit		N&V prospects							Regional 682934E 1808807N	Regional 665903E 1802933N	Regional 671289E 1813959N
Rock type	andesite lava	rhyolitic tuff	andesite lava	andesite lava	andesite lava	andesite lava	andesite lava	granodiorite porphyry	granodiorite porphyry	diorite	andesite lava	andesitic tuff
Sample No.	and-C	St-11CH	NP-7	NP-11	NP-12	NP-13	NP-14	N-160.5	NP-5	D-1	P-1	And-1
(wt.%)												
SiO_2	52.48	71.89	58.29	57.76	46.97	54.01	64.55	68.06	68.06	48.62	60.86	57.90
TiO_2	0.48	0.31	0.45	0.51	0.70	0.52	0.43	0.51	0.44	0.65	0.42	0.69
Al_2O_3	18.15	12.54	16.94	19.35	23.07	18.61	14.21	17.45	17.09	20.69	16.02	17.86
t-Fe_2O_3	8.91	4.05	8.20	9.26	9.25	10.00	8.78	3.40	3.59	8.69	7.47	9.71
MnO	0.25	0.12	0.12	0.05	0.14	0.19	0.12	0.02	0.03	0.12	0.14	0.21
MgO	4.49	1.58	2.78	3.48	5.93	6.01	3.26	1.24	1.29	7.45	2.96	4.13
CaO	5.33	3.96	6.58	2.33	7.35	4.38	3.94	3.47	4.09	12.74	4.22	4.47
Na_2O	2.57	4.59	0.32	2.94	2.97	4.58	2.87	4.76	4.81	1.79	3.18	4.57
K_2O	5.50	0.48	5.95	2.39	2.03	0.63	1.14	0.62	0.36	0.34	4.08	0.52
P_2O_5	0.09	0.06	0.09	0.12	0.08	0.08	0.08	0.17	0.16	0.02	0.08	0.20
LOI	6.77	3.13	5.69	2.88	2.62	3.53	3.34	1.88	1.14	1.34	1.19	2.29
H_2O (-)	0.37	0.19	0.15	0.57	0.78	0.73	0.83	0.35	0.22	0.29	0.33	0.39
Total	99.07	99.77	99.87	98.75	99.28	99.74	100.19	98.70	100.05	100.18	99.76	100.30
(ppm)												
Ba	1024	129	1628	722	266	42	305	238	106	bd	1003	111
Cu	149	20	111	7883	347	99	156	1076	361	57	107	45
Zn	60	47	52	46	67	76	51	45	31	52	72	96
Pb	10	1	3	bd	9	9	11	bd	2	10	10	2
Zr	41	72	23	29	58	45	37	100	87	18	38	48
Rb	183	8	73	238	104	75	92	206	bd	6	69	bd
Sr	280	na	254	352	347	351	264	647	735	680	219	357
Nb	bd	na	2	2	4	bd	bd	bd	bd	bd	2	2
Ce	51	na	83	43	25	14	27	27	19	15	58	19
Co	29	7	19	40	21	23	34	3	13	35	20	10
Cr	19	13	42	22	45	56	24	4	5	121	28	12
Ni	20	4	7	9	26	24	6	1	9	47	3	3
Th	99	na	12	152	88	81	87	143	11	14	11	7
Y	15	13	14	bd	16	5	10	bd	8	5	16	21
V	262	62	146	153	457	295	195	87	84	214	134	187
Alteration index												
AI	57.0	19.4	55.8	52.7	43.6	42.6	39.2	18.4	15.6	34.9	48.7	33.9
CCPI	63.2	52.6	63.6	70.5	75.2	75.5	75.0	46.3	48.6	88.3	59.0	73.1

na, not analyzed; bd, below detection limit; AI, Ishikawa alteration index (Ishikawa et al., 1976); CCCPI, chlorite-carbonate-pyrite index (Large et al., (2001)

Table 2 Major oxide (in wt. %) and trace elements composition (in ppm) of volcanic rocks and granodiorite porphyry determined by XRF.

Area	C pit		N & V prospects							Regional 682934E 1808807N	Regional 665903E 1802933N	Regional 671289E 1813959N
Rock type	andesite lava	rhyolitic tuff	andesite lava	andesite lava	andesite lava	andesite lava	andesite lava	granodiorite porphyry	granodiorite porphyry	diorite	andesite lava	andesitic tuff
Sample No.	and-C	St-11CH	NP-7	NP-11	NP-12	NP-13	NP-14	N-160.5	NP-5	D-1	P-1	And-1
(wt.%)												
SiO_2	52.48	71.89	58.29	57.76	46.97	54.01	64.55	68.06	68.06	48.62	60.86	57.90
TiO_2	0.48	0.31	0.45	0.51	0.70	0.52	0.43	0.51	0.44	0.65	0.42	0.69
Al_2O_3	18.15	12.54	16.94	19.35	23.07	18.61	14.21	17.45	17.09	20.69	16.02	17.86
$t\text{-}Fe_2O_3$	8.91	4.05	8.20	9.26	9.25	10.00	8.78	3.40	3.59	8.69	7.47	9.71
MnO	0.25	0.12	0.12	0.05	0.14	0.19	0.12	0.02	0.03	0.12	0.14	0.21
MgO	4.49	1.58	2.78	3.48	5.93	6.01	3.26	1.24	1.29	7.45	2.96	4.13
CaO	5.33	3.96	6.58	2.33	7.35	4.38	3.94	3.47	4.09	12.74	4.22	4.47
Na_2O	2.57	4.59	0.32	2.94	2.97	4.58	2.87	4.76	4.81	1.79	3.18	4.57
K_2O	5.50	0.48	5.95	2.39	2.03	0.63	1.14	0.62	0.36	0.34	4.08	0.52
P_2O_5	0.09	0.06	0.09	0.12	0.08	0.08	0.08	0.17	0.16	0.02	0.08	0.20
LOI	6.77	3.13	5.69	2.88	2.62	3.53	3.34	1.88	1.14	1.34	1.19	2.29
H_2O (-)	0.37	0.19	0.15	0.57	0.78	0.73	0.83	0.35	0.22	0.29	0.33	0.39
Total	99.07	99.77	99.87	98.75	99.28	99.74	100.19	98.70	100.05	100.18	99.76	100.30
(ppm)												
Ba	1024	129	1628	722	266	42	305	238	106	bd	1003	111
Cu	149	20	111	7883	347	99	156	1076	361	57	107	45
Zn	60	47	52	46	67	76	51	45	31	52	72	96
Pb	10	1	3	bd	9	9	11	bd	2	10	10	2
Zr	41	72	23	29	58	45	37	100	87	18	38	48
Rb	183	8	73	238	104	75	92	206	bd	6	69	bd
Sr	280	237	254	352	347	351	264	647	735	680	219	357
Nb	bd	na	2	2	4	bd	bd	bd	bd	bd	2	2
Ce	51	na	83	43	25	14	27	27	19	15	58	19
Co	29	7	19	40	21	23	34	3	13	35	20	10
Cr	19	13	42	22	45	56	24	4	5	121	28	12
Ni	20	4	7	9	26	24	6	1	9	47	3	3
Th	99	na	12	152	88	81	87	143	11	14	11	7
Y	15	13	14	bd	16	5	10	bd	8	5	16	21
V	262	62	146	153	457	295	195	87	84	214	134	187
Alteration index												
AI	57.0	19.4	55.8	52.7	43.6	42.6	39.2	18.4	15.6	34.9	48.7	33.9
CCPI	63.2	52.6	63.6	70.5	75.2	75.5	75.0	46.3	48.6	88.3	59.0	73.1

na, not analyzed; bd, below detection limit; AI, Ishikawa alteration index (Ishikawa et al., 1976); CCCPI, chlorite-carbonate-pyrite index (Large et al., (2001)

Table 3 Concentrations of trace elements and REEs (in ppm) of volcanic rocks and granodiorite porphyry determined by ICP-MS.

Area	Q prospect						A pit		C pit
Rock type	andesite lava	strongly altered andesite lava	rhyolitic tuff	rhyolitic tuff	rhyolitic tuff	post-min andesite dike	rhyolitic tuff	rhyolitic tuff	rhyolitic tuff
Sample No.	and-Q	Qgs-3wr	F-1	F-2	F-3	gan-3	As	St-17Ae	St-11CH
(ppm)									
Sc	32.7	7.74	7.72	8.06	19.5	22.5	15.0	20.0	14.9
V	299	22.6	127	42.2	112	237	54.2	85.7	62.6
Cr	7.47	11.2	7.48	3.04	11.7	27.5	6.93	7.02	6.83
Mn	bd	147	4440	952	542	490	883	689	759
Co	20.9	2.46	3.96	2.85	9.72	22.5	6.53	8.65	5.84
Ni	3.78	3.46	1.70	1.05	4.65	16.8	2.47	3.97	2.50
Cu	24.3	15.1	21.8	11.6	86.4	98.5	31.8	44.1	24.7
Zn	225	14.3	5.76	45.1	96.0	89.1	49.7	68.4	44.5
Ga	20.4	73.7	9.81	8.79	13.9	55.4	12.4	15.3	10.3
As	16.1	43.6	na	na	na	5.90	na	na	na
Rb	22.0	58.5	7.17	60.1	36.2	31.6	9.78	26.4	4.20
Sr	552	36.0	238	90.3	147	494	220	147	214
Y	44.5	2.59	5.51	7.26	16.9	23.8	17.4	15.2	14.7
Zr	221	13.8	15.0	25.5	46.3	146	53.2	72.8	52.5
Nb	6.99	0.67	0.51	0.77	1.33	4.80	1.54	1.75	1.47
Sn	1.63	0.31	0.23	0.42	0.49	1.12	0.62	0.70	0.49
Sb	0.57	1.76	0.76	1.98	0.23	0.89	48.0	0.55	0.32
Te	0.10	0.01	0.09	0.04	0.04	bd	0.02	0.03	bd
Cs	1.08	0.37	0.30	0.31	1.93	0.35	0.27	1.13	0.18
Ba	1430	454	32.2	2160	140	796	60.1	291	157
La	18.2	0.68	1.91	2.56	4.22	13.9	5.49	7.45	5.01
Ce	46.0	1.37	4.40	5.89	9.39	31.1	12.2	16.6	11.3
Pr	6.59	0.18	0.63	0.78	1.32	4.54	1.65	2.27	1.52
Nd	32.1	0.84	2.96	3.58	6.23	20.2	7.52	9.98	7.20
Sm	8.01	0.28	0.76	0.95	1.71	5.14	2.15	2.48	1.85
Eu	3.01	0.26	0.30	0.37	0.64	1.52	0.60	0.65	0.55
Gd	9.36	0.35	0.89	1.02	2.38	5.42	2.69	2.67	2.14
Tb	1.35	0.06	0.14	0.18	0.36	0.77	0.45	0.46	0.37
Dy	8.21	0.45	0.93	1.19	2.38	4.43	3.02	2.84	2.52
Ho	1.64	0.11	0.20	0.27	0.60	0.89	0.63	0.61	0.54
Er	4.68	0.35	0.61	0.85	1.98	2.58	1.92	1.90	1.66
Tm	0.64	0.06	0.09	0.13	0.27	0.37	0.28	0.29	0.26
Yb	4.09	0.44	0.55	0.90	1.63	2.32	1.91	2.00	1.74
Lu	0.60	0.07	0.09	0.14	0.28	0.35	0.29	0.31	0.28
Hf	4.54	0.44	0.43	0.93	1.43	4.00	1.71	2.11	1.65
Ta	0.57	0.23	0.14	0.28	0.57	1.15	0.33	0.34	0.23
Tl	0.19	0.97	0.08	0.40	0.37	0.21	0.15	0.18	0.04
Pb	4.38	15.5	1.18	3.37	12.0	2.97	66.8	4.93	1.96
Bi	0.03	0.02	0.07	0.04	0.12	0.02	0.20	0.24	0.13
Th	1.98	0.25	0.22	0.46	0.58	1.50	0.75	0.95	0.56
U	0.73	1.82	0.14	0.17	0.23	0.58	0.28	0.31	0.20

na, not analyzed; bd, below detection limit

Table 4 Trace elements and REEs (in ppm) of volcanic rocks and granodiorite porphyry determined by ICP-MS.

Area	N&V prospects					Regional 682934E 1808807N	Regional 665903E 1802933N	Regional 671289E 1813959N
Rock type	andesite lava	andesite lava	andesite lava	granodiorite porphyry	granodiorite porphyry	diorite	andesite lava	andesitic tuff
Sample No.	NP-7	NP-11	NP-13	N-160.5	NP-5	D-1	P-1	And-1
(ppm)								
Sc	24.1	39.6	34.1	6.29	6.14	29.9	20.02	32.1
V	226	1440	296	59.0	64.1	1090	198	139
Cr	20.4	49.4	41.1	9.95	9.79	160	18.8	10.5
Mn	595	na	2360	290	236	na	487	1330
Co	43.9	12.6	26.1	6.04	6.82	29.8	18.0	17.2
Ni	15.8	13.6	22.5	5.28	4.51	54.31	5.94	4.85
Cu	na	62.8	93.2	3840	398	56.7	99.7	34.7
Zn	51.9	86.0	59.4	45.6	40.8	56.7	59.7	90.7
Ga	15.8	18.3	15.9	19.3	18.3	19.0	14.1	16.9
As	1.20	11.9	14.1	1.37	1.79	2.72	3.88	3.13
Rb	41.3	91.6	12.7	6.79	4.13	9.93	58.1	22.0
Sr	439	642	371	1530	897	3720	216	242
Y	6.37	9.60	10.2	5.92	6.72	4.41	10.7	14.2
Zr	7.40	13.1	12.2	40.9	28.1	7.12	23.6	41
Nb	0.54	2.68	0.71	11.0	3.48	0.38	1.23	1.38
Sn	1.49	0.56	0.39	0.82	0.56	0.38	0.29	0.70
Sb	0.13	1.41	1.29	0.25	0.21	0.23	0.41	0.23
Te	0.16	0.22	0.31	0.06	0.11	0.20	0.13	0.06
Cs	0.62	1.04	0.82	0.55	0.52	0.44	1.64	0.26
Ba	4520	na	76.6	181	203	55.3	663	62.3
La	2.21	3.40	1.81	10.2	10.1	1.36	2.89	4.31
Ce	5.04	7.40	4.49	22.6	21.4	3.25	6.50	9.86
Pr	0.72	1.02	0.70	2.75	2.77	0.50	0.93	1.44
Nd	3.45	4.76	3.66	11.3	11.7	2.60	4.52	7.03
Sm	0.97	1.36	1.20	2.06	2.19	0.76	1.33	1.97
Eu	0.57	1.00	0.49	0.76	0.60	0.45	0.69	0.72
Gd	1.12	1.66	1.54	1.86	1.94	0.90	1.68	2.37
Tb	0.18	0.27	0.27	0.22	0.24	0.14	0.27	0.38
Dy	1.19	1.76	1.83	1.20	1.31	0.87	1.80	2.57
Ho	0.25	0.37	0.40	0.22	0.24	0.18	0.40	0.55
Er	0.76	1.07	1.21	2.63	0.69	0.49	1.20	1.65
Tm	0.11	0.15	0.18	0.08	0.10	0.07	0.18	0.24
Yb	0.73	1.00	1.15	0.55	0.61	0.46	1.15	1.64
Lu	0.11	0.15	0.18	0.08	0.09	0.07	0.18	0.25
Hf	0.25	0.46	0.47	0.96	0.89	0.26	0.80	1.03
Ta	0.11	0.42	0.20	0.73	0.31	0.35	0.28	0.26
Tl	0.18	0.41	0.12	0.04	0.02	0.07	0.48	0.04
Pb	1.69	2.00	1.11	2.06	1.51	1.00	4.93	2.17
Bi	0.15	0.11	0.07	0.04	0.02	0.05	0.04	0.04
Th	0.19	0.43	0.20	0.68	0.65	0.06	0.42	0.71
U	0.17	0.10	0.09	0.25	0.21	0.04	0.12	0.27

na, not analyzed; bd, below detection limit

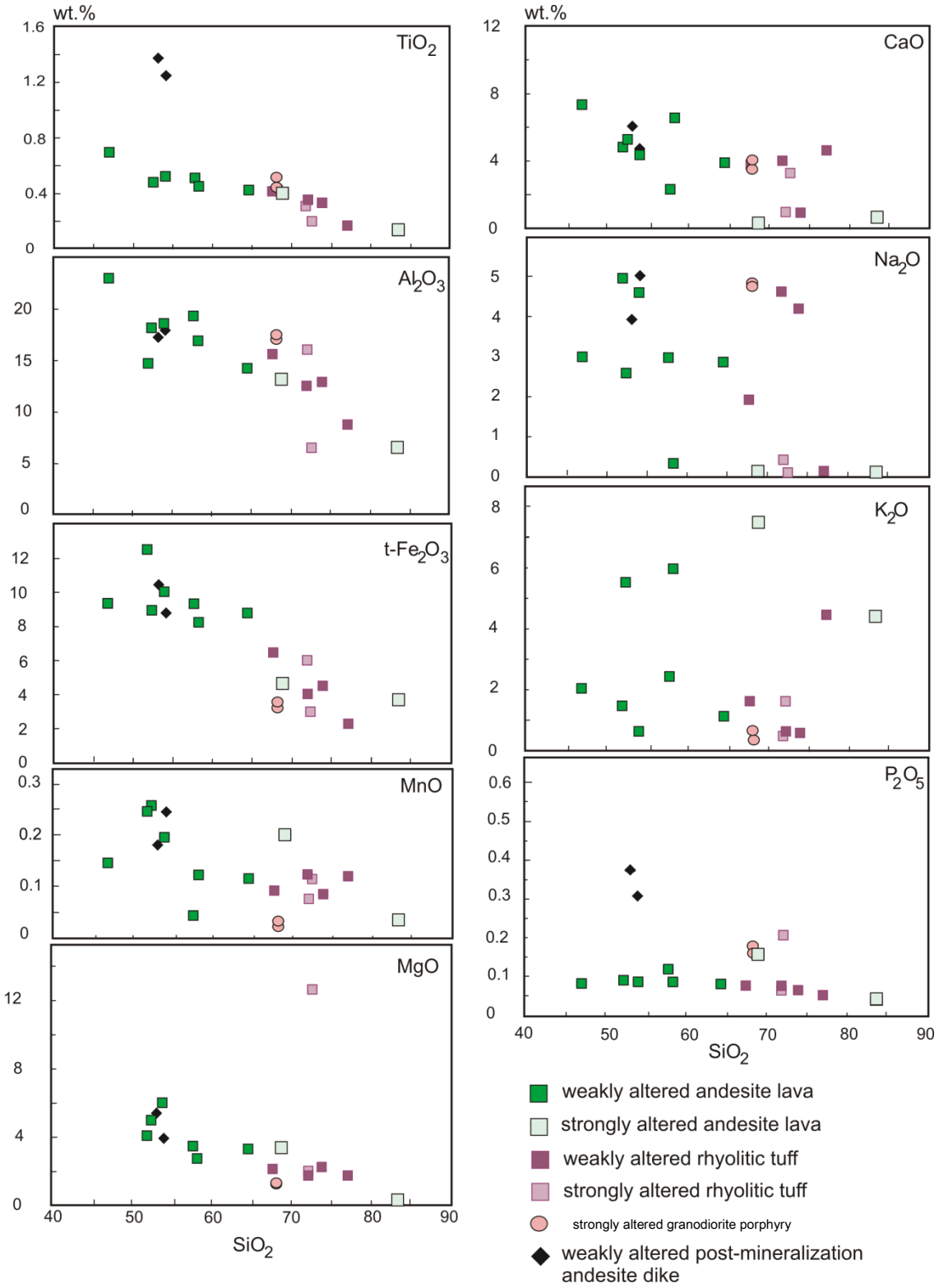

Figure 3.6 Harker diagram plots between SiO_2 and major oxides of weakly altered andesite lava, strongly altered andesite lava, weakly altered rhyolitic tuff, weakly altered post-mineralization andesite dike and strongly altered granodiorite porphyry.

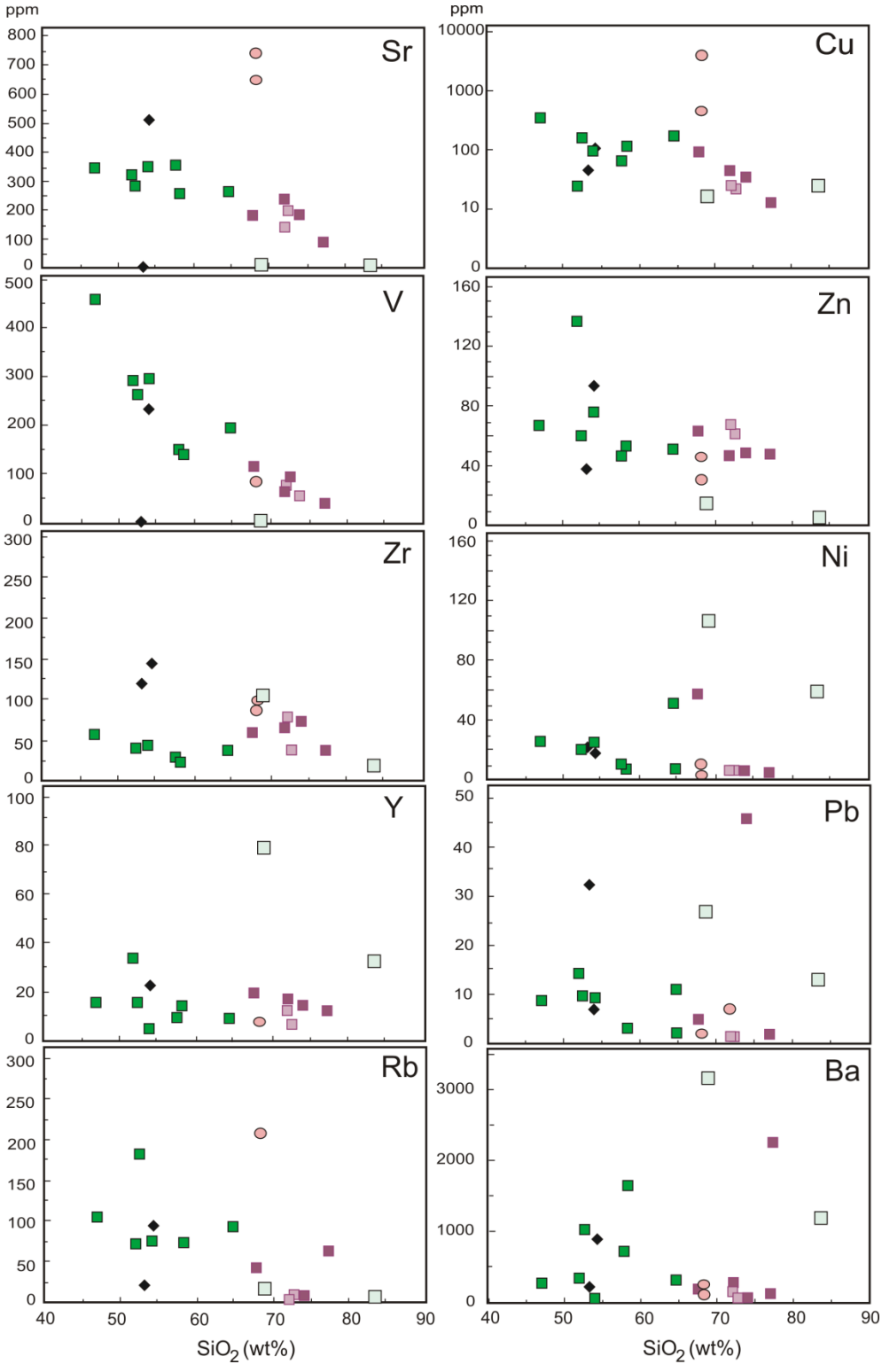

Figure 3.7 Harker diagram plots between SiO_2 and trace elements of weakly altered andesite lava, strongly altered andesite lava, weakly altered rhyolitic tuff, weakly altered post-mineralization andesite dike and strongly altered granodiorite porphyry.

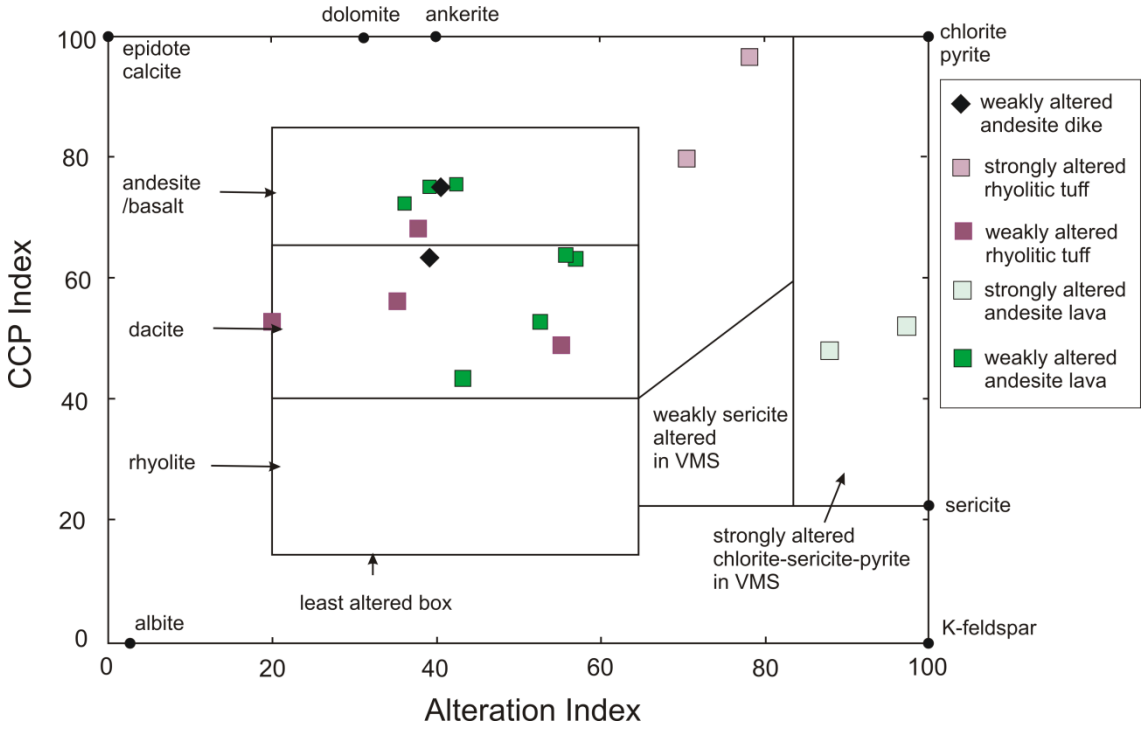

Figure 3.8 Diagram of alteration index (AI; Ishikawa et al., 1976) and CCP index (Large et al., 2001). Data of andesite lavas, rhyolitic tuffs and post-mineralization andesite dikes are plotted in least altered box ranging from dacite to andesite/basalt compositions. Data of the strongly altered andesite lava is plotted in the strongly altered chlorite-sericite-pyrite zone of VMS deposits. Data of the strongly altered rhyolitic tuffs (sample no. F1 and St17Ae) are plotted area near the strongly altered chlorite-sericite-pyrite zone.

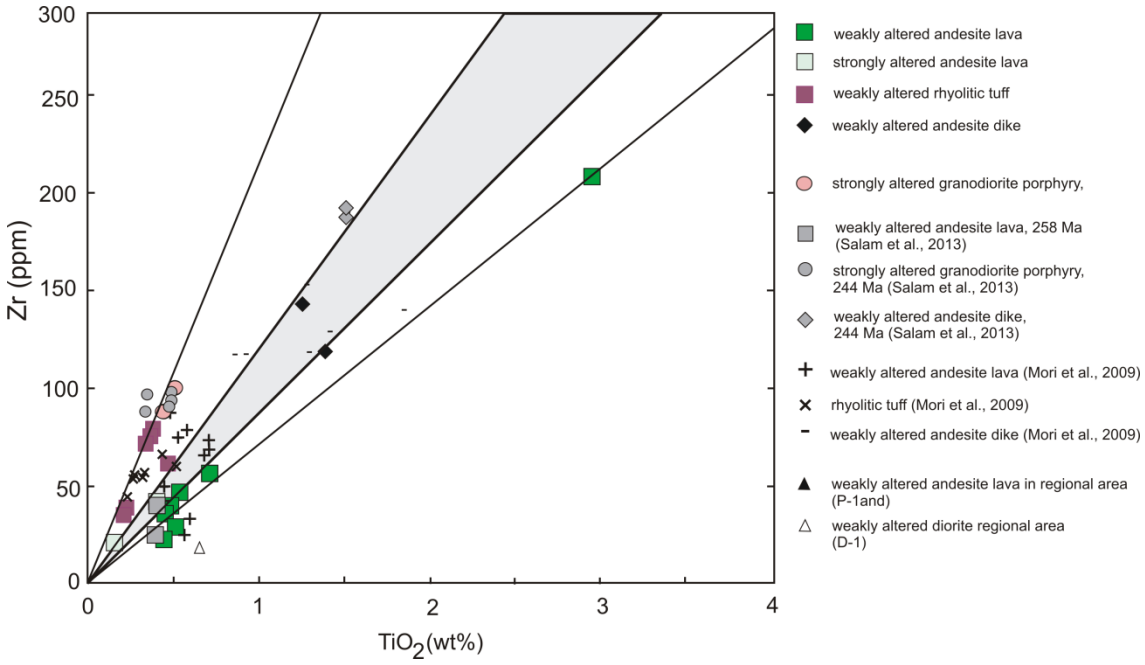

Figure 3.9 Diagram of Zr versus TiO_2 contents of the weakly altered andesite lava, strongly altered andesite lava, weakly altered rhyolitic tuff, post-mineralization andesite dike and granodiorite porphyry. Zr and TiO_2 contents in rocks are determined by XRF.

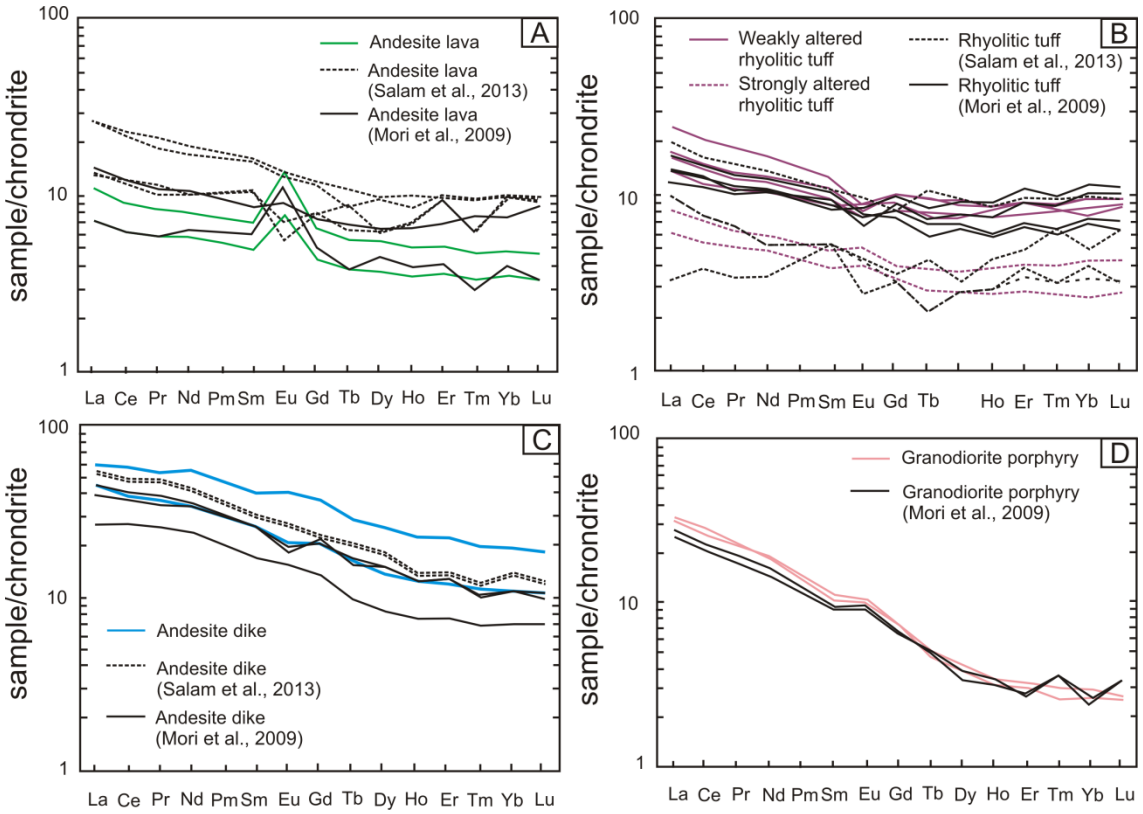

Figure 3.10 Chondrite-normalized REE patterns of andesite lava, weakly altered rhyolitic tuff, strongly altered rhyolitic tuff, post-mineralization andesite dike and granodiorite porphyry in the Chatree deposit.

3.4 Characteristics of igneous activities of the Chatree deposit

The andesitic volcanic sequence at the Chatree mining area can be separated into two volcanic activities; andesite lava and post-mineralization andesite dike. Andesite lava consists of low Ti, Zr and low REE contents. On the other hand, the post-mineralization andesite dike is characterized by slightly higher Ti, Zr and REE contents. The granodiorite porphyry is characterized by high Ti, Zr and REE contents. Zr/TiO_2 ratios of andesite lavas, post-mineralization andesite dikes and granodiorite porphyries are characterized by low, intermediate and high ratios, respectively. The chondrite-normalized REE patterns of andesite lavas and granodiorite porphyry are different. Ages of andesite lavas, post-mineralization andesite dikes and granodiorite porphyry are 258 Ma, 238 Ma and 244 Ma, respectively (Salam et al., 2013). Based on the chemical compositions and ages, andesite lava, post-mineralization andesite dike and granodiorite porphyry are thought to be different igneous activities.

Chapter 4: Au mineralization

Au mineralization occurs in from the north (A pit and Q prospects) through central (Ke, Kw, C, H and D pits) to south (B prospects) of the area (Fig. 3.1). On the other hand, Cu-Mo mineralization occurs in the south at theN and V prospects. In order to elucidate the relationship between gold and Cu-Au mineralization in the Chatree deposit, this study was carried out on the -A pit and Q and B prospects for the Au mineralization and the N and V prospects for the Cu-Mo mineralization.

The Au mineralization is characterized by veins, veinlets and strockwork breccias. Brecciated veins are the dominant structure of the Au-bearing quartz veins in the Chatree deposit. A total of 150 samples of ores were collected from drill cores and outcrop in open pits. The mineral assemblage was determined by observation using microscope, XRD (Rigaku MiniFlex) and EPMA (JEOL SUPERPROBE 733 EPMA) at Akita University. The Au-bearing quartz veins at the A pit, Q and B prospects are characterized by quartz, adularia, illite, calcite and sulfide minerals. The Au-bearing quartz veins can be classified into five stages of the Q prospect on the basis of crosscutting relationships (Tangwattananukul et al., 2014).

4.1 Vein, mineral paragenesis and quartz texture of the Q, A and B prospects

4.1.1 Vein and mineral paragenesis of the Q prospect

Based on crosscutting relationships of quartz veins and mineral assemblages, gold mineralization at the Q prospect is classified into five stages (Figs. 4.1 and 4.2). The mineral assemblages of those stages are summarized as follows.

Stage Q1: Dark-gray quartz veins and veinlets; consisting dominantly of microcrystalline quartz with small amounts of illite, calcite, adularia, pyrite, electrum, chalcopyrite and sphalerite. Banded and brecciated structures are common. Microcrystalline quartz is intimately associated with a large amount of pyrite and small amounts of chalcopyrite, sphalerite and electrum.

Stage Q2: Quartz veins and veinlets; consisting chiefly of quartz with small amounts of calcite, illite, adularia, pyrite and chalcopyrite. Quartz in this stage is characterized by a banded structure. Comb texture is the dominant texture.

Stage Q3: Quartz veins and veinlets; associated with trace amounts of calcite, adularia, illite, chlorite, pyrite and electrum. Banded structure is common in this stage. Grain size of quartz varies from 20 to 50 μm in diameter. Texture of quartz is characterized by chalcedonic and mosaic textures. Small amounts of pyrite and electrum were precipitated on the mosaic texture in this stage.

Stage Q4: Quartz-calcite veins and stockworks; consisting mainly of quartz and calcite with a small amount of illite and lesser amounts of chlorite, adularia and laumontite. Laumontite is characterized by platy and elongated prismatic crystals. Laumontite coexists with quartz, illite and calcite (Fig. 6). This fact suggests that laumontite, quartz, illite and calcite were precipitated during gold mineralization in this stage. When compared with ore minerals in the other stages, larger amounts of pyrite,

sphalerite, chalcopyrite and electrum were precipitated in this stage. Brecciated structure is common in this stage. The quartz is characterized by flamboyant and comb textures. Flamboyant and comb textures were formed in the early and late parts of this stage, respectively (Fig. 4.3 and Fig. 4.4).

Stage Q5: This stage is divided into early and late periods. The bands in the early period are characterized by greenish fine-grained quartz. The greenish fine-grained quartz consists of large amounts of quartz and small amounts of adularia, calcite and pyrite. The bands in the late period consist of a large amount of calcite with a small amount of quartz. Banded structure is composed of fine-grained quartz (10-30 μm) showing mosaic texture. Calcite is characterized by coarse-grained crystals (100-250 μm).

Electrum was dominantly precipitated in Stages Q1 and Q4.

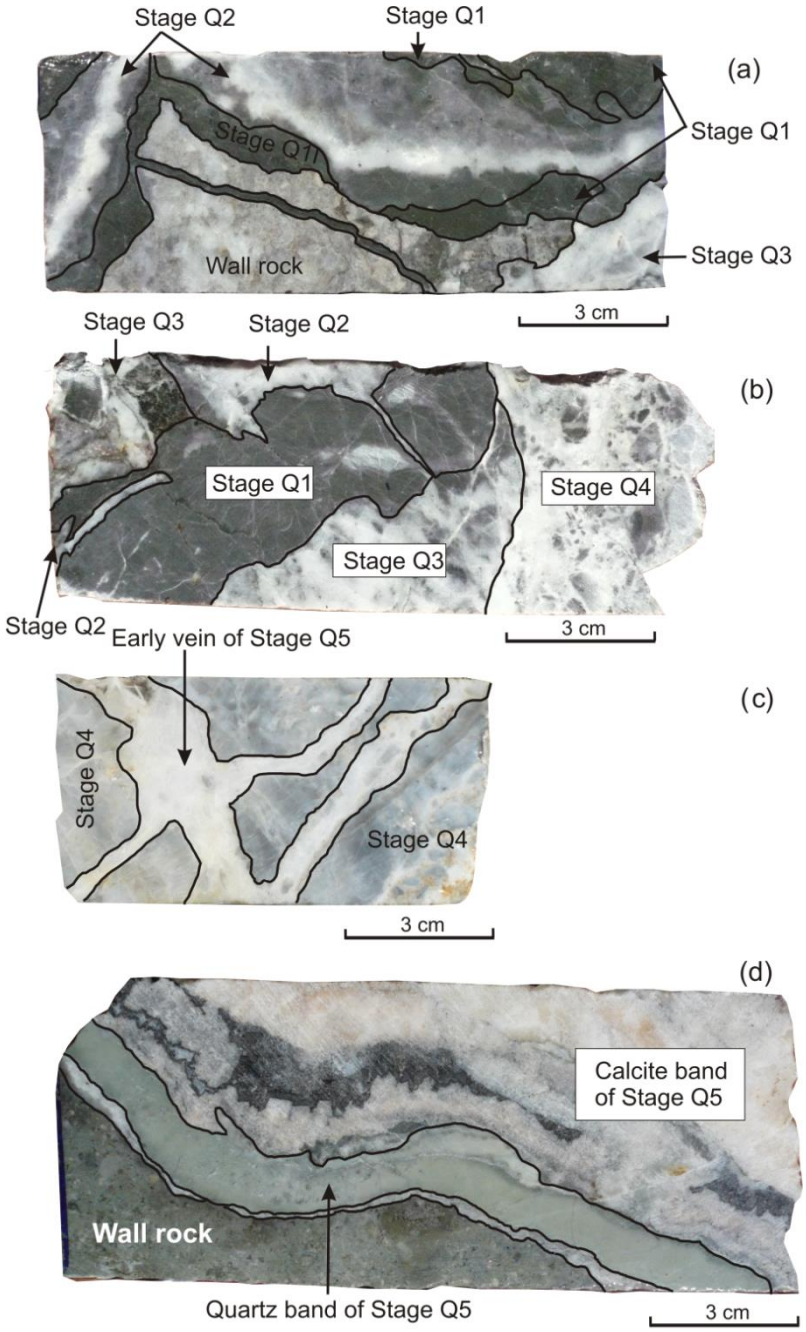

Figure 4.1 Photographs showing mineralization stages of the Au-bearing quartz veins at the Q prospect. (a) Quartz veins of Stage Q1 consist of light- to dark-grey quartz. Light-grey to white quartz of Stage Q2 and Q3 cut quartz veins of Stage Q1. (b) Quartz veins composed of brecciated quartz in Stage Q4 cut quartz veins of Stages Q1 and Q3. (c) Calcite veins of Stage Q5 cut quartz veins of Stage Q4. (d) The quartz band was formed before formation of the calcite in Stage Q5.

Table 5 Mineral assemblage of the Au-bearing quartz veins of the Q prospect determined by X-ray diffraction (XRD) analysis.

Sample no.	Stage	Qtz	Ad	Ill	Chl	Dol	Cc	Lmt	Py
Vg-1ed	Q1	◎	△				–		○
Vg-1Lg	Q1	◎	○				–		○
Vg-1IIw	Q1	◎	○	–			–		○
Qgs-3II	Q2	◎	–				○		△
Hbx-2II	Q2	◎	△				△		–
Qc-2II	Q2	◎	△				△		△
Qgs-1III	Q3	◎	–				○		△
Qs-1III	Q3	◎	–				–		△
Qs-2III	Q3	◎	△				△		△
Qs-3III	Q3	◎	△				△		△
Qs-4III	Q3	◎	–				△		–
Qm-1III	Q3	◎	–		–		○		–
Q-III	Q3	○	–		–		△		–
Qgs-2III	Q3	◎	–		–				–
Qs-6	Q3	◎	△		△		–		△
Hbx-1IV	Q4	◎	○		△		△		△
Hbx-2IV	Q4	◎	△	△			◎	△	△
Hbx-3IV	Q4	◎	○	△			△		△
Hbx-5IV	Q4	◎	△	△			△		△
Qm-2	Q5	△		–			◎		
Qc-4B	Q5	△					◎		
Qc-4C	Q5	△					◎		
Qm-1	Q5	△	–				◎		
Qc-4A	Q5	◎	△				–		–

◎ large ○ moderate △ minor – trace

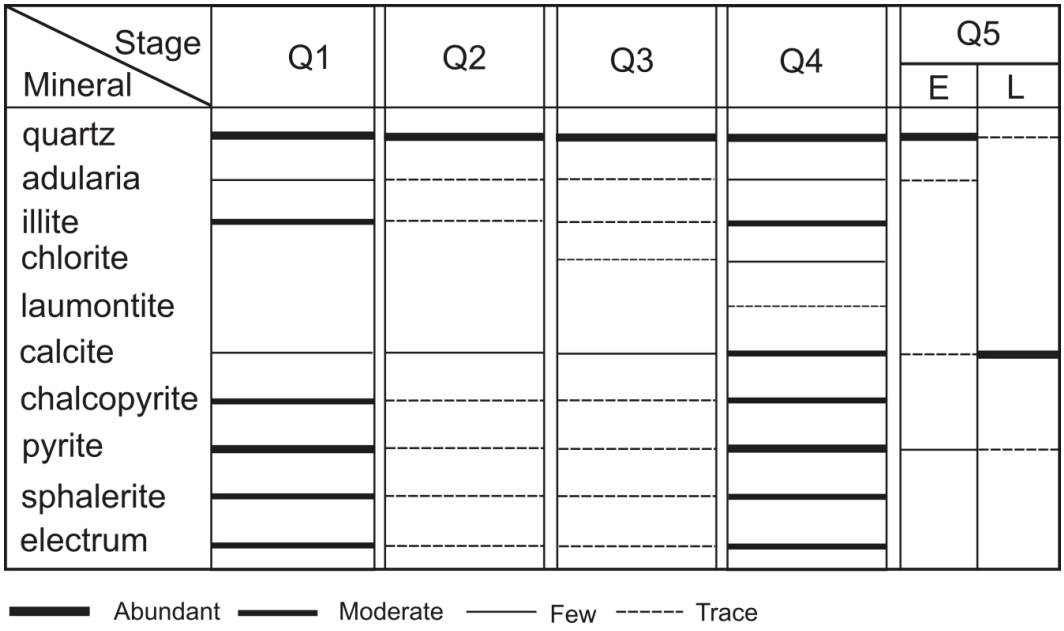

Figure 4.2 Paragenetic sequence of gold mineralization at the Q prospect in the Chatree deposit.

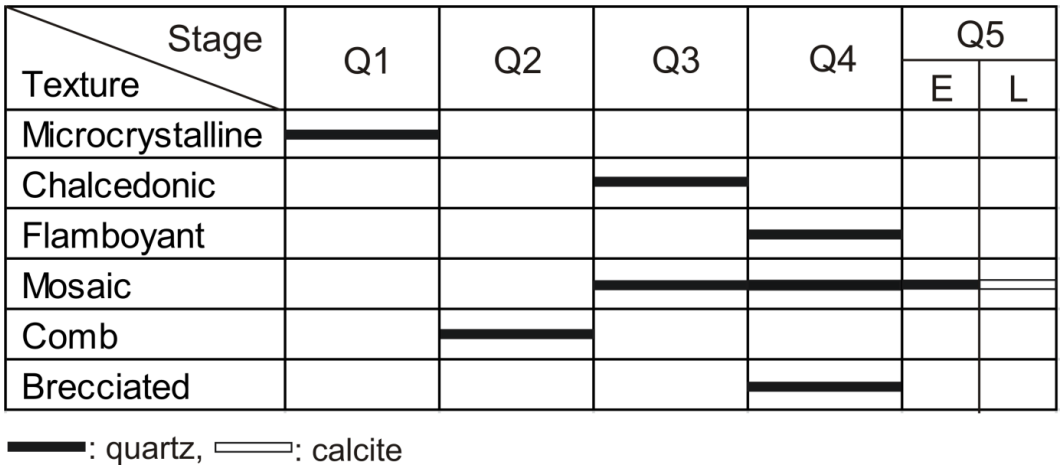

Figure 4.3 Classification of textures of quartz and calcite according to progress of mineralization stages.

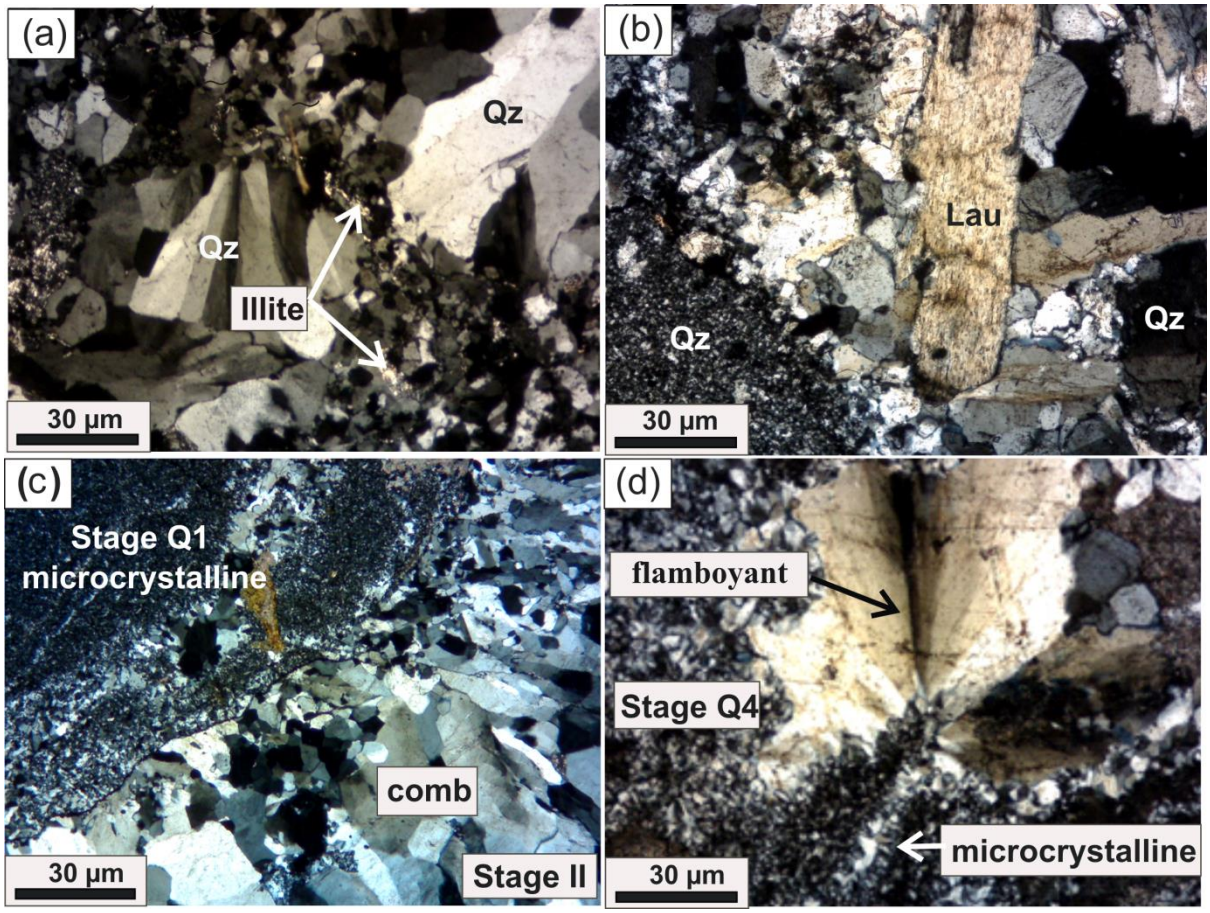

Figure 4.4 Photomicrographs showing representative minerals in the Q prospect. (a) Quartz in Stage Q4 coexists with illite. (b) Laumontite with quartz, calcite and illite in Stage Q4. (c) Aggregate of microcrystalline quartz of Stage Q1 and comb quartz of Stage Q2. (d) Flamboyant texture of quartz showing a fan-like shape and undulatory extinction. Flamboyant quartz of Stage Q4 coexists with fine-grained quartz crystals.

4.1.2 Vein and mineral paragenesis of the A pit

The Au-bearing quartz veins of the A prospect are divided into five stages from Stages A1 to A5 on the basis of crosscutting relationships of quartz veins and mineral paragenesis (Fig. 4.5 and 4.6). The characteristics of these stages are summarized below.

Stage A1: Light to dark-gray quartz veins and veinlets; consist of a large amount of microcrystalline quartz and small amounts of adularia, pyrite, electrum, chalcopyrite and sphalerite. Quartz veins show alternation of quartz layers with different pyrite content. Pyrite of Stage A1 shows dendritic texture. The dendritic pyrite contains a larger amount of electrum (Fig. 4.7). Banded and brecciated structures are common in this stage. Light to dark-gray microcrystalline quartz is associated with a large amount of pyrite and with small amounts of chalcopyrite, sphalerite and electrum.

Stage A2: Quartz veins and veinlets; consist of a large amount of quartz with small amounts of illite, adularia, calcite, pyrite and chalcopyrite. The quartz is fine- to coarse-grained (20 μm -1 mm in diameter) and shows comb texture. The comb texture of quartz is oriented perpendicular to the wall of vein (Fig. 4.8A). .

Stage A3: Quartz veins and veinlets; associated with trace amounts of calcite, illite, adularia, chlorite, pyrite and electrum. Quartz is fine-to-medium-grained (20-50μm in diameter). The texture of quartz is characterized by mosaic and comb textures. The mosaic texture is characterized by quartz crystals showing a jigsaw texture.

Stage A4: Quartz veins and stockworks consist of large amounts of quartz and calcite with small amounts of illite, chlorite, adularia, barite, dolomite, pyrite, sphalerite, chalcopyrite, tetrahedrite, galena and electrum. Barite occurs as veinlet (1-2 mm) and cut the Au-bearing quartz vein of Stage A1 (Fig. 4.7). Barite exhibits subhedral to euhedral shape, is medium-to-coarse-grained and coexists with quartz, calcite and

illite. Electrum occurs as inclusions in pyrite, and pyrite coexists with chalcopyrite and sphalerite. Several quartz textures are recognized in this stage such as flamboyant, comb, pseudoacicular, and ghost sphere (Figs. 4.8B-D). The flamboyant texture is characterized by the radial flamboyant extinction of individual quartz crystals with rounded crystal outline. The ghost sphere occurs within microcrystalline quartz as spherical distribution of impurities. The psedoacicular display a radial acicular appearance and linear arrangements of fine-grained quartz (Fig. 4.8).

Stage A5: Calcite veins and veinlets are composed of a large amount of calcite with small amounts of quartz and pyrite. Quartz is fine-grained and exhibits mosaic texture.

The Au-bearing quartz veins of Stages A1 and A4 have high gold content.

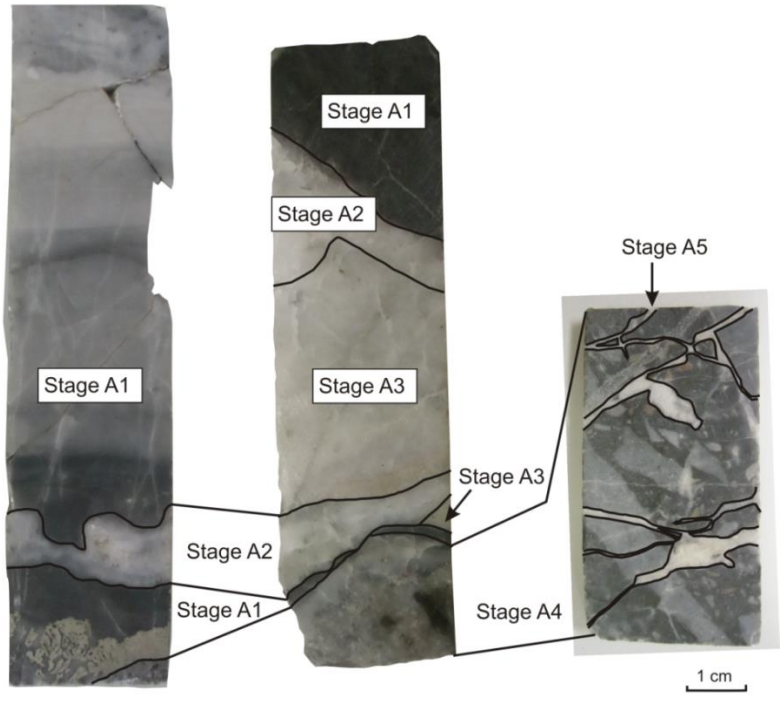

Figure 4.5 Photographs showing mineralization stages of the Au-bearing quartz vein at the A pit.

Table 6 Mineral assemblage of the Au-bearing quartz veins of the A pit determined by X-ray diffraction (XRD) analysis.

Sample no.	Stage	Qtz	Ad	Ill	Chl	Dol	Cal	Brt	Py
A7	A1	◎	△		–		△		△
A14-3	A1	◎	△				△		○
A14Lg	A1	◎	△				△		△
A15Lg	A1	◎	△	–			△		△
An8I	A1	◎	○	△			△		△
A12Lg	A1	◎	△	△	–		–		△
A13II	A2	◎	△	–			△		△
A15II	A2	◎	△				△		–
A11III	A3	◎	△	–			△		△
A9III	A3	◎	–				△		△
A10IV	A4	◎	△		–	–	○		△
A12IV	A4	◎	△	△			○		△
A12	A4	○	△	△	△		○	△	–
A	A4	◎	△	–			○		–
An2	A4	◎	△	△	△	–	–		–
A16IV	A4	◎	○	△	△	–	○		△
An3	A5	◎					◎		
An4	A5	◎					◎		–

◎ large ○ moderate △ minor – trace

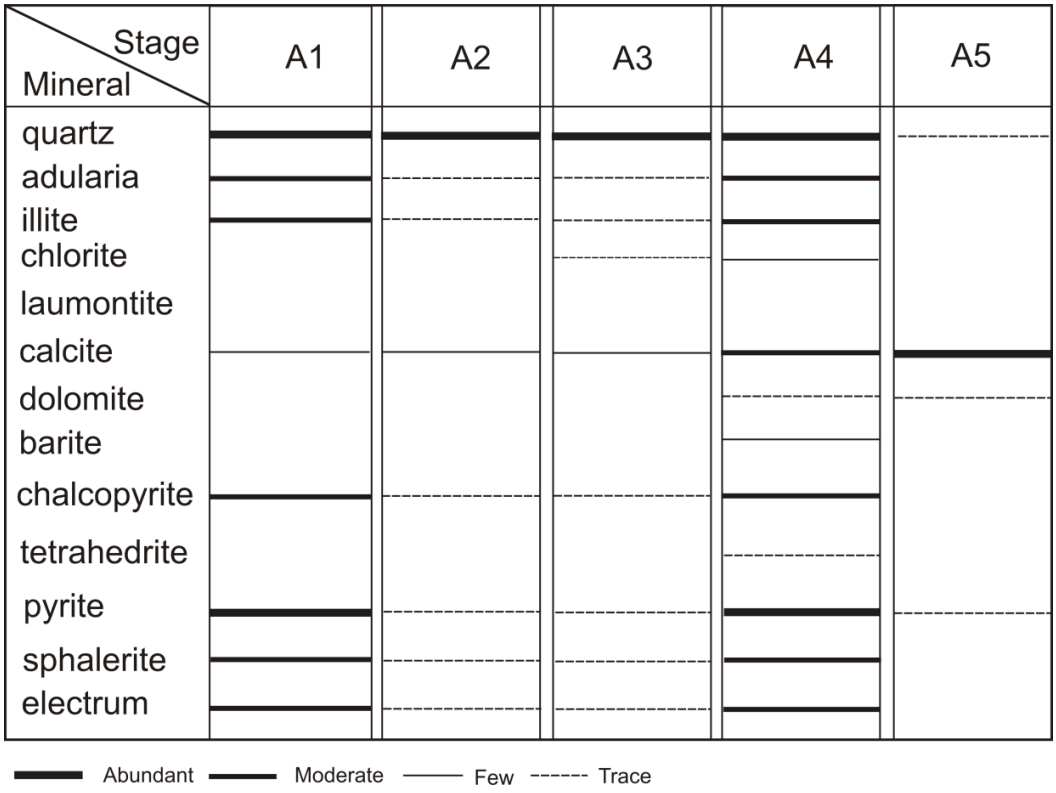

Figure 4.6 Paragenetic sequence of gold mineralization at the A pit in the Chatree deposit.

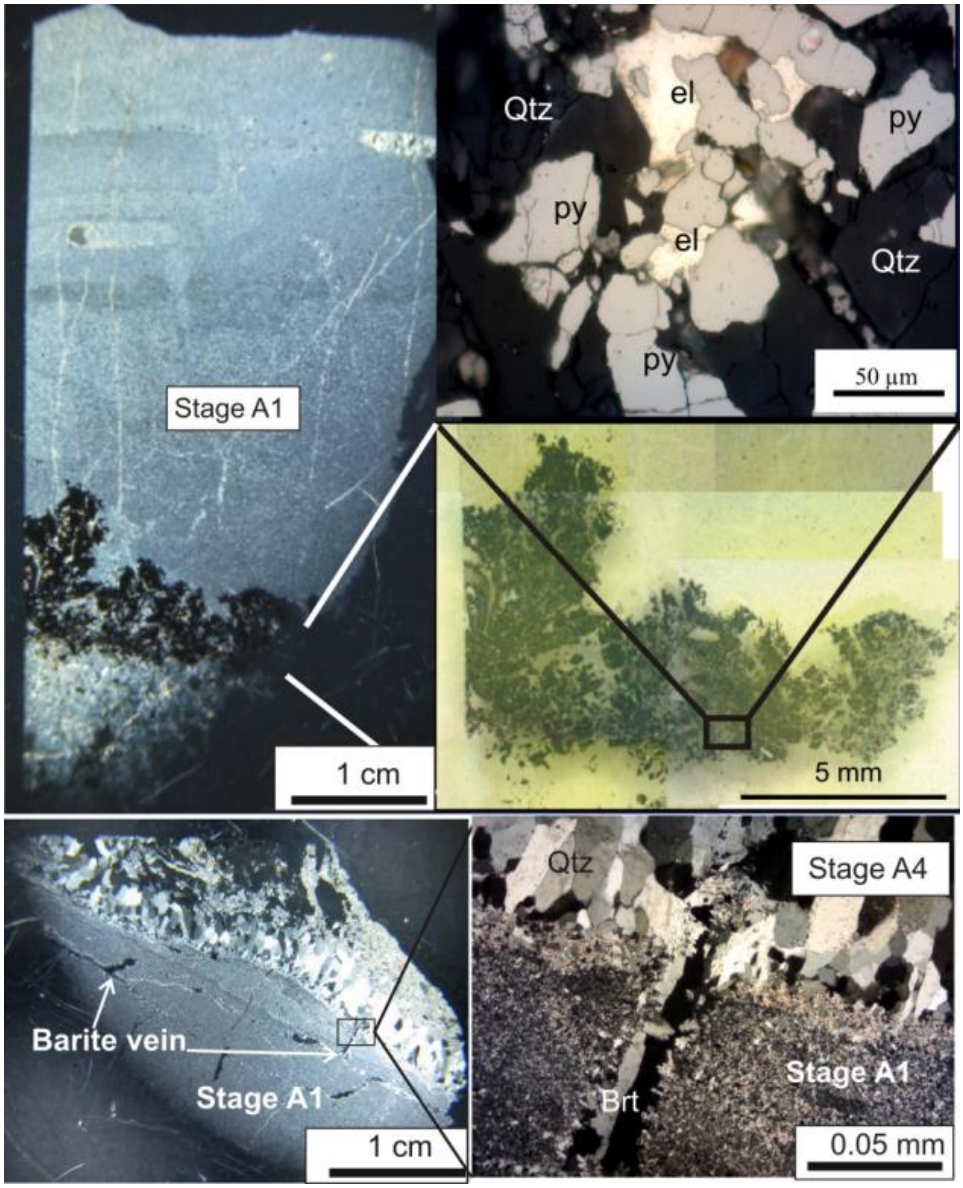

Figure 4.7 Photographs showing the Au-bearing quartz veins of Stage A1 associated with large amounts of electrum. Barite vein cut Au-bearing quartz vein of Stage A1.

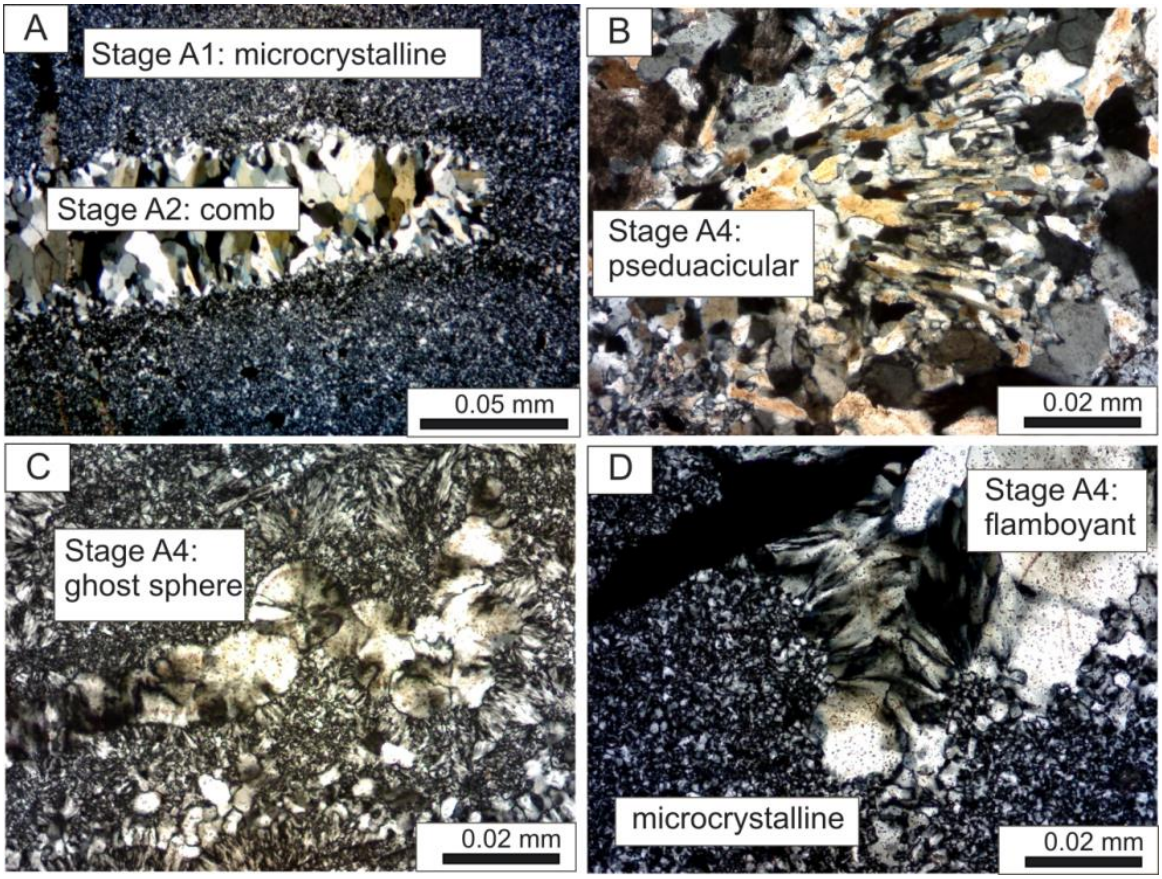

Figure 4.8 (A) Photomicrographs showing microcrystalline quartz of Stage A1 and comb quartz of Stage A2. (B) - (D) The Au-bearing quartz vein of Stage A4 consists of various quartz textures. (B) Aggregates of quartz show acicular shape. (C) Ghost sphere occurs within microcrystalline quartz as cloudy spheres. (D) Flamboyant texture of quartz is typical texture of Stage A4. The texture is exhibited by the wavy extinction of individual quartz crystal. Flamboyant texture is common in Stage Q4 and A4 at the Q and A prospects.

4.1.3 Vein and mineral paragenesis of the B prospect

The Au-bearing quartz veins of the B prospect are separated into five stages on the basis of crosscutting relationship (Fig. 9). The mineral assemblages of those stages are summarized as follows.

Stage B1: Light to dark-gray quartz veins and veinlets; consist of a large amount of microcrystalline quartz and small amounts of illite, calcite, dolomite, chlorite, adularia, pyrite, electrum, chalcopyrite and sphalerite. Microcrystalline quartz is common in this stage and associated with fine-grained pyrite.

Stage B2: Quartz veins and veinlets; consist of a large amount of quartz with small amounts of calcite, dolomite, chlorite, adularia, pyrite and chalcopyrite. The medium-tocoarse-grained quartz exhibits comb texture.

Stage B3: Quartz veins and veinlets; composed of quartz with trace amounts of dolomite, calcite, chlorite, adularia and pyrite. Quartz is medium-grained and exhibits mosaic texture. Stage B4: Quartz veins and stockworks; consist of a large amount of quartz and dolomite with small amounts of chlorite, calcite, illite, adularia, pyrite, sphalerite and chalcopyrite. The size of quartz is fine- to coarse-grained showing microcrystalline and feathery quartz texture. The feathery texture displays plumose of fibrous silica (Fig. 4.10).

Stage B5: Dolomite veins and veinlets; composed of a large amount of dolomite and small amount of calcite and quartz.

Table 7 Mineral assemblage of the Au-bearing quartz veins of the B prospect determined by X-ray diffraction (XRD) analysis.

Sample no.	Stage	Qtz	Ad	Ill	Chl	Dol	Cc	Py
B15I	B1	◎	△		△		△	△
B29Py	B1	◎	○	–		○		△
B29I	B1	◎	○	–		○		△
BC-1	B2	◎	△					–
B9II	B2	◎	△		△	–	–	△
B29III	B3	◎	△		–	○	–	△
B2	B4	◎	△	–	–	△		△
B10	B4	◎	△		△	–	△	○
B13IV	B4	◎	△		△	△		△
B14IV	B4	◎	–		△	○	△	△
B29V	B5	○	–	–		◎	○	–

◎ large ○ moderate △ minor – trace

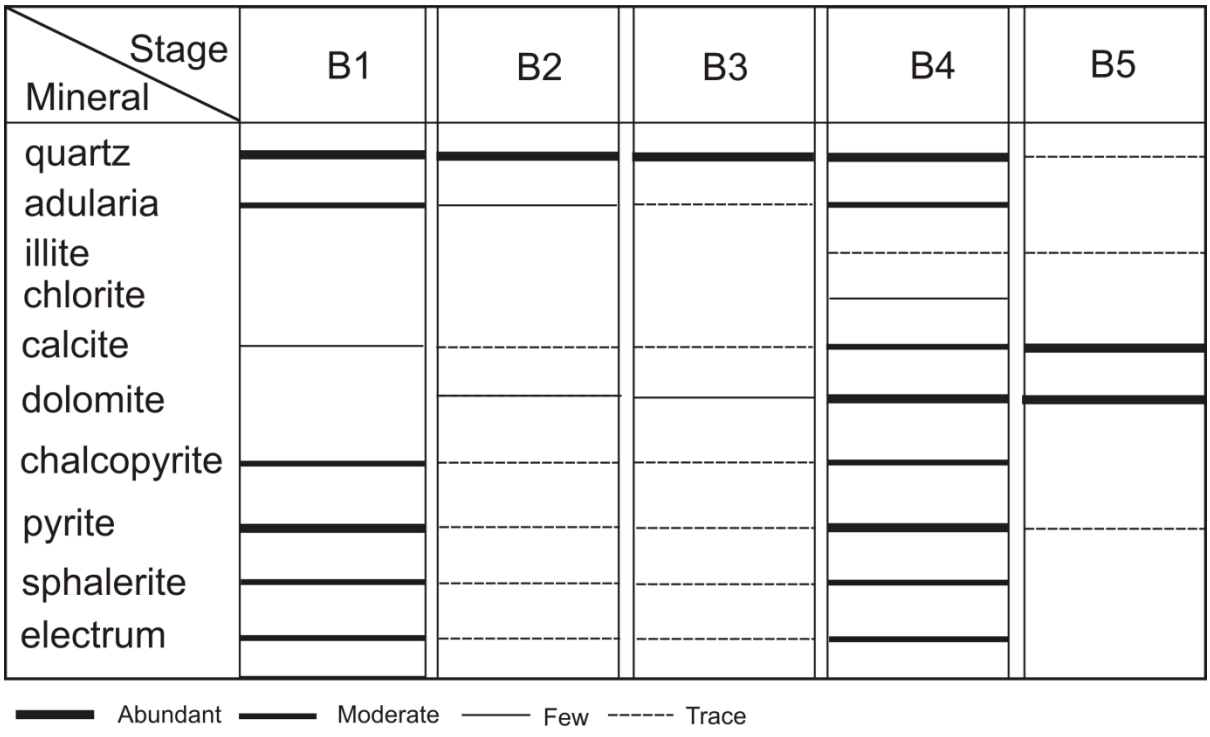

Figure 4.9 Paragenetic sequence of gold mineralization at the B prospect in the Chatree deposit.

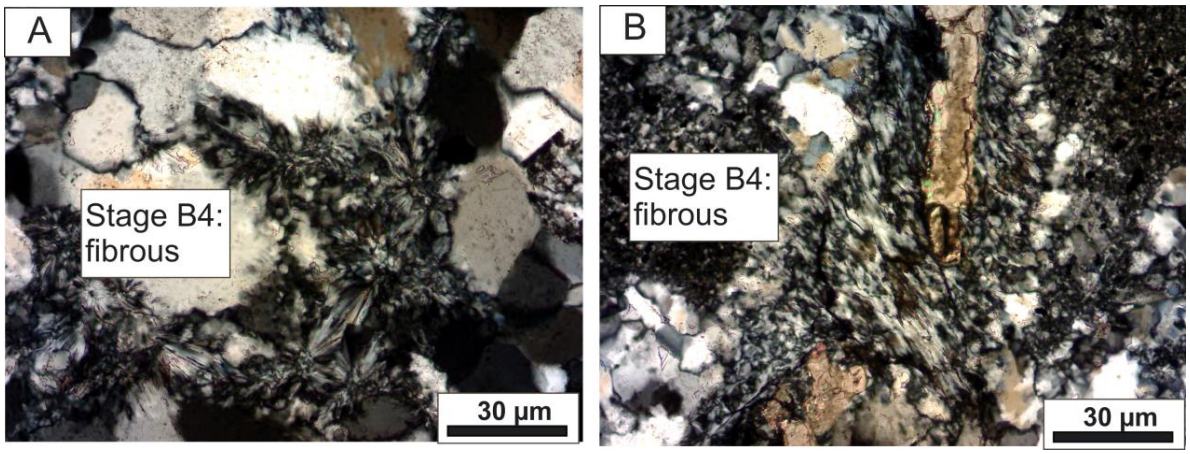

Figure 4.10 (A) The feathery texture is characterized by plumose of fibrous silica in Stage B4 of B prospect. This texture is developed on the margin of quartz crystals. (B) Feathery texture as characterized by plumose of fibrous silica.

4.2 Variation of K_2O, CaO, Au, Cu and Zn contents in ores

The chemical compositions of Au-bearing ores from the A pit, Q and B prospects were examined on the basis of classification of stages and quartz textures. The chemical compositions of ores were determined by atomic absorption spectroscopy (AAS) and inductively coupled plasma mass spectrometry (ICP-MS) at Akita University and by the proton-induced X-ray emission (PIXE) method at Nishina Memorial Cyclotron Center. Analytical procedures of ICP-MS and PIXE were described by Satoh et al. (1999) and Sera and Yanagisawa (1992), respectively.

The Au-bearing quartz veins from Stages Q1 to Q5, A1 to A5 at the Q prospect and A pit show large variations in K_2O, CaO, Au, Cu and Zn contents (Fig. 4.11). The K_2O content is high in quartz veins of Stages Q1 – Q4 and Q5 at the Q prospect and A1 - A4 at the A pit. The CaO content is high in quartz veins of Stages Q1 and Q4 except for the calcite band in Stage Q5. Gold, Cu and Zn contents are slightly high in quartz veins of Stages Q1 and Q4 at the Q prospect and Stages A1 and A4 at A pit. Gold and K_2O contents and Au and CaO contents of the ores from Stages Q1 to Q4 show positive correlations. Gold and K_2O contents of the ores from Stages A1 to A4 also show positive correlation. The correlations suggest that electrum was precipitated with illite, adularia and calcite.

Table 8 Chemical compositions of the Au-bearing quartz veins at the A pit and Q and B prospects.

Sample no.	Stage	Ca (ppm)	K (ppm)	Au (ppm)	Cu (ppm)	Zn (ppm)
Q prospect						
Vg-1eu	Q1	8480	34400	1.00	35.9	11.1
Vg-1Lg	Q1	4440	801000	1.10	26.3	191
Vg-1ed	Q1	638000	12100	1.90	11.9	23.8
Vg-1IIw	Q2	2720	1030	2.39	29.3	68.9
Qgs-3II	Q2	4380	540	0.45	20.4	29.9
Q-1III	Q3	3310	280	0.58	11.0	15.3
Qgs-1III	Q3	3180	508	0.25	10.4	19.8
Qgs-2III	Q3	2100	508	0.55	22.6	22.6
Hbx-1IV	Q4	bd	11700	bd	35.6	28.1
Hbx-2IV	Q4	10100	600	0.58	6.90	11.2
Hbx-3IV	Q4	7040000	2540000	1.45	23.7	30.0
Qm-2V	Q5	3740	3860	bd	1.68	16.4
Qc-4VI	Q5	36800	bd	bd	13.7	303
A pit						
A-14-1	A1	2210	13900	3.32	4130	67.6
A-14-2	A1	430	76.2	93.2	146	33.0
A-14-3	A1	9000	10500	4.52	117	23.9
A-14-4	A1	1330	9000	0.01	29.3	70.7
A-13II	A2	38300	20900	0.01	2.81	27.0
A-15II	A2	13900	3610	0.03	2.26	29.2
A-9III	A3	4040	56.4	0.01	1.47	32.1
A-11III	A3	1540	3530	1.08	6.08	18.4
A-10IV	A4	22800	1730	0.16	5.28	21.2
A-16IV	A4	9940	14000	0.69	14.6	41.7
B prospect						
B15IP	B1	28600	6280	1.89	117	23.9
B-29Py	B1	9780	6300	bd	29.3	70.7
B-9I	B1	1270	7190	0.01	2.81	27.0
B-29II	B2	12300	5120	0.03	2.26	29.2
B-29III	B3	81900	13300	0.01	1.47	32.1
B-10IV	B4	3190	13900	1.08	6.08	18.4
B-14IV	B4	87100	9420	0.16	5.28	21.2
B-29V	B5	1660000	7980	0.69	14.6	41.7

bd, below detection limit

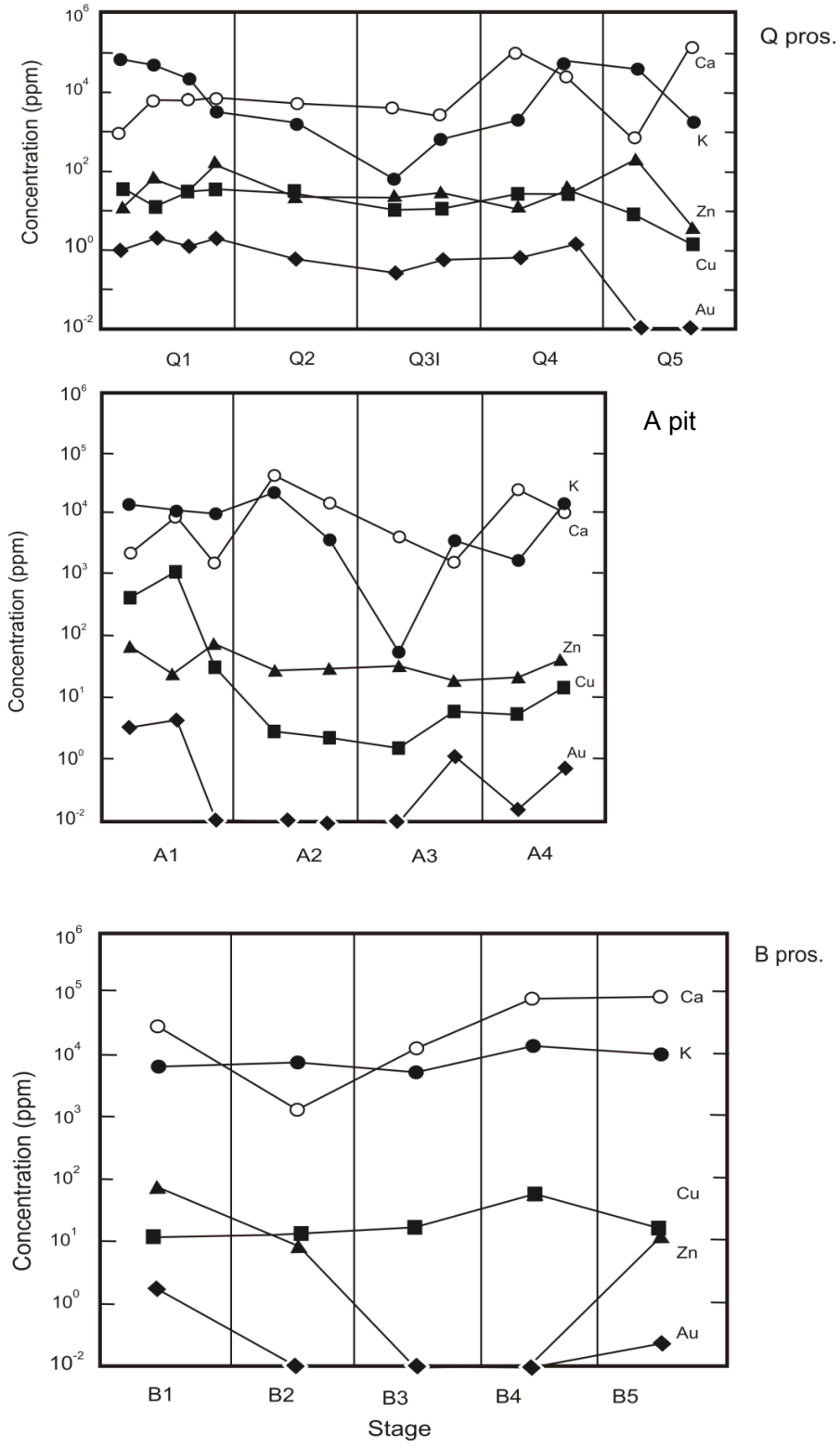

Figure 4.11 Diagrams showing variations in K_2O, CaO, Au, Zn and Cu contents of the Au-bearing quartz veins from the A pit and Q and B prospects according to progress of mineralization.

4.3 Fluid inclusion study

Microthermometric measurements were performed on quartz vein using a Linkam heating-freezing stage (type-10002L) at Akita University. The temperature uncertainty in measurement of homogenization temperature (Th) and melting point of ice (Tm) is $\pm 0.2^0$C and $\pm 0.1^0$C, respectively.. Fluid inclusions in the Au-bearing quartz veins and the Cu-Mo-bearing quartz veins are composed of secondary fluid inclusions. The secondary fluid inclusions in the Au-bearing quartz veins at the A pit, Q and B prospects are small (10-30 μm) and can be separated into two fluid inclusions type such as monophase liquid fluid inclusions and liquid-rich fluid inclusions based on the classification by Roedder (1984). A small vapor bubble is present. Volume of vapor is less than 50% of the total volume in liquid-rich two-phase fluid inclusions (Fig. 4.12). Homogenization temperatures of secondary two-phases fluid inclusions of the A pit and Q and B prospects range from 85°C to 150°C, 105°C to 295°C and 150°C to 310°C, respectively (Fig. 4.13). Ranges of salinities of the secondary fluid inclusions of the Q prospect, A pit and B prospect are from 0.0 to 1.3, from 0.1 to 2.1 and from 0.2 to 2.3 wt% NaCl eq, respectively. Salinities of secondary fluid inclusions are between meteoric water and seawater.

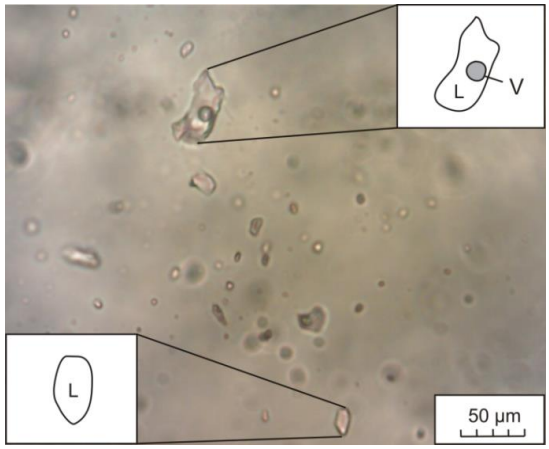

Figure 4.12 Photomicrograph of fluid inclusions in the Au-bearing quartz vein from the A pit.

Table 9 Homogenization temperatures and salinities of fluid inclusions from the A pit and Q and B prospects.

Prospect	Sample no.	Stage	No	T_h (°C)	T_m(°C)	wt% NaCl eq.	Type
Q	Hbx-2IV	Q4	1	89	-0.5	0.2	LV, S
			2	112	-0.7	0.8	LV, S
			3	123	-1.0	1.6	LV, S
			4	137			LV, S
Q	Qs-4	Q5	5	86	-0.6	0.3	LV, S
			6	107			LV, S
			7	140			LV, S
			8	141	-1.2	2.2	LV, S
			9	144			LV, S
			10	145	-1.1	1.9	LV, S
			11	150			LV, S
A	A14-1	A4	12	235	-1.7	0.9	LV, S
			13	263	-1.8	1.0	LV, S
			14	272	-0.9	0.2	LV, S
			15	255	-0.8	0.1	LV, S
			16	251	-0.8	0.1	LV, S
			17	224	-0.9	0.2	LV, S
			18	240	-2.1	1.3	LV, S
			19	269	-1.9	1.1	LV, S
			20	262	-1.6	0.8	LV, S
			21	241	-2.2	1.4	LV, S
			22	257	-0.8	0.1	LV, S
			23	257	-2.3	1.5	LV, S
			24	262	-1.7	0.9	LV, S
			25	270	-0.8	0.1	LV, S
A	A14-2	A4	26	281	-2.2	1.4	LV, S
			27	278	-1.3	0.6	LV, S
			28	286	-1.5	0.7	LV, S
			29	285	-1.2	0.5	LV, S
			30	259	-1.3	0.6	LV, S
			31	286	-1.6	0.8	LV, S
			32	306	-0.9	0.2	LV, S
			33	220	-0.8	0.1	LV, S
			34	135	-2.3	1.5	LV, S
			35	135	-1.7	0.9	LV, S
			36	133	-0.8	0.1	LV, S
A	A14-3	A4	37	135	-2.2	1.4	LV, S
			38	131	-1.3	0.6	LV, S
			39	130	-1.5	0.7	LV, S
			40	104	-1.3	0.6	LV, S
			41	89	-2.2	1.4	LV, S
			42	71	-2.1	1.3	LV, S
			43	102	-2.0	1.2	LV, S
			44	151	-1.8	1.0	LV, S
			45	143	-2.5	1.7	LV, S
			46	145	-2.3	1.5	LV, S
			47	153	-1.6	0.8	LV, S
			48	150	-1.7	0.9	LV, S
			49	155	-1.1	0.4	LV, S
B	BC-1	B4	50	253	-1.0	0.5	V, S
			51	310	-0.9	0.3	LV, S
			52	241	-1.0	0.5	LV, S
			53	177	-0.8	0.2	V, S
			54	129	-0.9	0.3	LV, S
			55	167	-0.8	0.2	V, S
			56	245	-1.1	0.6	LV, S
			57	180	-2.3	2.5	V, S
			58	274	-1.0	0.5	LV, S
			59	212	-2.1	2.2	LV, S
			60	164	-0.9	0.3	LV, S

L, liquid; V, vapor; S, secondary fluid inclusions; blank means no data

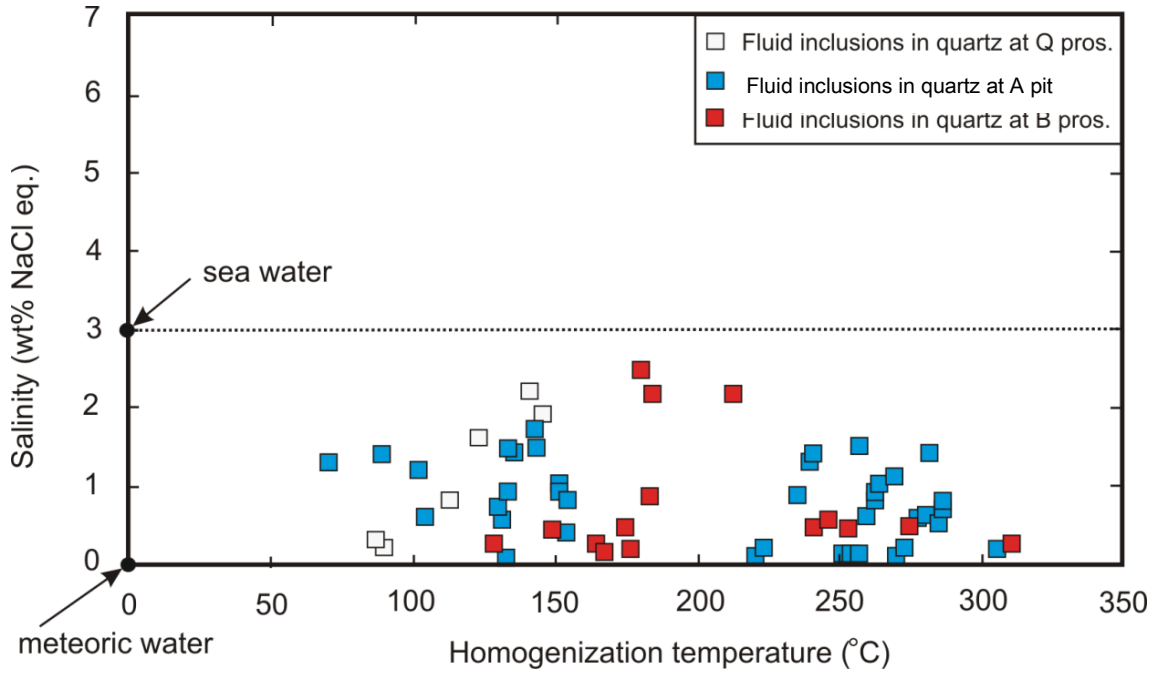

Figure 4.13 Homogenization temperatures and salinities of secondary fluid inclusions in quartz of Stage Q4 from the A pit and Q and B prospects.

4.4 Oxygen isotopic ratios of the Au-bearing quartz

Oxygen and carbon isotopic ratios of the Au-bearing quartz veins were analyzed by a mass spectrometer (Isoprim Dual Intel; Isoprime Limited) at Akita University. Measurement of oxygen isotopic ratios of quartz was carried out by the F_2-technique described by Kita and Matsubaya (1983). Pure quartz fraction were obtained for oxygen isotopic ratios by procedure of Tangwattananukul et al. (2014). The $\delta^{18}O$ are given relative to SMOW (Standard Mean Ocean Water). Analytical precision on the basis of one standard deviation is within ± 0.2 ‰.

The $\delta^{18}O$ values of quartz were examined according to the progress of mineralization stages together with paragenesis from the A pit and Q and B prospects (Table 1). The $\delta^{18}O$ values of the Au-bearing quartz veins of the A pit and Q and B prospects from Stages Q1 to Q5, A1 to A5 and B1to B4 are shown in Fig. 4.13, respectively. The $\delta^{18}O$ values of Au-bearing quartz veins of the Q prospect range from +9.9 to +15.0‰ (Tangwattananukul et al., 2014). The $\delta^{18}O$ values of the Au-bearing quartz veins of Stage Q4 were clearly increased compared with those of earlier stage. The $\delta^{18}O$ values of the Au-bearing quartz veins of the A pit range from +11.9 to +13.4‰ except for the $\delta^{18}O$ values of the Au-bearing quartz veins of Stage A1 (+14.0‰). The $\delta^{18}O$ values of the Au-bearing quartz veins of the B prospect range from +12.4 to +14.1‰. The $\delta^{18}O$ values of the Au-bearing quartz veins of Stage B1 to B4 slightly increased from early to later stage. The $\delta^{18}O$ values of Au-bearing quartz veins slightly increased from the Au-bearing quartz veins in the Q prospect and A pit (north) to B (south) prospect.

The $\delta^{18}O$ values of the hydrothermal solution were calculated from the $\delta^{18}O$ values of quartz of the Au-bearing quartz veins at 200°C and 250°C (Fig. 4.14)

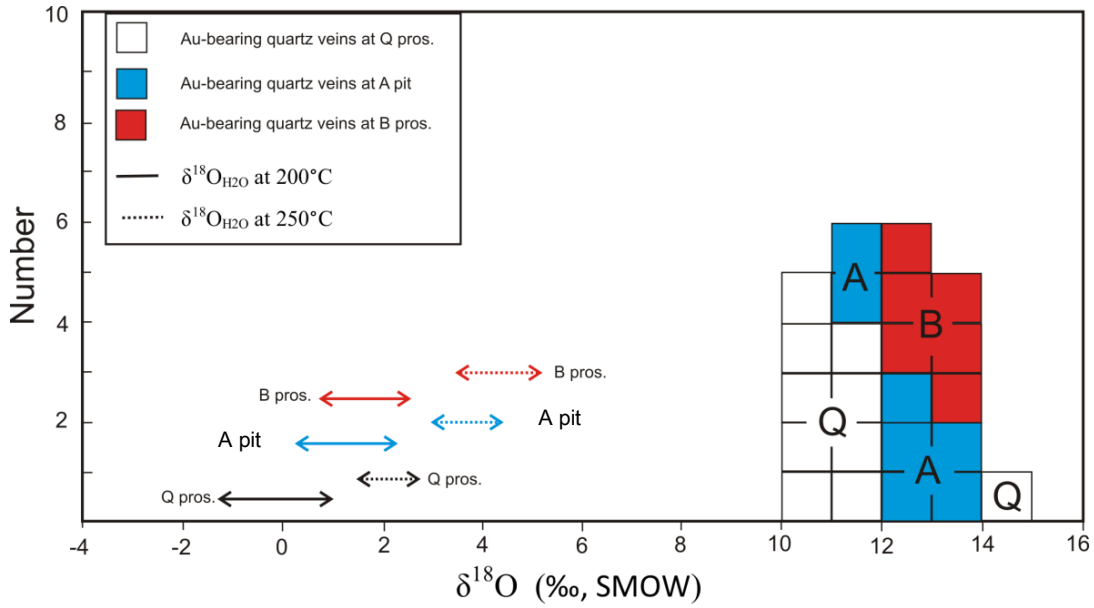

Figure 4.14 Histogram of $\delta^{18}O$ values of quartz showing the increase in $\delta^{18}O$ values of quartz from the Q to B prospects. The $\delta^{18}O_{H2O}$ values of hydrothermal solution were calculated at temperatures of 200^0C and 250^0C.

Samples for analysis of the $\delta^{18}O$ values of altered andesite rock of the A pit, Q and B prospects were collected at portions within distance of 5 mm from margin of veins. The $\delta^{18}O$ values of altered rock of the A pit and Q and B prospects are +11.4, +9.7 and +11.5‰, respectively.

Table 10 $\delta^{18}O$ values of quartz according to the progress of mineralization and morphology of quartz texture of the Au-bearing quartz veins from the A pit and Q and B prospects.

Sample no.	Stages	$\delta^{18}O_{quartz}$ (‰)	Quartz texture	prospect
Vg-1eu	Q1	10.7	microcrystalline	Q
Vg-1Lg	Q1	10.4	microcrystalline	Q
Vg-1IIw	Q1	11.3	comb	Q
Qgs-3II	Q2	10.9	comb	Q
Q-III	Q3	11.0	mosaic	Q
Hbx-1	Q4	11.0	comb and brecciated	Q
Hbx-3IV	Q4	9.9	comb and brecciated	Q
Hbx-3IV	Q4	10.9	comb and brecciated	Q
Hbx-3IV	Q4	11.2	comb and brecciated	Q
Hbx-2IV	Q4	14.4	flamboyant and brecciated	Q
Hbx-2IV	Q4	14.6	flamboyant and brecciated	Q
Hbx-2IV	Q4	14.8	flamboyant and brecciated	Q
Hbx-2IV	Q4	15.0	flamboyant and brecciated	Q
QC-4A	Q5	11.4	mosaic	Q
QC-4A	Q5	11.7	mosaic	Q
QC-4B	Q5	11.6	mosaic	Q
A14-1	A1	12.7	microcrystalline	Q
A14-2	A1	14.0	microcrystalline	Q
A7I	A1	11.9	microcrystalline	Q
A13II	A2	12.5	comb	A
A11III	A3	13.4	mosaic	A
A16IV	A4	11.8	brecciated	A
An3V	A5	12.1	mosaic	A
B15IP	B1	13.4	microcrystalline	B
BC1	B2	12.4	comb	B
B9II	B2	13.8	comb	B
B29III	B3	12.9	mosaic	B
B14IV	B4	12.4	brecciated	B
B29IV	B4	14.1	brecciated	B

4.5 Characteristics of the Au-bearing quartz veins at the Chatree deposit

The Au-bearing quartz veins of the Chatree deposit can be divided into five stages from Stage 1 to 5 based on cross-cutting relationship. The Au-bearing quartz vein of Stage 1 and the Au-bearing network-type vein of Stage 4 are common in the A pit and the Q and B prospects. The Au-bearing network-type vein of Stage 4 is composed of larger amount of pyrite, sphalerite, chalcopyrite and electrum. Laumontite is coexisting with quartz, calcite and illite in the Au-bearing quartz vein of the Stage Q4 at the Q prospect (Tangwattananukul et al., 2014). Barite coexists with quartz, calcite and illite of the Au-bearing quartz veins of Stage A4 at the A pit. Fine-to-medium-grained, anhedral-to-euhedral pyrite coexists with sphalerite, chalcopyrite and electrum. . Dolomite and chlorite are present in the Au-bearing quartz veins of Stage B4 at the B prospect. Amounts of dolomite and chlorite increase from B prospect through the A pit and Q prospect.

4.5.1 Formation process of the Au-bearing quartz veins based on the morphology of quartz

The Au-bearing quartz veins of the A pit, Q and B prospects at the Chatree deposit show different grain sizes, textures of quartz and mineral assemblages. The quartz having high Au content in the Au-bearing quartz veins at the Q prospect is characterized by microcrystalline and flamboyant textures in Stages Q1 and Q4. Microcrystalline and flamboyant quartz in Stages Q1 and Q4 of the Q prospect were precipitated from the hydrothermal solution that was supersaturated with respected to silica (Tangwattananukul et al., 2014). Quartz veins in many epithermal deposit precipitates from solutions that were supersaturated with respect to quartz because of adiabatic steam loss and rapid cooling (Fournier et al., 1985). The dendritic pyrite

in microcrystalline quartz in Stage A1 of the A pit is characterized by fine-grained pyrite coexisting with chalcopyrite and electrum. The presence of dendritic pyrite also suggests rapid crystal growth from supersaturated hydrothermal solution. On the other hand, the network-type vein of Stage Q4, A4 and B4 is characterized by brecciated structure with quartz fragments of early stage. Brecciated structure is common in the Chatree gold deposit. The flamboyant texture in Stage Q4 and A4 in the Au-bearing quartz veins at the A pit and Q prospect, respectively, suggests the hydrothermal solution was supersaturated respect to amorphous silica (Dong et al., 1995). Ghost-sphere, pseudoacicular and flamboyant textures in the Au-bearing quartz vein of Stage A4 suggest possibility of deposition from amorphous silica . The texture of quartz of Au-bearing quartz veins of Stages Q1, Q4, A1 and A4 of the Q prospect and A pit suggests the precipitation of gold particles with amorphous silica(Dong et al., 1995).

4.5.2 Estimation of formation temperature

The hydrothermal system responsible for the formation of the Chatree deposit was interpreted in comparison with the framework of modern geothermal systems (Henley and Ellis, 1983; White and Hedenquist, 1995). The temperatures of the hydrothermal solution can be inferred from stabilities of minerals. Chlorite, illite and K-feldspar are stable above temperatures of 180°, 200° and 250°C, respectively (Henley et al., 1984; Inoue, 1995). Laumontite is also stable at temperatures from 90° to 230°C. The presence of laumontite, illite and chlorite in Stage Q4 of the Q prospect suggests that the formation temperature at Stage Q4 ranged from 200° to 230°C.

4.5.3 Estimation of $a_{Ca^{2+}}/(a_{H^+})^2$ and a_{K^+}/a_{H^+} ratios in hydrothermal solution

Activity ratios of $a_{Ca^{2+}}/(a_{H^+})^2$ and a_{K^+}/a_{H^+} of hydrothermal solution at 200°C were estimated on the basis of the stability of laumontite. Stability boundaries of minerals in the system of K_2O-CaO-Al_2O_3-SiO_2-H_2O were calculated from the reactions shown in Table 6 and Figure 4.15. The $a_{Ca^{2+}}/(a_{H^+})^2$ and a_{K^+}/a_{H^+} ratios were estimated from the following reactions:

$$2\text{Illite} + 6\text{Quartz} + 12H_2O + 3Ca^{2+} = 3\text{Laumontite} + 2K^+ + 4H^+.$$

The equilibrium constants of the reactions (log K) were calculated using the SUPCRT92 database (Johnson et al., 1992) (Table 4). The $a_{Ca^{2+}}/(a_{H^+})^2$ ratio of hydrothermal solution forming quartz veins at Stage Q4 was estimated to range from $10^{8.7}$ to $10^{8.8}$ and also the (a_{K^+}/a_{H^+}) ratio was estimated to range from $10^{2.2}$ to $10^{2.3}$ under the condition of coexistence of laumontite, illite and quartz (Fig. 4.15). K-feldspar is not able to coexist with laumontite under the above condition. K-feldspar occurs less abundantly and may be formed under a condition that is temporally or locally different from the above condition. Calcite also occurs with quartz, illite, K-feldspar and laumontite assemblage in Stage Q4.

f_{CO2} was estimated on the basis of the mineral assemblage and the following reaction:

$$CaCO_3 + 2H^+ = Ca^{2+} + CO_2(g) + H_2O.$$

Based on the equilibrium constants and the range from $(a_{Ca^{2+}}/(a_{H^+})^2)$ $10^{8.7}$ to $10^{8.8}$, f_{CO2} was estimated to range from 0.6 to 0.8 bars at 200°C.

Table 11 Equilibrium constants for estimation of formation environment of the Au-bearing quartz veins at the Q prospect.

Eq.	Reaction	log K 150°C	200°C	250°C
1.	$2KAl_2(AlSi_3)O_{10}(OH)_2 + 3H_2O + 2H^+ \rightleftharpoons 3Al_2Si_2O_5(OH)_4 + 2K^+$	4.85	4.27	3.76
2.	$3KAlSi_3O_8 + 2H^+ \rightleftharpoons KAl_3Si_3O_{10}(OH)_2 + 2K^+ + 6SiO_2$	8.31	7.99	7.70
3.	$CaAl_2Si_4O_{12}{\cdot}4H_2O + 2H^+ \rightleftharpoons Al_2Si_2O_5(OH)_4 + Ca^{2+} + 2SiO_2 + 3H_2O$	9.86	8.64	7.65
4.	$Ca_2Al(AlSi_3O_{10})(OH)_2 + SiO_2 + 2H_2O + 2H^+ \rightleftharpoons CaAl_2Si_4O_{12}{\cdot}4H_2O + Ca^{2+}$	10.17	8.75	7.50
5.	$3CaAl_2Si_4O_{12}{\cdot}4H_2O + 2K^+ + 4H^+ \rightleftharpoons 2KAl_3Si_3O_{10}(OH)_2 + 3Ca^{2+} + 6SiO_2 + 12H_2O$	24.73	21.65	19.19
6.	$Ca_2Al(AlSi_3O_{10})(OH)_2 + 3SiO_2 + 2K^+ + 2H^+ \rightleftharpoons 2KAlSi_3O_8 + 2Ca^{2+} + 2H_2O$	12.87	10.64	8.77
7.	$3Ca_2Al(AlSi_3O_{10})(OH)_2 + 2K^+ + 10H^+ \rightleftharpoons 2KAl_2(AlSi_3)O_{10}(OH)_2 + 6Ca^{2+} + 3SiO_2 + 6H_2O$	55.22	47.89	41.70
8.	$CaCO_3 + 2H^+ \rightleftharpoons Ca^{2+} + CO_2(g) + H_2O$	8.87	8.63	8.39

The values of log K for reaction were calculated using the SUPCRT92 database (Johnson et al., 1992)

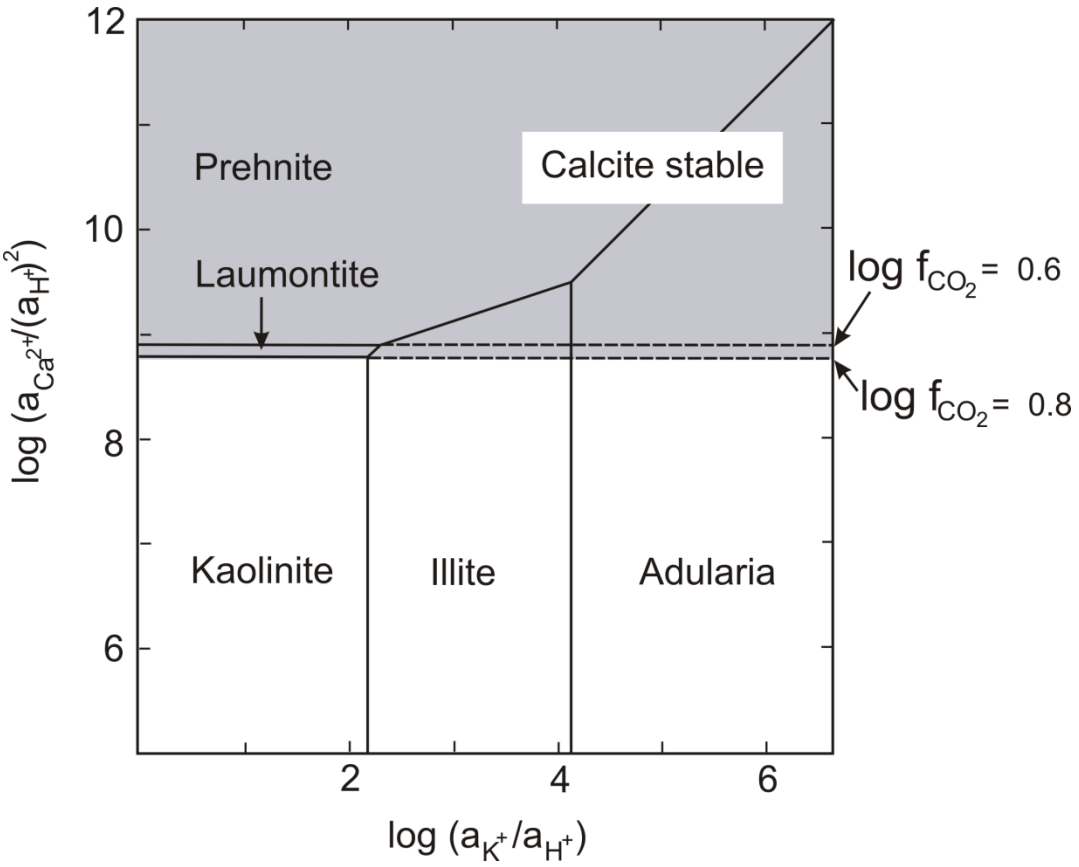

Figure 4.15 Activity diagram showing the stability of calcium and potassium aluminosilicates at temperature 200^{0}C in equilibrium with quartz and calcite. Calcite is stable in the gray-shaded area.

4.5.4 Possibility of boiling at the Q prospect

The presence of microcrystalline quartz and flamboyant texture of quartz in Stages Q1 and Q4 suggests that the hydrothermal solution was supersaturated with respect to amorphous silica. The flamboyant textures (Dong et al., 1995) and increase in the $\delta^{18}O$ values of quartz in Stage Q4 suggest a possibility of boiling.

The $\delta^{18}O$ values of quartz at the Stage Q4 increased by about 5 ‰ from +10.4 ‰ to +15.0 ‰. The temperature during the formation of quartz in Stage Q4 was estimated to be approximately 200°C based on the mineral assemblage. The temperature of the hydrothermal solution prior to boiling is thought to be higher than 200°C. Given that the temperature of the hydrothermal solution was 250°C, the increase in the $\delta^{18}O$ value of quartz during Stage Q4 can be explained by increase in the degree of isotopic fractionation between quartz and hydrothermal solution as well as increase in the $\delta^{18}O$ value of hydrothermal solution due to boiling. The increase in the $\delta^{18}O$ value of the hydrothermal solution is obtained from heat balance equations before and after boiling as follows:

$$H_{l,\,250°C} = yH_{v,\,200°C} + (1 - y)H_{l,\,200°C},$$

$$\delta^{18}O_{l,\,250°C} = y\delta^{18}O_{v,\,200°C} + (1- y)\,\delta^{18}O_{l,\,200°C},$$

$$\delta^{18}O_{l,\,200°C} = \delta^{18}O_{l,\,250°C} + y\,1000 \ln \alpha_{l\text{-}v},$$

where $H_{l,\,250°C}$, $H_{v,\,200°C}$, $H_{l,\,200°C}$, $\delta^{18}O_{l,\,250°C}$, $\delta^{18}O_{v,\,200°C}$ and $\delta^{18}O_{l,\,200°C}$ are the enthalpy of the original hydrothermal solution in a reservoir, the enthalpy of the vapor at 200°C after boiling, the enthalpy of the solution at 200°C after boiling, the $\delta^{18}O$ value of the original hydrothermal solution at 250°C, the $\delta^{18}O$ value of vapor at 200°C after boiling and the $\delta^{18}O$ value of the solution at 200°C after boiling, respectively, and y is the mass fraction of vapor. The enthalpy values reported by Keenan et al. (1969) and the fractionation factor between

liquid and vapor (1000 ln $\alpha_{l\text{-}v}$) reported by Truesdell (1977) were used for the calculation. Based on the calculation, the $\delta^{18}O$ value of the hydrothermal solution was increased by about 0.3 ‰ after boiling. The oxygen isotopic fractionation between quartz and water at 200°C is 2.8 ‰ (Matsuhisa et al., 1979), larger than that at 250°C. The sum of these two is 3.0 ‰ and the value (3.0‰) is similar to the increase in the $\delta^{18}O$ value of quartz during Stage Q4. Therefore, the increase in the $\delta^{18}O$ value from +9.9 to +15.0‰ of quartz during Stage Q4 suggests the occurrence of boiling and precipitation of electrum, illite, laumontite and calcite at approximately 200°C during Stage Q4.

4.5.5 Depth of formation of Au-bearing quartz veins at the Q prospect

Total pressure (P_T) during the formation of quartz veins was estimated on the basis of f_{CO2}, the calculation in the previous section and P_{H2O} at 200°C. P_{H2O} was estimated to be 16 bars from data of a steam table (Keenan et al., 1969). Therefore, total pressure of the hydrothermal solution is thought to be approximately 17 bars ($P_T = P_{H2O} + f_{CO2} = 16+1$). Given that a hydrostatic condition is assumed for the formation environment of gold mineralization at the Q prospect, the gold mineralization occurred 200 meters below the paleosurface, even when decrease in density of the hydrothermal solution and lowering of the ground water level are taken into account. The estimated depth is in the range of common epithermal gold deposits.

4.5.6 Origin of hydrothermal solution

The $\delta^{18}O$ values of the hydrothermal solution forming gold-bearing quartz veins at the Q prospect were estimated with an assumption of isotopic equilibrium between quartz and H_2O. The $\delta^{18}O$ ratios of gold-bearing quartz veins range from +10.4 to +11.7‰ from Stages Q1 to Q5 except for Stage Q4 (Table 2). Assuming that the temperature of the hydrothermal solution are 200°C or 250°C, the $\delta^{18}O$ ratios of the hydrothermal solution in equilibrium with quartz in Stages Q1 to Q5 (except for Stage Q4) range from -1.2 to +0.1‰ or +1.5 to +2.8‰, respectively.

The origin of water in hydrothermal solution having $\delta^{18}O$ values ranging from -1.2 to + 2.8‰ can be estimated using the procedure proposed by Taylor (1971). The final $\delta^{18}O$ values of water ($\delta^{18}O_f^w$) after oxygen isotopic exchange between water and rock was estimated to be

$$\delta^{18}O_f^w = \frac{W/R}{1+W/R}\,\delta^{18}O_i^w + \frac{1}{1+W/R}\,(\delta^{18}O_i^r - 1000 \ln \alpha_{r-w}),$$

in which i and f refer to the initial state (before water-rock interaction) and the final state (after water-rock interaction), respectively, and r and w refer to rock and water, respectively. The W/R ratio is the water/rock ratio expressed in mass proportion of oxygen. $1000 \ln\alpha_{r-w}$ was used as the fractionation factor between Anorthite and H_2O (Matsuhisa et al., 1979).

The final $\delta^{18}O$ ratio of water was estimated in the temperature range of 150° to 250°C assuming three cases of the initial water being magmatic water, meteoric water and seawater and assuming that the initial value of rock was + 6‰. In the case of magmatic water, the $\delta^{18}O$ values of final water suggest that quartz veins at the Q prospect were formed under a rock-dominant condition (Fig. 4.16a). However, such a rock-dominant condition is not suitable for the formation of gold deposits such as the Q prospect because the condition does

not allow supply of a large amount of hydrothermal solution for the formation of large epithermal gold deposits.

In the case of meteoric water, the $\delta^{18}O$ value of meteoric water was estimated to be -3‰. The geology of the Chatree area in Permian to Triassic age was formed under the subaerial environment near the seashore. The Chatree mining area was also located near the equator (from 10°N to 10°S) during the period of Au mineralization based on paleomagnetic data of the Shan-Thai plate (Bunopas and Vella, 1983; Grunow et al., 1996; Charusiri et al., 2002). The $\delta^{18}O$ values of meteoric water near the equator at present range from -6 to -1‰. The mode of the $\delta^{18}O$ values is -3‰ (Fricke and O'Neil, 1999). This value was used for calculation. The $\delta^{18}O$ values of final water also suggests that quartz veins at the Q prospect were formed under a rock-dominant condition at temperatures from 150° to 250°C (Fig. 4.16b).

On the other hand, if the initial water was seawater, the $\delta^{18}O$ values of final water of the hydrothermal solution suggest that the Au-bearing quartz veins at the Q prospect were formed under a water-dominant condition at temperatures from 150° to 250°C (Fig. 4.16c). Therefore, one of the possibilities for the initial water forming Au.-bearing quartz veins at the Q prospect is seawater. However, there is also a possibility that the hydrothermal solution was formed by mixing of meteoric water and magmatic water. Low salinity of secondary fluid inclusions in quartz of the Q prospect also supports the contribution of meteoric water to the hydrothermal system forming the Chatree deposit. Salinity of fluid inclusions in sphalerite of the Au-bearing quartz veins at the C pit of the Chatree deposit is 9.1 wt% of NaCl equivalent (Mori, 2009; Mizuta et al., 2009), which is higher than that of seawater. This high salinity may constrain the origin of hydrothermal solution forming gold-bearing quartz veins at the Q prospect.

The hydrothermal solution of the Chatree deposit has a possibility of a magmatic source based on the strontium isotope and fluid inclusions of sphalerite. However, the oxygen isotopic ratio of the Au-bearing quartz vein shows a possibility of meteoric water and/or seawater. Ohmoto and Rye (1970) proposed that the ore fluid of epithermal ore deposits have been originated from meteoric water in other locations.

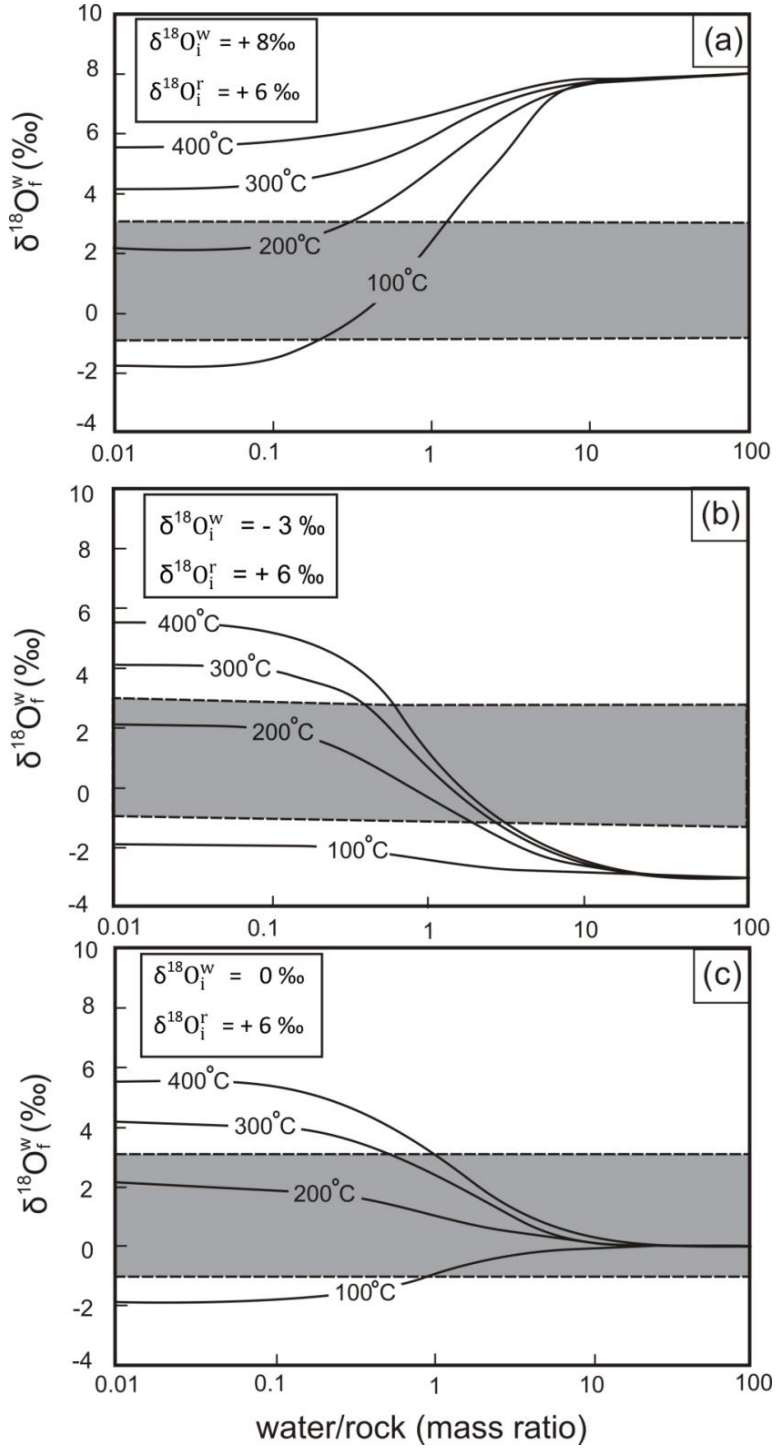

Figure 4.16 Calculation of the final $\delta^{18}O$ values of water based on different types of initial water and temperatures, with the $\delta^{18}O$ value of initial rock being +6 ‰. (a) The $\delta^{18}O$ value in the case of initial water being magmatic water. (b) The $\delta^{18}O$ value in the case of initial water being meteoric water. (c) The $\delta^{18}O$ value in the case of initial water being seawater.

Chapter 5: Cu-Mo mineralization

5.1 Mode of occurrence of Cu-Mo mineralization at the Chatree deposit

Cu-Mo mineralization is present at the N and V prospects in the southern part of the Chatree deposit (Fig. 3.1). Cu-Mo-bearing quartz veinlets occur in granodiorite porphyry and andesite lava (Unit 4) (Fig. 5.1). Granodiorite porphyry showing porphyritic texture is composed of coarse-grained plagioclase (0.5-3 mm), quartz and hornblende phenocrysts surrounded by fine-grained groundmass of quartz, plagioclase, ilmenite and magnetite. Alteration minerals of granodiorite porphyry are chlorite and sericite. Andesite lava is composed of plagioclase and hornblende phenocrysts (1-2 mm) and groundmass consisting of plagioclase, apatite and secondary minerals such as pyrite, chalcopyrite, chlorite and epidote.

Quartz veinlets are divided into five types from early to later stages such as types A, B, C, D and E (Fig. 5.1-5.3). Quartz veinlets of Types A, B and C occur in granodiorite porphyry and quartz veinlets of Types D and E occur in altered andesite lava (Fig. 5.3). The width of quartz veins range 0.5 to 5 mm. The mineral assemblage of the quartz veinlets of Types A, B and C consist of quartz-chlorite-illite-molybdenite-pyrite-chalcopyrite, quartz-chlorite-illite-chalcopyrite-pyrite and quartz-chlorite-illite-chalcopyrite-pyrite-sphalerite-pyrrhotite, respectively. The quartz veinlets of Types D and E are composed of quartz-chlorite-pyrite-chalcopyrite-sphalerite-pyrrhotite and quartz-epidote, respectively. Cu contents of Types A, B and C quartz veinlets are 0.15 wt%, while Cu content of Type D quartz veins is 0.07 wt%.

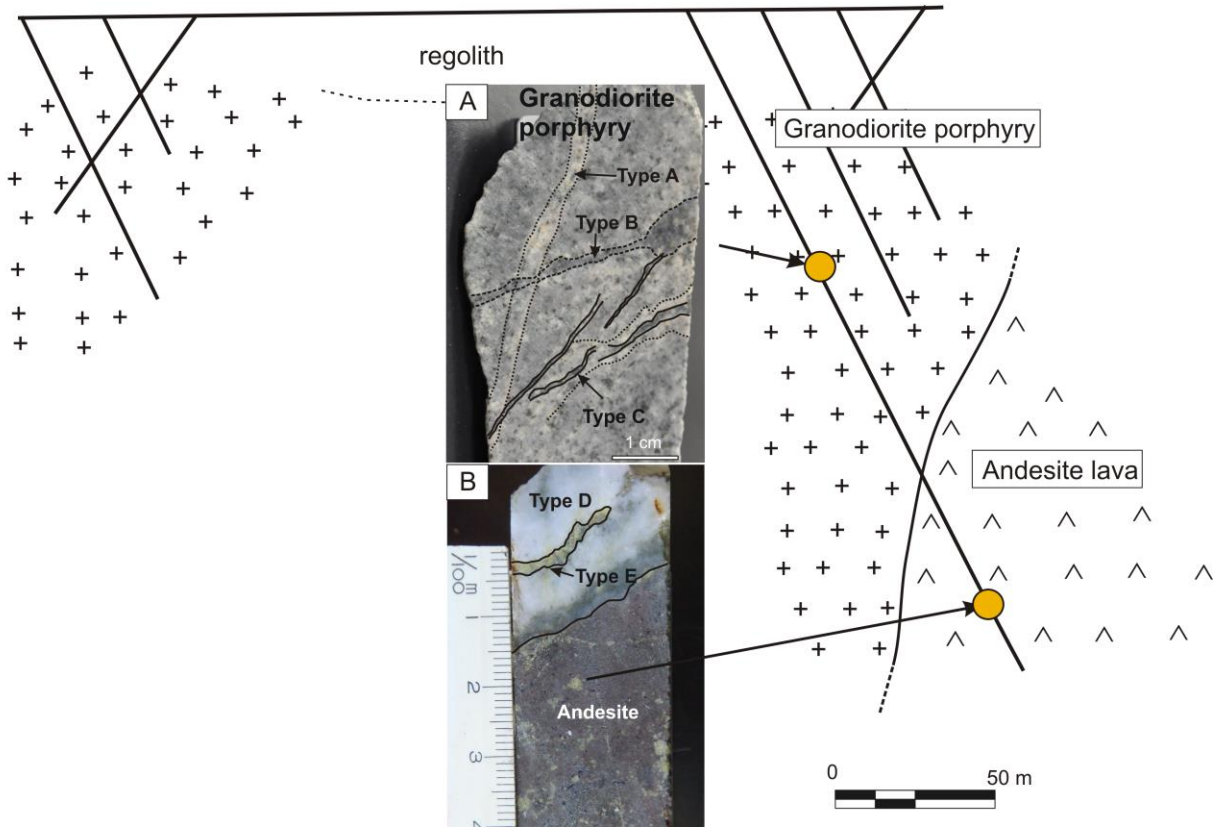

Figure 5.1 Cross-section of the N prospect shows granodiorite porphyry intruded andesite lava (unit 4). (A) Cross cutting relationship of Types A, B and C quartz veinlets in granodiorite porphyry. (B) Types D and E quartz veinlets in andesite lava.

Vein type	Host Rock	Minerals
A	Granodiorite porphyry	Qtz-Chl-Ilt-mol-py-ccp
B		Qtz-Chl-Ilt-ccp-py
C		Qtz-Chl-Ilt-ccp-py-sp-po
D	Andesite lava	Qtz-Chl-Ilt-py-ccp-sp-po
E		Qtz-ep

Figure 5.2 Quartz veinlets in Cu-Mo mineralization are classified into five types. Type A quartz veinlet contains molydenum. Quartz veins in granodiorite porphyry contain Cu higher than quartz veins in andesite lava.

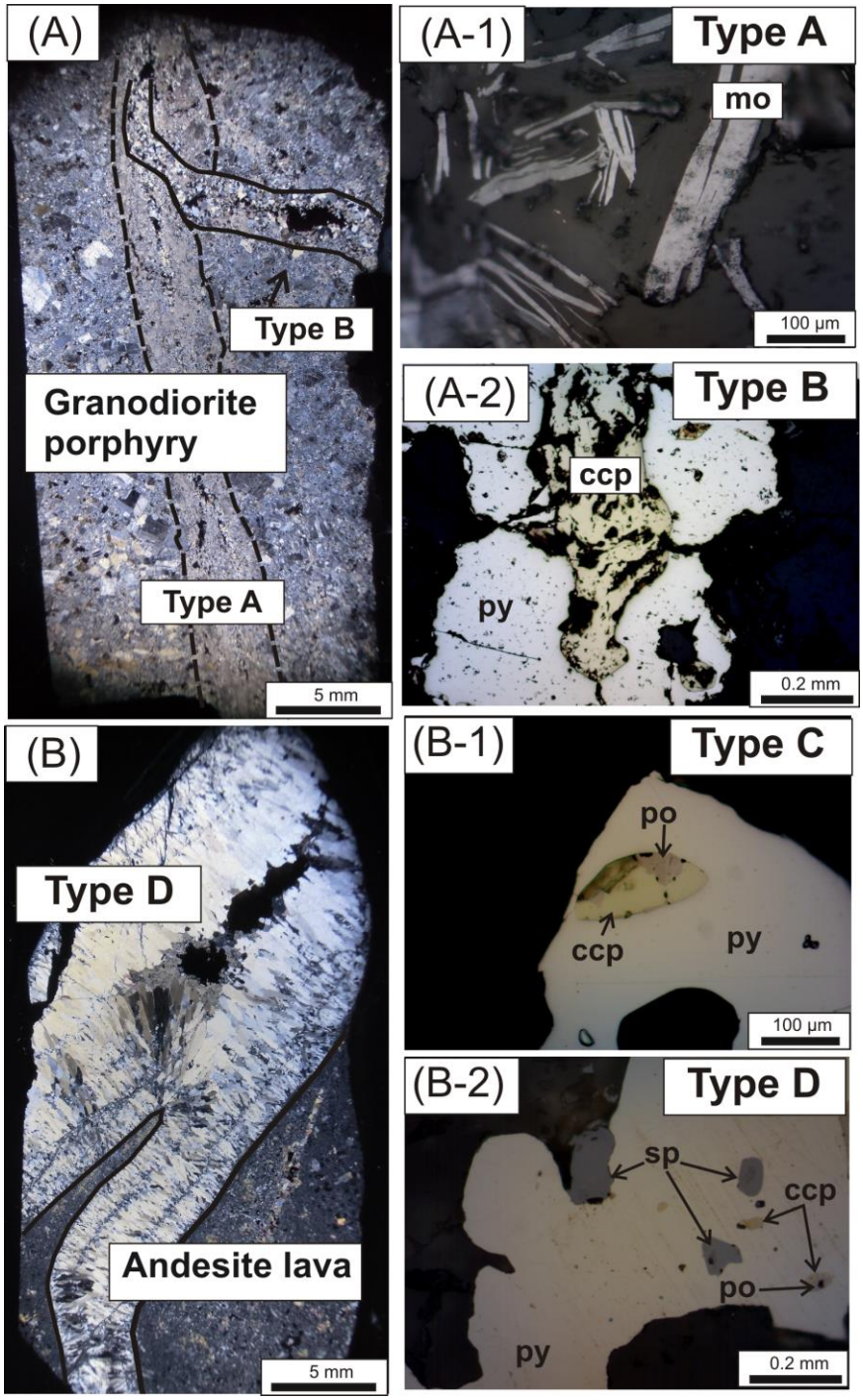

Figure 5.3 Photomicrographs showing mineral assemblage from Types A to D quartz veins. (A-1) Molybdenum is in Type A veinlet in granodiorite porphyry. (A-2) Pyrite coexists with chalcopyrite and pyrrhotite in Type B veinlets. (B-1) Type C quartz veinlet contains pyrite, chalcopyrite and pyrrhotite. (B-2) Type D vein containing pyrite, chalcopyrite, sphalerite and pyrrhotite.

Types C and D quartz veins are characterized by coexistence of pyrite, chalcopyrite and pyrrhotite. The phase relation of Cu-Fe-S system suggests that pyrite, chalcopyrite and pyrrhotite are formed in high temperature. Coexistence among pyrrhotite, pyrite and chalcopyrite suggest the temperature around 300° to 500°C.

5.2 Fluid inclusion study

Microthermometric measurements were performed on quartz veinlets using a Linkam heating-freezing stage (type-10002L) at Akita University. The temperature uncertainty in measurement of homogenization temperature (Th) and melting point of ice (Tm) is $\pm 0.2^{0}$C and $\pm 0.1^{0}$C, respectively..Fluid inclusions in the Cu-Mo-bearing quartz veins are composed of secondary fluid inclusions. The secondary fluid inclusions in the Cu-Mo-bearing quartz veins at the N and the V prospects (Fig. 5.4 and Table 3) are divided into three types according to the phase assemblage at room temperature by Roedder (1984): (1) liquid-rich two-phase fluid inclusions (volume of vapor less than 20% of the total volume), (2) vapor-rich two-phase fluid inclusions (volume of vapor more than 80% of the total volume) and (3) multiphase solid-bearing fluid inclusions. The multiphase solid-bearing fluid inclusions contain halite and reddish hematite in addition to liquid and vapor. Homogenization temperatures of liquid-rich fluid inclusions range from 100°C to 450°C with salinity ranging from 0.2 to 3.7 wt% NaCl eq. The homogenization temperatures of multiphase solid-bearing fluid inclusions range from 220°C to 450°C with salinities of 33.2 to 45.6 wt% NaCl eq (Fig. 5.5). The vapor-rich fluid inclusions was divided into two groups: (1) fluid inclusions having low salinity in the range from 0.1 to 1.0 wt% NaCl eq. and (2) fluid inclusions having slightly higher salinity in the range from 1.0 to 4.0 wt% NaCl eq.

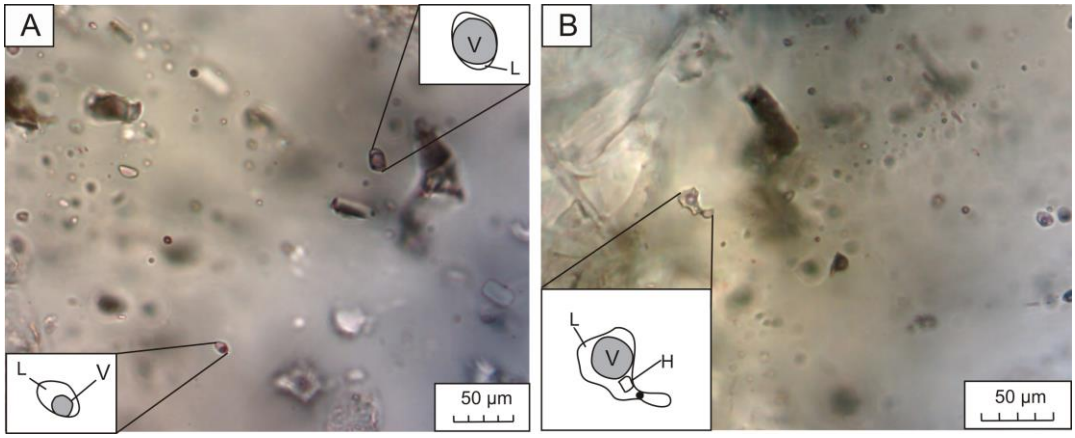

Figure 5.4 Photomicrographs of fluid inclusions in quartz veinlets from the N prospect. (A) Two phase fluid inclusions consist of liquid-rich fluid inclusions and vapor-rich fluid inclusions. (B) Multiphase solid-bearing fluid inclusions.

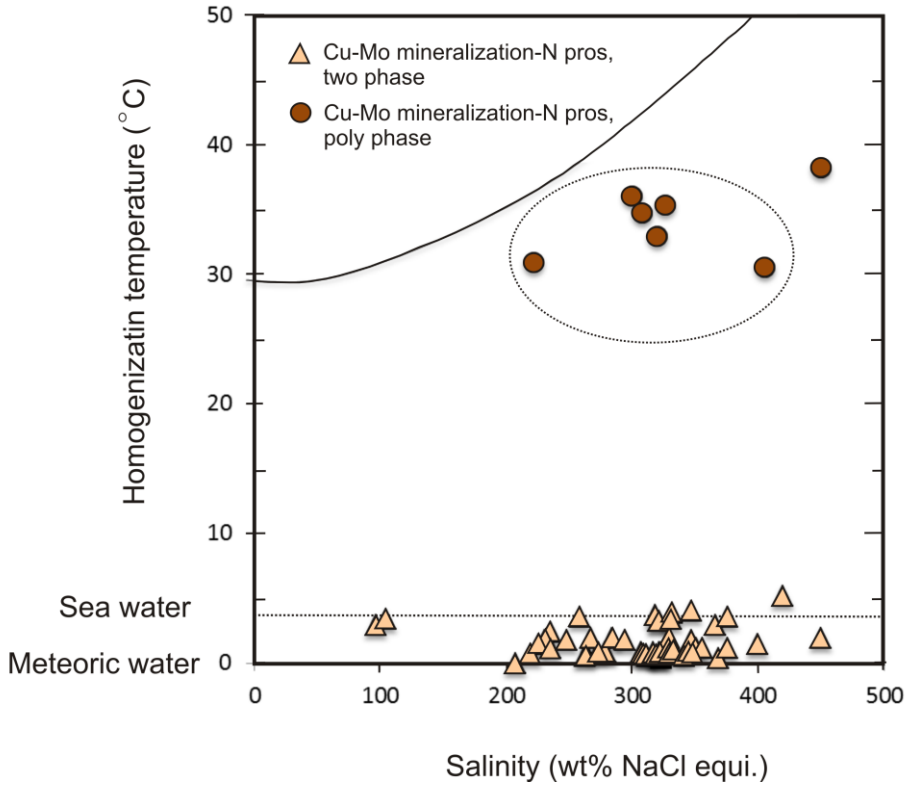

Figure 5.5 Diagram showing relationship between homogenization temperatures and salinities of fluid inclusions at the N prospect.

Table 12 Homogenization temperatures and salinities of fluid inclusions of quartz veinlets in granodiorite porphyry.

Sample no.	No	T_h (°C)	T_m(°C)	wt% NaCl eq.	Type
N-1	1	263	-1.0	0.5	V, S
	2	267	-1.9	1.9	L, S
	3	258	-3.0	3.6	V,S
	4	311	-1.1	0.6	L, S
	5	235	-1.4	1.1	V, S
	6	264	-1.1	0.6	L, S
	7	278	-1.2	0.8	L, S
	8	294	-1.8	1.7	V, S
	9	226	-1.6	1.4	V, S
	10	330	-1.5	1.3	V, S
	11	231	-1.8	1.7	V, S
	12	235	-2.2	2.3	L, S
	13	219	-1.1	0.6	L, S
	14	330	-1.4	1.1	V, S
	15	351	-1.4	1.1	L, S
	16	230	-1.9	1.9	V, S
	17	400	-1.6	1.4	L, S
	18	450	-1.9	1.9	V, S
	19	104	-2.9	3.4	V, S
	20	97	-2.6	2.9	V, S
N-1-1	21	376	-1.4	1.1	L, S
	22	321	-1.0	0.5	L, S
	23	321	-2.8	3.3	V, S
	24	332	-3.2	3.9	V, S
	25	248	-1.8	1.7	L, S
N-1-2	26	347	-3.3	4.0	V, S
	27	323	-0.9	0.3	L, S
	28	333	-1.2	0.8	L, S
N-1-4	29	322	-1.2	0.8	V, S
	30	341	-1.0	0.5	V, S
	31	331	-2.9	3.4	L, S
	32	319	-3.1	3.7	L, S
	33	366	-2.6	2.9	V, S
	34	207	-0.7	0.1	V, S
	35	312	-1.0	0.5	V, S
	36	307	-1.2	0.8	V, S
	37	317	-1.2	0.8	V, S
	38	284	-1.9	1.9	V, S
	39	279	-1.2	0.8	V, S
N-1-5	40	347	-1.8	1.8	L, S
	41	348	-1.2	0.8	L, S
	42	323	-1.0	0.5	L, S
	43	333	-1.3	0.9	L, S
	44	376	-3.0	3.6	V, S
	45	273	-1.2	0.8	L, S
N-1-6	46	369	-0.9	0.3	V, S
	47	322	-2.8	3.3	L, S
	48	356	-1.4	1.1	L, S
	49	319	-1.0	0.5	L, S
	50	309	-1.1	0.6	L, S
N-1-6	51	326	35.0	43.9	D, S
	52	308	34.7	42.4	D, S
	53	450	35.0	43.1	D, S
N-1	54	405	30.5	33.2	D, S
	55	222	30.9	34.0	D, S
	56	320	32.9	38.3	D, S
	57	300	36.0	45.6	D, S

L, liquid; V, vapor; D, multiphase solid-bearing; S, secondary fluid inclusion

5.3 Oxygen isotopic study

Oxygen isotopic ratios of samples of altered granodiorite porphyry and altered andesite lavas from the N and V prospects were analyzed. The $\delta^{18}O$ ratios of altered granodiorite porphyry and altered andesite lavas range from +9.4 to +10.7‰. The $\delta^{18}O$ values (+10.7‰) of altered granodiorite porphyry are heavier than those of altered andesite lava (+9.4‰). The $\delta^{18}O$ value of Type D quartz vein in andesite lava is +13.0 ‰.

The oxygen isotopic exchange reaction between fluids and rocks in the Cu-Mo mineralization may be considered as a simple water-rock interaction. The change in the $\delta^{18}O$ value of rock due to water-rock interaction can be evaluated from Sheppard et al. (1969) and Taylor (1971). The final $\delta^{18}O$ value of rock after the oxygen isotopic exchange between water and rock was estimated by,

$$\delta^{18}O_f^r = \frac{\delta 18O_i^r + (\delta 18O_i^w + 1000 \ln \alpha_{r-w})W/R}{1+W/R},$$

$1000 \ln \alpha_{r-w}$ is the fractionation factor between Albite and H_2O (Matsuhisa et al., 1979).

The final $\delta^{18}O$ of rock of strongly altered granodiorite porphyry was estimated at the temperature of 450°C under a water-dominant condition assuming cases of the initial water being magmatic water (Fig. 5.7). In the case of meteoric water and sea water, the final $\delta^{18}O$ ratios of rocks suggest that quartz were formed under a rock-dominant condition at the temperature below 100°C. Therefore, magmatic water is a possible source of the initial water that formed the Cu-Mo mineralization at the N and V prospects.

Table 13 The $\delta^{18}O$ values of altered granodiorite porphyry, altered andesite lava and Type D quartz vein.

Sample no.	Rock type	$\delta^{18}O$ (‰)
N-1	Granodiorite porphyry	9.7
N-5	Granodiorite porphyry	9.4
NP-7	Andesite lava	10.7
NP-14	Andesite lava	10.0
NP-14Q	Type D quartz vein	13.0

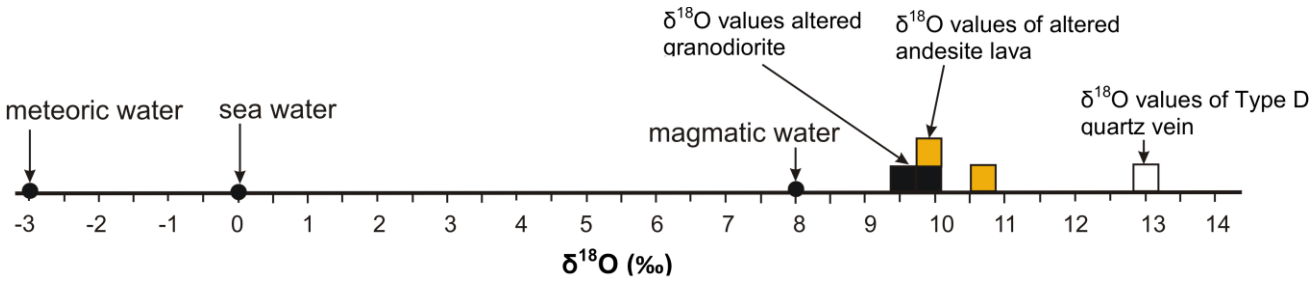

Figure 5.6 Histogram showing the $\delta^{18}O$ values of altered granodiorite porphyry, altered andesite lava and Type D quartz vein. The $\delta^{18}O$ values of meteoric water, sea water and magmatic water were -3.0 ‰, 0.0‰ and 8.0‰, respectively.

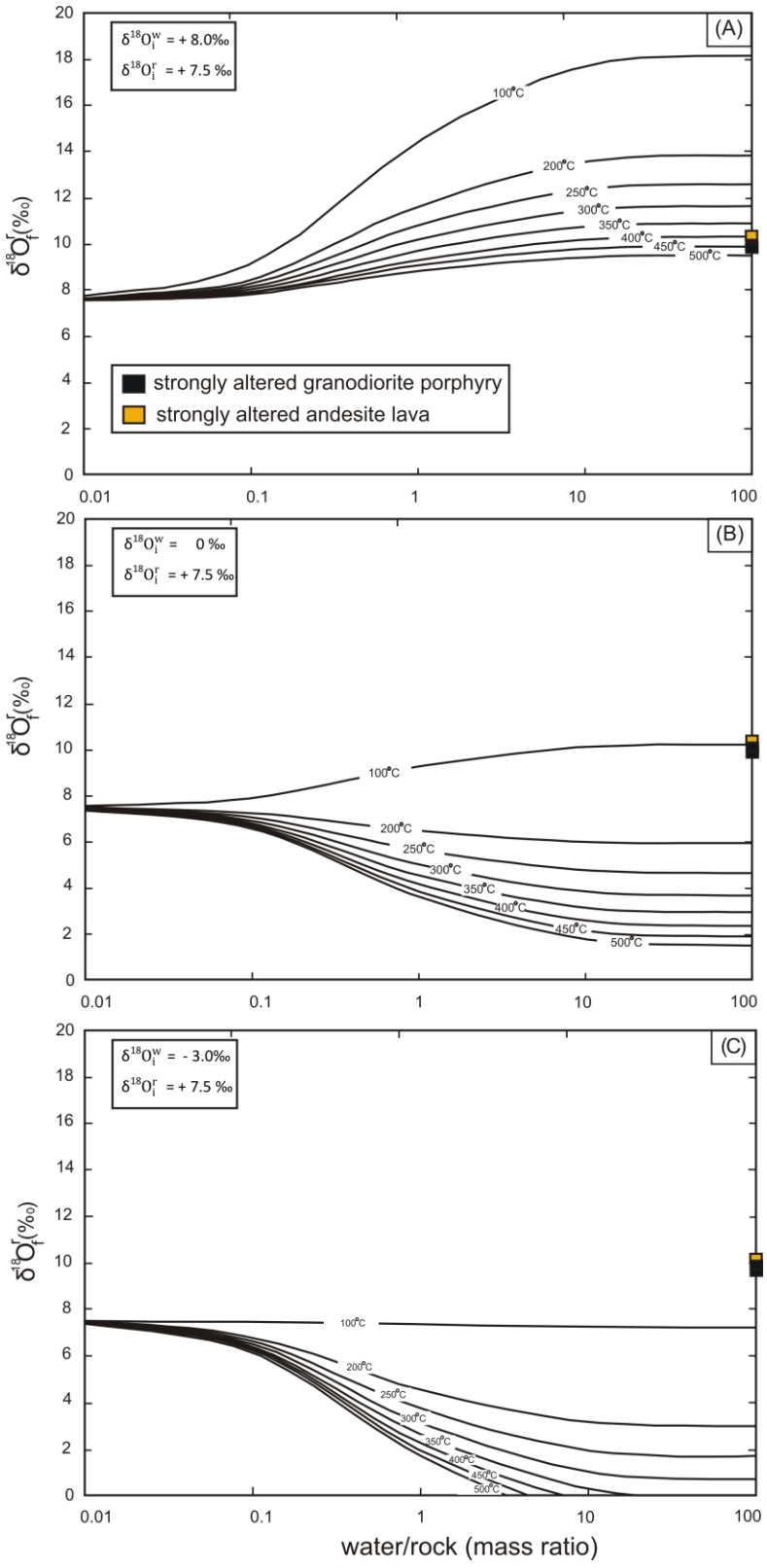

Figure 5.7 Calculation of the final $\delta^{18}O$ value of rock based on different types of initial water and temperatures, with the $\delta^{18}O$ of initial rock being +7.5 ‰. (a) The $\delta^{18}O$ in the case of initial water being magmatic water. (b) The $\delta^{18}O$ in the case of initial water being sea water. (c) The $\delta^{18}O$ in the case of initial water being meteoric water.

5.4 Formation environment of Cu-Mo mineralization

Fluid inclusions of quartz veins at the N prospect are divided into liquid-rich two-phase fluid inclusions and multiphase solid-bearing fluid inclusions. Most of halite-bearing fluid inclusions show lower dissolution temperature of halite crystals and then the homogenization temperature of vapor bubble to liquid. The process suggests that fluid forming the halite-bearing fluid inclusions was formed as a result of phase separation under low pressure and high temperature condition. Henley and McNabb (1978) proposed that hypersaline liquid coexist with vapor in porphyry Cu fluid inclusions originated as a homogeneous, moderate-salinity, relatively low density plume of magmatic fluid that separated to hypersaline liquid and low-salinity vapor during ascent and depressurization. The fluid inclusions of the Cu-Mo mineralization were observed with coexisting halite-bearing fluid inclusion and vapor-rich fluid inclusion (Fig. 5.8). It can be explained in terms of unmixing of an originally homogeneous aqueous fluid, exsolved from the magma with salinities typically in the range of 2 to 10 wt% NaCl equivalent and at pressures of 1.0 to 1.5 kbar, equivalent to depths of 4 to 6 km at lithostatic pressure (Burnham, 1979; Hedenquist et al., 1998). During ascent from its point of exsolution from the parent magmatic pluton to the depth of ore formation, the magmatic fluid intersects its solvus, forming immiscible liquid and vapor phases of hugely contrasting density.

Halite-bearing fluid inclusions and vapor-rich fluid inclusions from the Cu-Mo mineralization, can coexist when a high-temperature magmatic fluid ascended and intersected its solvus. The halite-bearing fluid inclusion having 37 wt% NaCl equivalent coexists with vapor-rich fluid inclusion having 1 wt% NaCl equivalent, at the temperature of 450°C and pressure 250 bar, which is equivalent to depth of 1 km at lithostatic pressure (Fig. 5.8).

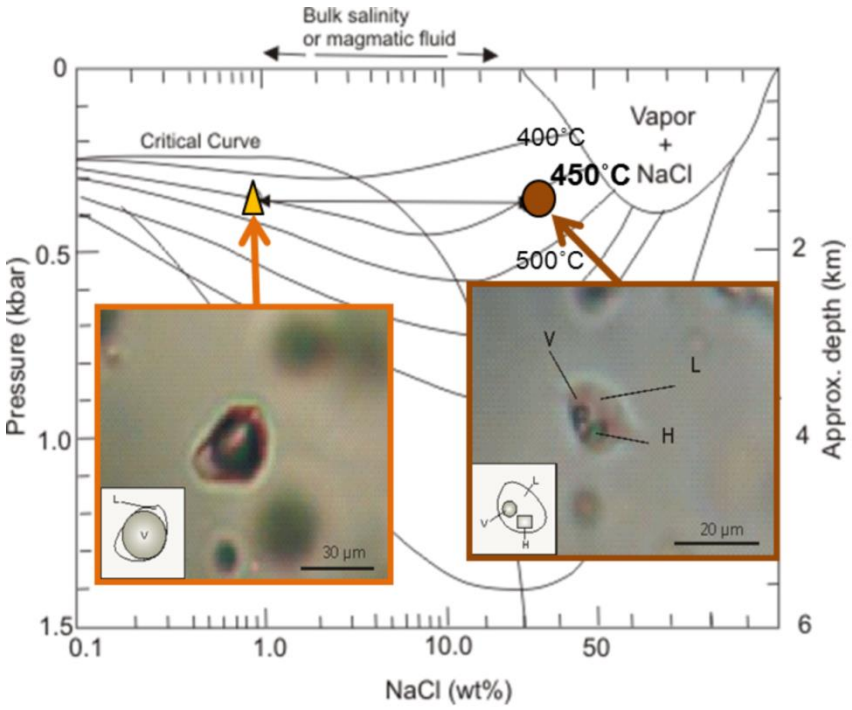

Figure 5.8 Diagram of the H_2O-NaCl system (Sourirajan and Kennedy, 1962) with halite-bearing fluid inclusion and vapor-rich fluid inclusion of Cu-Mo mineralization at the N prospect. The magmatic fluid separated to vapor-rich fluid inclusions (1 wt% NaCl equivalent) and a halite-bearing fluid inclusion (37 wt% NaCl equivalent) during ascent and depressurization. Cu-Mo mineralization occur at temperature of 450°C and depth of 1 km.

Cu-Mo mineralization in the Chatree deposit was formed at the temperature of 450°C and depth of about 1 km below the paleosurface.

Chapter 6: Strontium isotopic study

The geology around the Chatree deposit is composed mainly of sedimentary strata from Carboniferous to Permian as described in detail in Chapter 3. Carboniferous strata consist of conglomerate, sandstone, shale, chert and limestone. Early Permian strata consist of limestone. The limestones contain warm water Tethyan macro fauna (Fontaine et al., 1991). Middle Permian strata are dominantly sandstone and shale. Late Permian volcanic sequences are the host rocks of the Chatree deposit. Intrusions around the Chatree deposit are Carboniferous granite and Early Triassic diorite (Fig. 6.1). Permian volcanic rocks are considered to be formed in a volcanic arc environment related to subduction of oceanic crust beneath the Indochina terrane around 258 Ma (Salam et al., 2013).

6.1 Samples for strontium isotopic study

For strontium isotopic analyses, the samples of Carboniferous-Permian limestone, siltstone, sandstone, andesite lava, strongly altered andesite lava, post-mineralization andesite dike, diorite, granodiorite porphyry, the Au-bearing quartz veins and calcite veins were collected to understand temporal and spatial evolution of hydrothermal system of the Chatree deposit. Those samples were collected within the Chatree mining area and at location away from the Chatree mining area (Fig. 6.1). The samples in the Chatree mining area were collected from the A and C pits and Q, N, V prospects. From the A pit, the sample of strongly altered andesite lava, weakly altered andesite lava, post-mineralization andesite dike, Au-bearing quartz veins of Stage A1, network-type vein of Stage A4 and calcite vein of Stage A5 were collected as shown in Fig. 6.2. The sample of weakly altered andesite lava was collected approximately 4 meter far from the network veins (Fig. 6.2C). The strongly altered andesite

lava was collected near quartz veins (2 cm away from the vein) (Fig. 6.2). The post-mineralization andesite dike cut andesite lava and quartz veins (Figs. 6.2A and 6.3B). The Au-bearing network-type veins and calcite veins were collected from the A pit (Fig. 6.2B). From the Q prospect, the sample of strongly altered andesite lava, weakly altered andesite lava, post-mineralization andesite dike, Au-bearing network-type veins of Stage Q4 and calcite vein of Stage Q5 were collected as shown in Fig. 6.3. Samples of andesite lava and granodiorite porphyry at the N and V prospects were also collected to understand characteristics of magmatic-hydrothermal system forming Cu-Mo mineralization in granodiorite porphyry. At location away from the Chatree mining area as shown in Fig. 6.1, diorite, Carboniferous-Permian limestone and Carboniferous siltstone and shale were collected. Sample of diorite was collected away from the Chatee deposit as shown in Fig. 6.1. Samples of Carboniferous-Permian limestone were collected away from the Chatree mining area. Limestone samples were collected from southeast and east of the Chatree deposit as shown in Fig. 6.1. Carboniferous siltstone and shale was collected in east of the Chatree mining area. Photographs of hand specimen of these samples and the following samples from location away the Chatree mining area are show in Fig. 6.4.

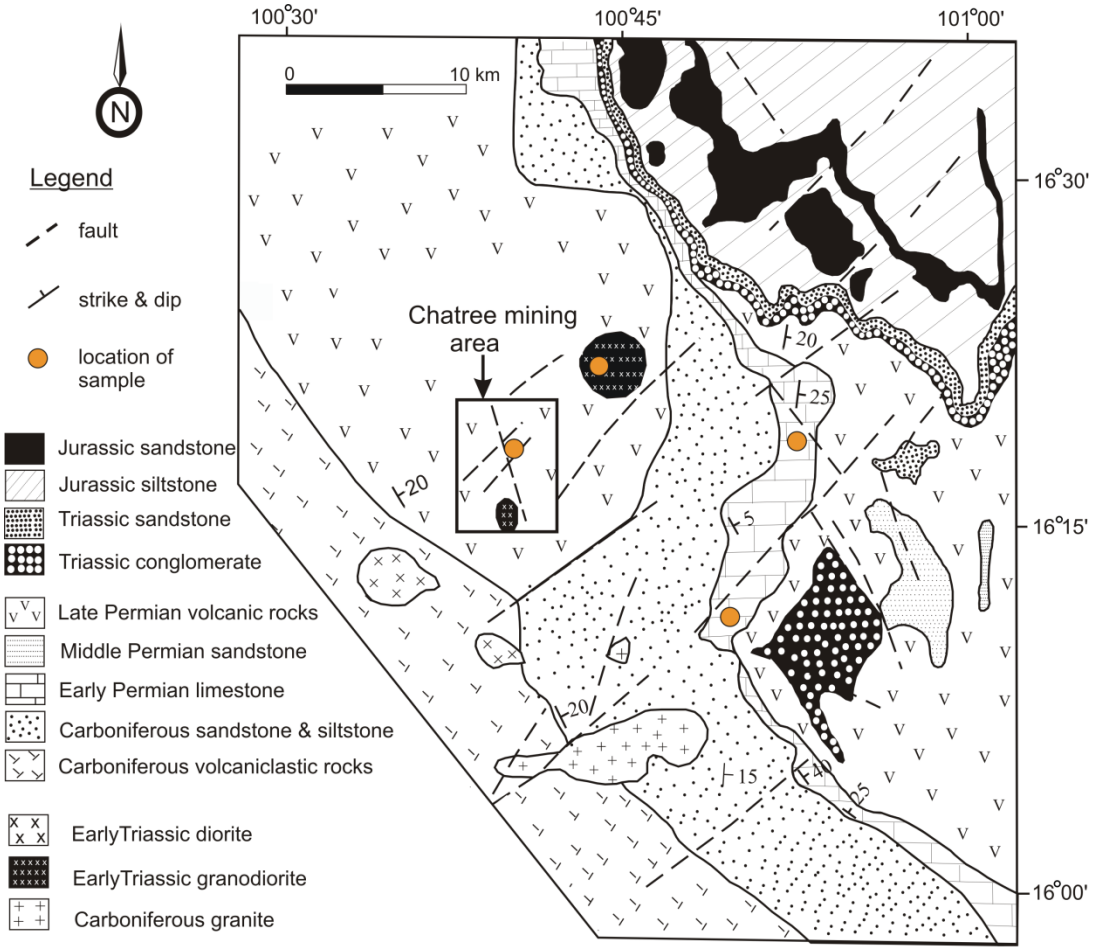

Figure 6.1 The location of samples for strontium isotopic analysis are shown in the regional geologic map around the Chatree mining area. The samples from the Chatree mining area were collected in the area shown by the square (See Chapter 3). Away from the Chatree mining area, samples of Carboniferous sandstone and siltstone, Permian limestone and Triassic diorite were collected at the localities shown as orange circles.

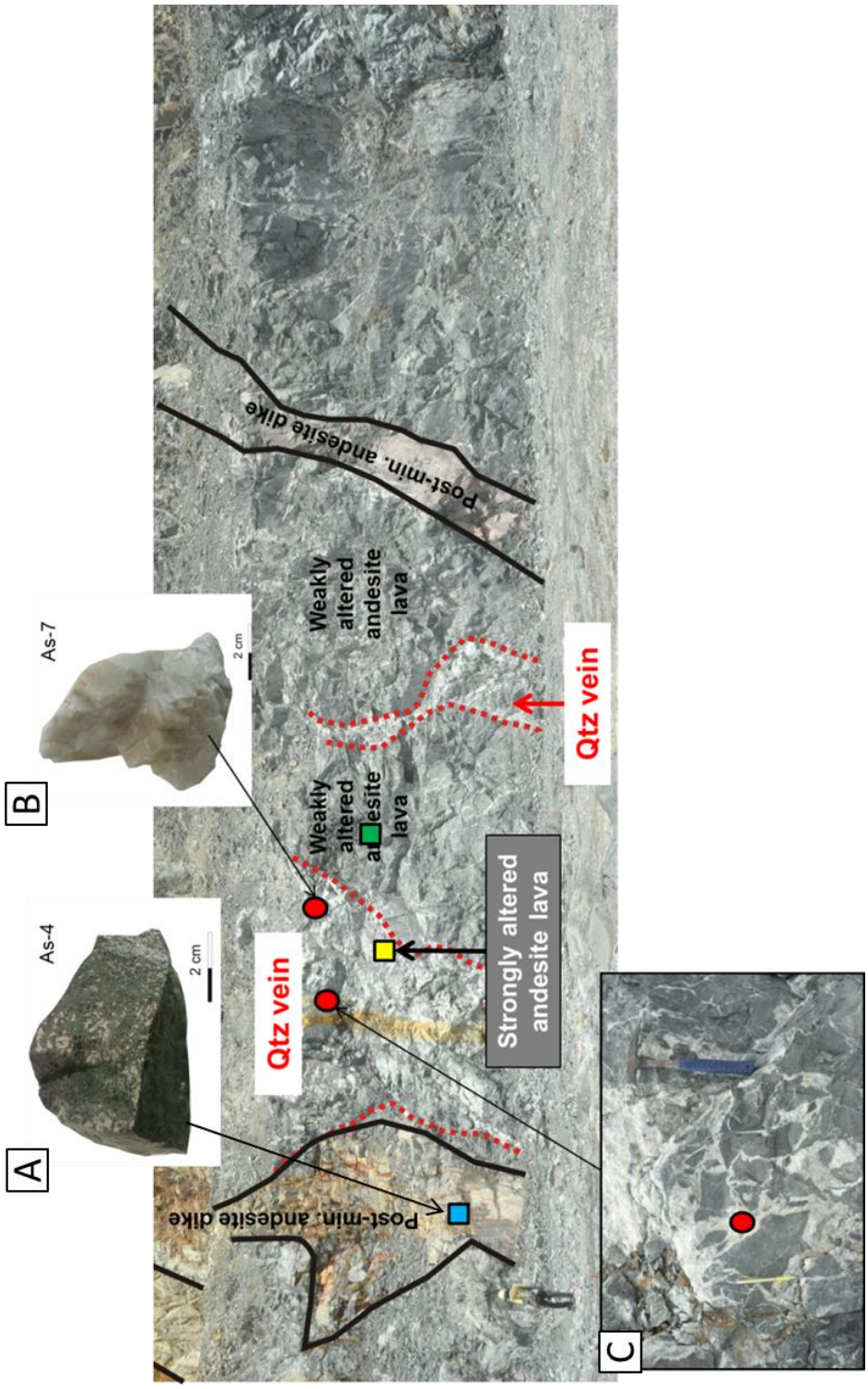

Figure 6.2 Photograph of open pit wall showing occurrence of the weakly altered andesite lava, the strongly altered andesite lava, the Au-bearing quartz veins and the post-mineralization andesite dikes at the A pit. The andesite lava (Unit 4) is cut by the Au-bearing quartz veins and post-mineralization andesite dike. (A) Post-mineralization andesite dike cut quartz veins and andesite lava. (B) Calcite vein of Stage A5 is collected. (C) Photograph is the Au-bearing quartz veins of Stage A4.

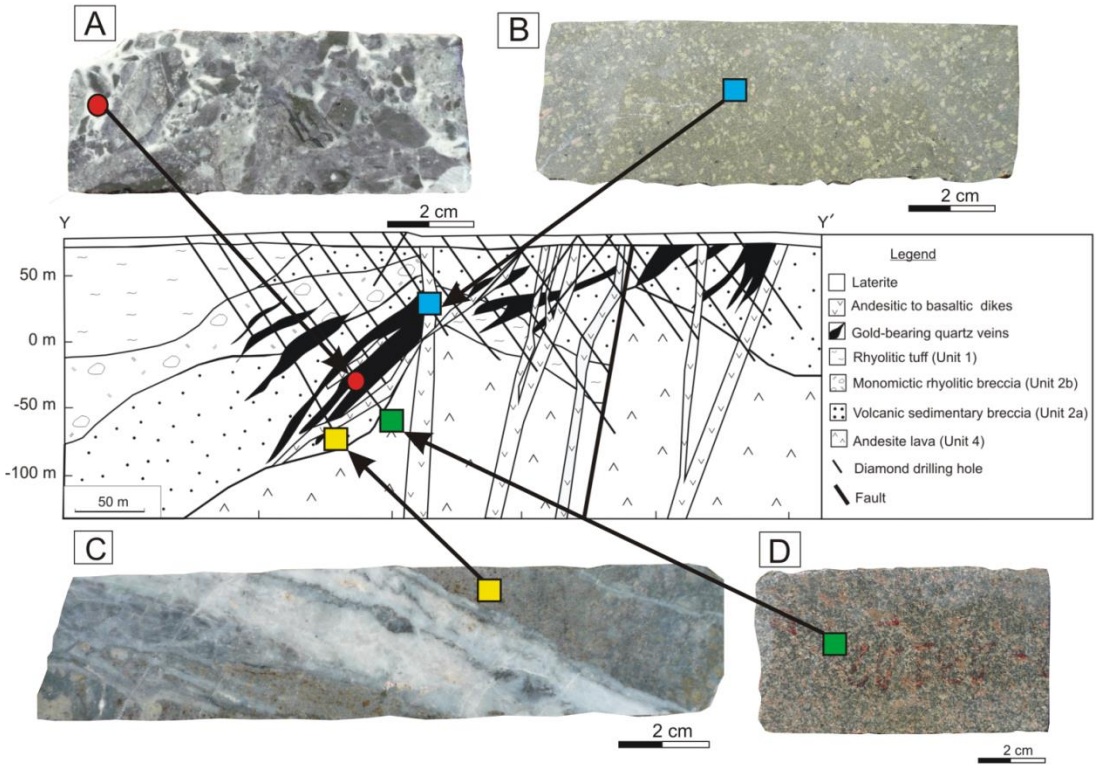

Figure 6.3 Cross section of the Q prospect showing the location of the weakly altered andesite lava, the strongly altered andesite lava, the Au-bearing quartz veins of Stage Q4 and the post-mineralization andesite dike. (A) The Au-bearing quartz vein of Stage Q4 is collected at the Q prospect. (B) The post-mineralization andesite dike cut andesite lava and quartz veins. (C) The strongly altered andesite lava cut by the Au-bearing quartz veins of Stage Q4. (D) The andesite lava of Unit 4 is weakly alterated.

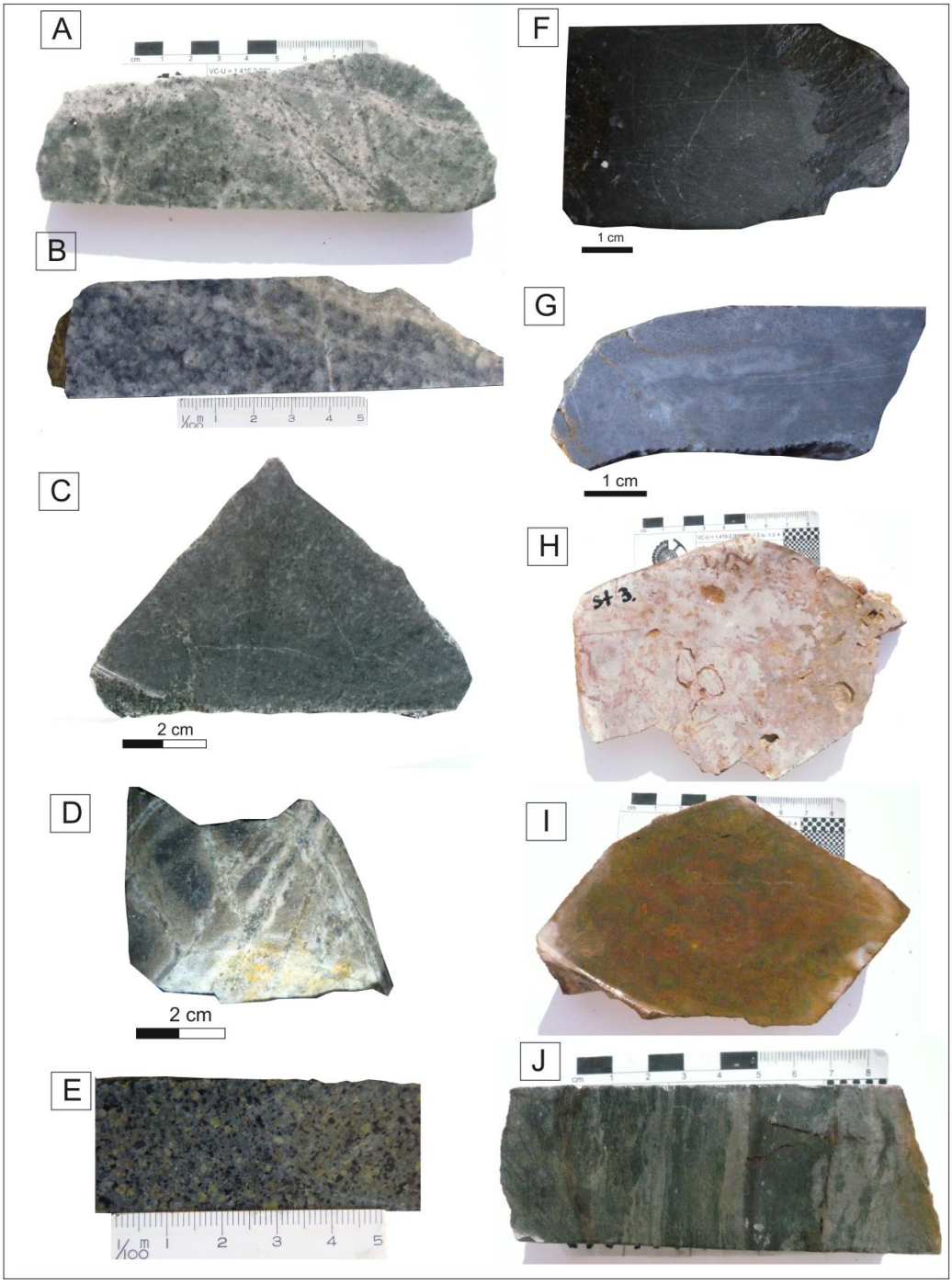

Figure 6.4 Photographs of hand specimen samples from the N and V prospects and location away from the Chatree mining area. (A-B) Granodiorite porphyry from the N prospect. (C) Least altered diorite away from the Chatree mining area. (D-E) andesite lavas from the N and V prospects. (F) Carboniferous-Permian limestone in the southeast of the Chatree mining area. (G) Carboniferous-Permian limestone to the east of the Chatree mining area. (H-I) Carboniferous siltstone to the east of the Chatree mining area and contains of brachiopods. (J) Carboniferous shale is characterized by gray color of lamination.

6.2 Characteristics of alteration of samples for study of strontium isotopic ratios

The area of least altered volcanic rocks is shown in the diagram of alteration index and CCP index (Fig. 6.5). The weakly altered andesite lava and post-mineralization andesite dike are plotted in the field of mafic rocks of the least altered box (andesite and basalt), while strongly altered andesite lava near veins are plotted in area of strongly altered rock of VMS deposit (Alteration Index ranging from 80 to 98) (Fig. 6.5). Samples of andesite lava from the N and V prospects are plotted in the box of least altered rocks. Granodiorite porphyry is characterized by silicified alteration as shown in Chapter 5. Diorite consists of plagioclase, amphibole, biotite, quartz, magnetite and ilmenite. The alteration index and CCP index of diorite 35 and 88, respectively.

Table 14 Strontium isotopic ratios, Rb, Sr and Au contents of rocks and veins from the Chatree mining area .

Location	Sample no	Descriptions	Rb (ppm)	Sr (ppm)	Au (ppm)	$^{87}Rb/^{86}Sr$	Age Ma	$(^{87}Sr/^{86}Sr)m$	$(^{87}Sr/^{86}Sr)i$	2σ error
Au mineralization										
Andesite lava										
Q prospect	and-Q	weakly altered andesite lava	21.9	530		0.121	258±3	0.705563	0.705118	0.000009
Q prospect	Qgs-3	strongly altered andesite lava	58.4	36.0		4.954	250±1	0.725220	0.707632	0.000012
A pit	A15	strongly altered andesite lava	107	79.0		4.133	250±1	0.723909	0.709235	0.000005
Veins										
Q prospect	Hbx-3IV	qtz-cc-ad brecciated veins of Stage Q4	20.0	63.7	1.45	0.958	250±1	0.711655	0.708254	0.000020
Q prospect	Qc-4V	cc vein of Stage Q5	0.4	102.1	0.10	0.012	250±1	0.705190	0.705146	0.000005
A pit	A7	qtz-cc-ad vein of Stage A1	0.6	73.1	1.19	0.023	250±1	0.706247	0.706164	0.000018
A pit	A15I	qtz-cc-ad brecciated veins of Stage A1	0.5	12.4	3.20	0.116	250±1	0.708704	0.708293	0.000006
A pit	A14Lg	qtz-cc-ad vein of Stage A1	2.2	38.2	4.50	0.182	250±1	0.707597	0.706949	0.000010
A pit	A16IV	qtz-cc-ad brecciated veins of Stage A4	13.1	43.5	0.69	0.924	250±1	0.720887	0.717607	0.000023
A pit	As-7	cc vein of Stage A5	2.0	30.0	0.01	0.203	250±1	0.705566	0.704843	0.000006
C pit	V1	cc-chl-qtz vein	2.0	30.0	1.15	0.203	250±1	0.705290	0.704567	0.000011
C pit	V2	cc-chl-qtz vein	2.0	30.0	0.01	0.203	250±1	0.706015	0.705292	0.000020
Post-mineralization andesite dike										
A pit	As4	least altered post-mineralization andesite dike	21.0	371		0.173	244±5	0.705566	0.704967	0.000010
Q prospect	gan-3	least altered post-mineralization andesite dike	94.1	510		0.562	244±5	0.705676	0.703727	0.000006
Cu-Mo mineralization										
Andesite lava										
N prospect	NP-7	least altered andesite lava	41.3	439		0.287	258±3	0.706362	0.705309	0.000008
V prospect	NP-13	least altered andesite lava	12.6	371		0.104	258±3	0.705595	0.705212	0.000006
Granodiorite										
N prospect	N-1	strongly altered granodiorite porphyry	6.7	650		0.032	244±5	0.704329	0.704219	0.000017
N prospect	N-5	strongly altered granodiorite porphyry	4.1	730		0.017	244±5	0.704273	0.704213	0.000015
Rocks a way from the Chatree deposit										
Diorite	D-1	least altered diorite	9.9	700		0.043	244±5	0.704337	0.704187	0.000008
Limestone	St7	Carboniferous-Permian						0.706517		0.000011
Limestone	St1	Carboniferous-Permian						0.707484		0.000016
Sedimentary rock	St3-1	Carboniferous	0.4	90.0		0.137	250±1	0.706798	0.706313*	0.000008
Sedimentary rock	St3-2	Carboniferous	2.3	127		0.055	250±1	0.706498	0.706302*	0.000012
Sedimentary rock	St3-3	Carboniferous	1.5	56.6		0.081	250±1	0.706231	0.705942*	0.000013

$^{87}Sr/^{86}Sr_m$, measured $^{87}Sr/^{86}Sr$; $^{87}Sr/^{86}Sr_i$, initial $^{87}Sr/^{86}Sr$; blank of Au content column, below detection limit

*, initial $^{87}Sr/^{86}Sr$ ratio of sedimentary rock is calculated at the same age as the Au-bearing hydrothermal solution

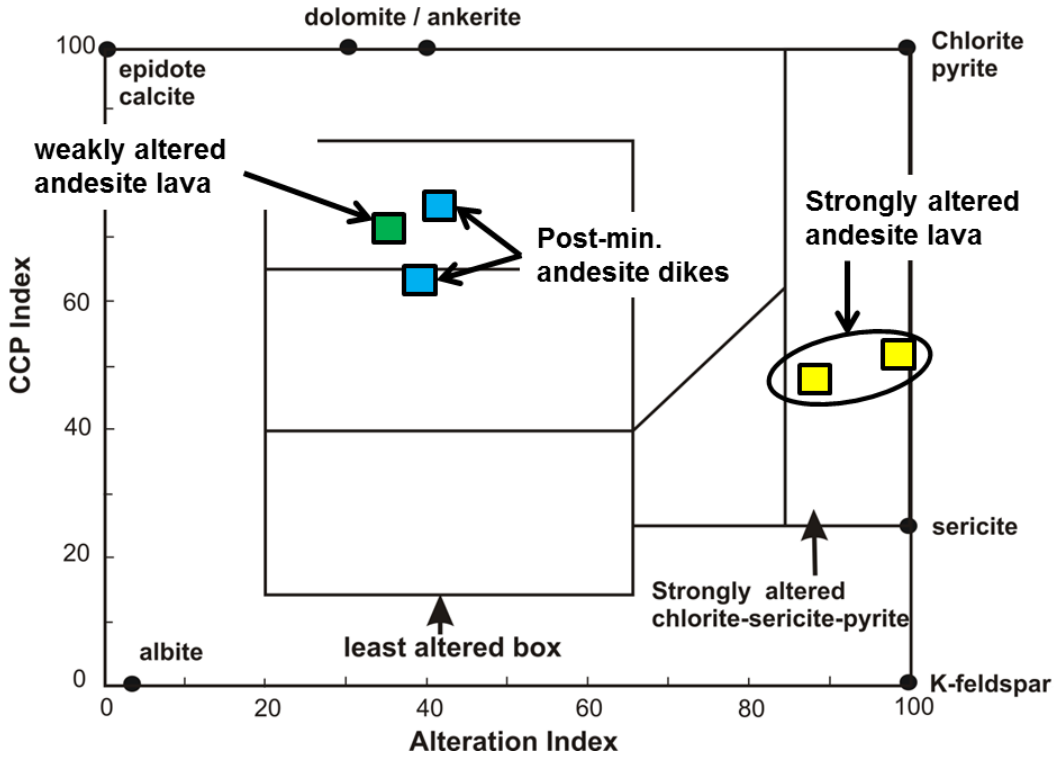

Figure 6.5 Classification of altered rocks of the Chatree deposit based on alteration and CCP indexes (Ishikawa et al., 1976; Large et al., 2001). The weakly altered andesite lavas, strongly altered andesite lavas and post-mineralization andesite dikes at the A pit and Q prospect were plotted in the least altered box. The strongly altered andesite lavas were plotted in the area of strongly altered chlorite-sericite-pyrite alteration of VMS deposits.

6.3 Analytical procedure of strontium isotopic ratios

The rock and vein samples were crushed to pieces of 1-2 mm in size and washed ultrasonically in ultrapure water about 10 minutes, followed by multiple rinses with the water before being ground in mortar. 100 mg of each powder sample was completely digested in a concentrated HF-$HClO_4$-HNO_3 solution in a closed Teflon bottle on hot plate in accordance with the procedure described by Satoh et al. (1999). The solution sample was analyzed by ICP-MS at Akita University to determine concentration of Sr. The sample solutions of amount desired to obtain 10 μg of Sr were evaporated and then 1 ml of 3.5 N HNO_3 was added to the samples. Then, Sr is extracted by an ion exchange method using handmade Teflon (3 mm in diameter, 15 mm of long) column with Eichron Sr spec resin (100-150 mesh) following the procedure described by Na et al. (1995). Sr isotopic ratios were determined using a Thermo Fisher mass spectrometry (NEPTUNE) at the Research Institute for Humanity and Nature, Kyoto, Japan. The measured $^{87}Sr/^{86}Sr$ was normalized on the basis that the $^{87}Sr/^{86}Sr$ of NBS 987 is 0.710251 ± 4. The within-run precision (2σ) for $^{87}Sr/^{86}Sr$ was ± 0.000014 to 0.000015.

6.4 Analytical results of strontium isotopic ratios

The analytical results are shown in Table 14. Initial $^{87}Sr/^{86}Sr$ ratios are calculated from measured strontium isotopic ratios and concentrations of Rb and Sr, assuming the age of formation as 258 Ma for weakly altered andesite lava, 250 Ma for strongly altered andesite lava and Au-bearing quartz veins and calcite veins and 244 Ma for post-mineralization andesite dike and granodiorite porphyry (Salam et al., 2013). Siltstone and shale of Carboniferous strata are assumed at 250 Ma, which is the same as the age of the Au-mineralization. The equation for calculation of initial $^{87}Sr/^{86}Sr$ is shown in below:

$$^{87}Sr/^{86}Sr_m = {}^{87}Sr/^{86}Sr_i + {}^{87}Rb/^{86}Sr \ (e^{\lambda t} - 1), \quad (1)$$

where $^{87}Sr/^{86}Sr_m$ is measured of $^{87}Sr/^{86}Sr$ ratio of each sample and $^{87}Sr/^{86}Sr_i$ is initial of $^{87}Sr/^{86}Sr$ ratio of each sample. λ is the decay constant of ^{87}Rb ($1.42 \times 10^{-11}\ y^{-1}$). $^{87}Rb/^{86}Sr$ is the ratio of these isotopes in terms of numbers of atomic ratios (mole ratio), and obtained by the following way. Rb has two isotopes of ^{85}Rb and ^{87}Rb. The abundance of ^{85}Rb and ^{87}Rb are 72.1654% and 27.8346%, respectively. Its atomic weight is 85.46776. The abundance of ^{87}Rb in 1000 g of sample is following as.

$$^{87}Rb = \frac{1000 \times Rb_c \times 10^{-6}}{85.46776} \times 0.278346, \quad (2)$$

where Rb_c is a total concentration of Rb of each sample.

Table 15 Abundance of Strontium isotopes

Isotopic ratios	Abundance	Percentage abundance of strontium isotope	Average atomic weight of strontium
^{84}Sr	0.0068	0.56	83.9134
^{86}Sr	0.1194	9.86	85.9093
^{87}Sr	0.0842*	6.96	86.9089
^{88}Sr	1.0000	82.61	87.9056
Sum	1.2104		
			87.6169

*0.1194 x 0.705563

Strontium has four isotopes of ^{88}Sr, ^{87}Sr, ^{86}Sr and ^{84}Sr in nature. The abundances of ^{88}Sr, ^{87}Sr and ^{84}Sr in nature are constant as shown in Table 15. However, the abundance of ^{87}Sr is variable because of the formation of radiogenic ^{87}Sr by the decay of ^{87}Rb and the atomic weight of Sr is different in each sample. The following example shows how the atomic weight is calculated. If Sr content of andesite lava is 530 ppm and measured $^{87}Sr/^{86}Sr$ ratio of andesite lava is 0.705563, the abundance of ^{87}Sr in 1000 g of sample is calculated according to the following equation.

$$^{86}Sr = \frac{1000 \text{ X } Sr_c \text{ X } 10^{-6}}{87.6169} \text{ X } 0.0986, \qquad (3)$$

where Sr_c is a total concentration of Sr of each sample. Based on the abundances of ^{87}Rb and ^{86}Sr using equation (2) and (3) and the measured $^{87}Sr/^{86}Sr$ of sample, initial ratios of $^{87}Sr/^{86}Sr$ of sample was calculated.

6.5 Strontium isotopic ratios of weakly altered andesite lava and strongly altered andesite lava

The measured $^{87}Sr/^{86}Sr$ ratios of strongly altered andesite lavas, weakly altered andesite lavas and post-mineralization andesite dikes are different (Table 14 and Fig. 6.6A). The measured $^{87}Sr/^{86}Sr$ ratio of the weakly altered andesite lava at the Q prospect is 0.705563. The measured $^{87}Sr/^{86}Sr$ ratios of strongly altered andesite lavas at the A pit and Q prospect are 0.723909 and 0.725220, respectively. The measured $^{87}Sr/^{86}Sr$ ratios of post-mineralization andesite dike at the A pit and Q prospect are 0.705566 and 0.705676, respectively.

The initial $^{87}Sr/^{86}Sr$ ratios of weakly altered and strongly altered andesite lavas are shown in Fig. 6.6B. The initial $^{87}Sr/^{86}Sr$ ratio of weakly altered andesite lava at the Q prospect is 0.705118. The initial $^{87}Sr/^{86}Sr$ ratios of strongly altered andesite lava of Q prospect and the A pit are 0.7070632 and 0.709235, respectively. The initial $^{87}Sr/^{86}Sr$ ratios of strongly altered andesite lavas are higher than initial $^{87}Sr/^{86}Sr$ ratio of weakly altered andesite and weakly altered post-mineralization andesite dikes. The initial $^{87}Sr/^{86}Sr$ ratios of the strongly altered andesite lavas are higher than the initial $^{87}Sr/^{86}Sr$ ratios of Permian sea water (0.707; DePaolo and Ingram, 1985). Relation between Rb and Sr contents of the strongly altered andesite lavas, weakly altered andesite lava and post-mineralization andesite dikes are shown in Fig. 6.7. The weakly altered andesite lava and weakly altered post-mineralization andesite dikes have higher Sr contents than the strongly altered andesite lavas, while Rb content of strongly altered andesite lavas are slightly higher than Rb content of weakly altered andesite lava and weakly altered post-mineralization andesite dikes. The $^{87}Sr/^{86}Sr$ ratios of rocks are correlated with the ratio of $^{87}Rb/^{86}Sr$ of rocks.

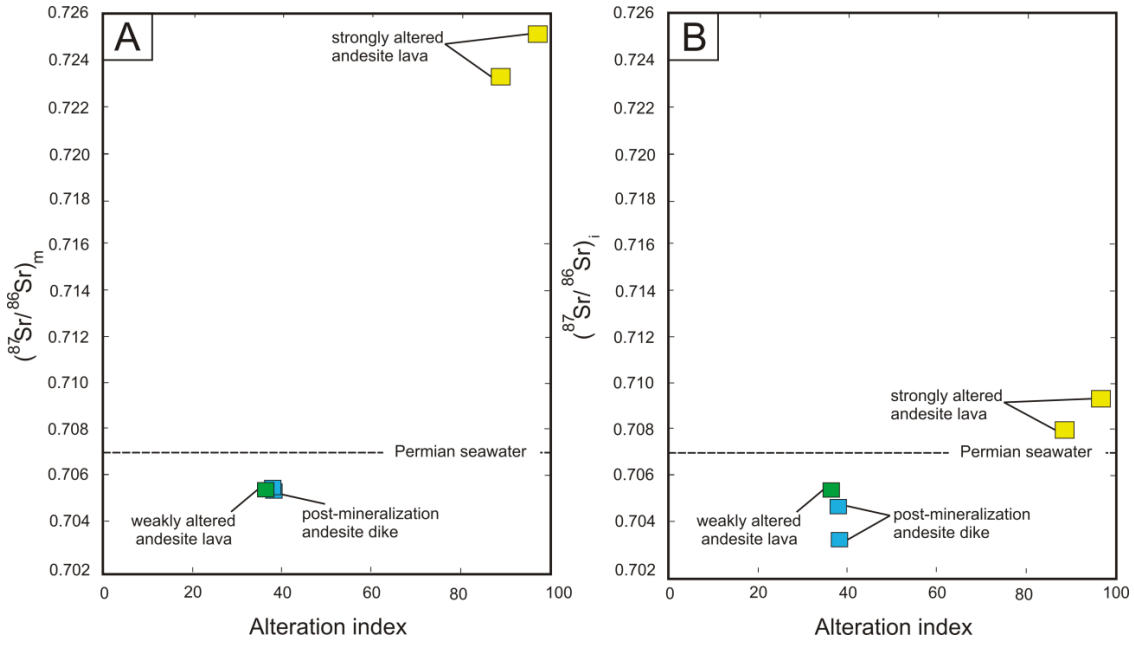

Figure 6.6 Diagrams showing the relation between (A) alteration index and measured strontium isotopic ratios and (B) alteration index and initial strontium isotopic ratios of weakly altered andesite lavas, strongly altered andesite lavas and post-mineralization andesite dikes. Strontium isotopic ratio of sea water in Permian age is from DePaolo and Ingram (1985).

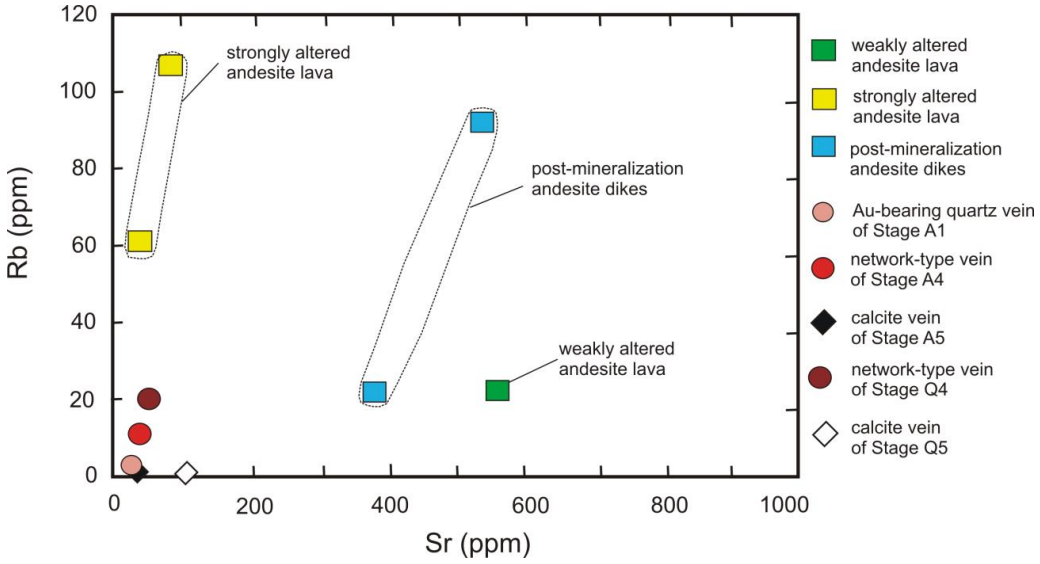

Figure 6.7 Diagram showing relation of Sr and Rb contents among weakly altered andesite, post-mineralization andesite dikes, strongly altered andesite lavas, quartz veins and calcite veins.

$^{87}Rb/^{86}Sr$ ratios of the strongly altered andesite lavas are higher than $^{87}Rb/^{86}Sr$ ratios of the weakly altered andesite lava. This is due to the large different in $^{87}Rb/^{86}Sr$ of the strongly and weakly altered andesite lavas. The relation between initial $^{87}Sr/^{86}Sr$ ratios and $^{87}Rb/^{86}Sr$ ratios is plotted shown in Fig. 6.8.

If the original andesite of strongly and weakly altered andesite lavas are same, it is suggested that the high initial $^{87}Sr/^{86}Sr$ and high $^{87}Rb/^{86}Sr$ ratios of strongly altered andesite lavas were formed by water/rock interaction between the weakly altered andesite lava and hydrothermal solution having high $^{87}Sr/^{86}Sr$ ratio. The hydrothermal solution having high $^{87}Sr/^{86}Sr$ ratio was derived from deeper section to shallow section such as in the Chatree deposit. The hydrothermal solution reacted with weakly andesite lava in shallow section, then strongly altered andesite lavas were formed (Fig. 6.9). In this water/rock reaction, the initial $^{87}Sr/^{86}Sr$ ratio of strongly altered andesite was raised.

The high initial $^{87}Sr/^{86}Sr$ and high $^{87}Rb/^{86}Sr$ ratios of strongly altered andesite lavas were formed by water/rock interaction between the weakly altered andesite lava and hydrothermal solution having high $^{87}Sr/^{86}Sr$ ratio. The hydrothermal solution having high $^{87}Sr/^{86}Sr$ ratio was derived from deeper section to shallow section in the Chatree deposit. The hydrothermal solution reacted with weakly andesite lava in shallow section, then strongly altered andesite lavas were formed (Fig. 6.9).

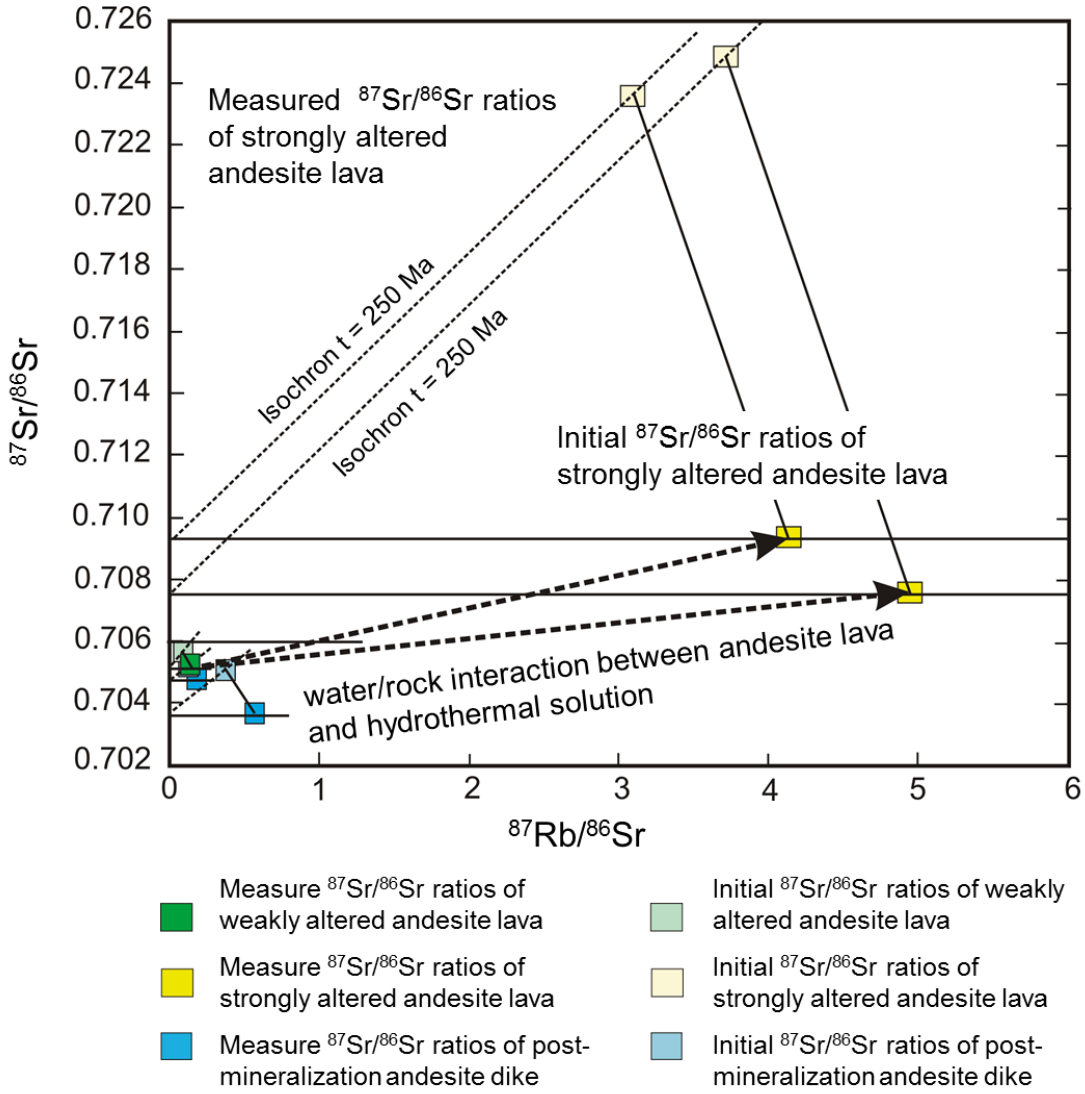

Figure 6.8 Diagram showing relation of $^{87}Rb/^{86}Sr$ and $^{87}Sr/^{86}Sr$ ratios among weakly altered andesite lava, strongly altered andesite lavas and post-mineralization andesite dikes.

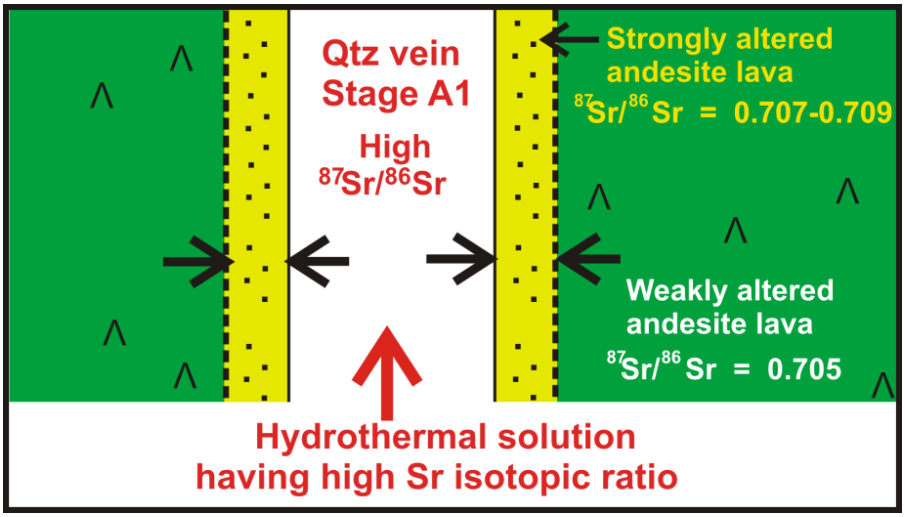

Figure 6.9 Schematic diagram showing the occurrence of strongly altered andesite lava having higher $^{87}Sr/^{86}Sr$ as a result of water/rock interaction between the hydrothermal solution having high strontium isotopic ratio and weakly altered andesite lava.

6.6 Strontium isotopic ratios of the Au-bearing quartz veins and calcite veins of the Chatree deposit

The Au-bearing quartz veins of Stage A1 and network-type veins of Stage A4 at the A pit and the Au-bearing quartz veins of Stage Q1 and network-type veins of Stage Q4 at the Q prospect are composed of quartz, adularia, calcite and sulfide minerals containing large amounts of gold. Calcite vein of Stage A5 at the A pit and calcite vein of Stage Q5 at the Q prospect are composed of a large amount of calcite and small amount of sulfide minerals and gold (Fig. 6.10 and 6.11).

The $^{87}Sr/^{86}Sr$ ratios of the Au-bearing quartz veins and calcite veins of the A pit and Q prospect are shown in Table 14. The measured $^{87}Sr/^{86}Sr$ ratios of the Au-bearing quartz veins of Stage Q4 and calcite vein of Stage Q5 are 0.711655 and 0.705190, respectively. The measured $^{87}Sr/^{86}Sr$ ratios of the Au-bearing quartz veins of Stages A1 and A4 and calcite vein of Stage A5 are 0.707597, 0.720887 and 0.705566, respectively. The initial $^{87}Sr/^{86}Sr$ ratios of the network-type vein of Stage Q4 and calcite vein of Stage Q5 at Q prospect are calculated to be 0.708254 and 0.705146, respectively. The initial $^{87}Sr/^{86}Sr$ ratios of the Au-bearing quartz veins of Stage A1 range from 0.706164 to 0.708293. The initial $^{87}Sr/^{86}Sr$ ratios of the network-type vein of Stage A4 and calcite vein of Stage A5 at the A pit are estimated to be 0.717607 and 0.704843, respectively. The relation between paragenetic sequence and the initial $^{87}Sr/^{86}Sr$ ratios of the Au-bearing quartz veins at the A pit and Q prospect are shown in Figs. 6.10 and 6.11. The initial $^{87}Sr/^{86}Sr$ ratios of the Au-bearing network-type vein of Stage A4 at A pit and the Au-bearing network-type vein of Stage Q4 at Q prospect are higher than those of calcite veins of Stage A5 at A pit and Stage Q5 at the Q prospect. Rb and Sr contents of the Au-bearing quartz veins of Stage A1, network-type veins of Stage A4 and calcite veins of Stage A5 at the A pit and network-type veins of Stage Q4

and calcite veins of Stage Q5 at the Q prospect are shown in Fig. 6.7. Sr contents of the Au-bearing quartz vein of Stage A1, network-type veins of Stages A4 and calcite vein of Stage A5 at the A pit, network-type veins of Stages Q4 and calcite vein of Stage Q5 at Q prospect are similar. However, Rb contents of the Au-bearing network-type veins of Stage A4 at the A pit and the Au-bearing network-type veins of Stage Q4 at Q prospect are higher than those of calcite vein of Stage A5 at the A pit and Stage Q5 at Q prospect.

The initial $^{87}Sr/^{86}Sr$ ratios of the Au-bearing quartz vein of Stage A1 at the A pit and the network-type vein of Stage Q4 at the Q prospect are similar with initial $^{87}Sr/^{86}Sr$ ratios of the strongly altered andesite lavas. The initial $^{87}Sr/^{86}Sr$ ratios of the Au-bearing network-type vein of Stage A4 is the highest among the samples examined in this study. The high $^{87}Sr/^{86}Sr$ ratios of the strongly altered andesite lava and the Au-bearing type vein of Stage A4 at the A pit are similar to $^{87}Sr/^{86}Sr$ ratios of sedimentary rocks (Fig. 6.13). This fact suggests that the Au-bearing quartz veins and the network-type veins were formed by hydrothermal solution having high $^{87}Sr/^{86}Sr$ ratio (Fig. 6.9). There is a possibility that the hydrothermal solution forming Au mineralization reacted with sedimentary strata in deeper section of the Chatree deposit. The hydrothermal solution that reacted with sedimentary strata is thought to be related to the Au mineralization of the Chatree deposit based on the relation between high $^{87}Sr/^{86}Sr$ ratio and higher Au content of the Au-bearing quartz vein of the Chatree deposit. However, the initial $^{87}Sr/^{86}Sr$ ratios of Carboniferous siltstones and shale range from 0.705942 to 0.706313 (Table 14). Unlike the hydrothermal solution, these Carboniferous siltstones and shale do not show high $^{87}Sr/^{86}Sr$ ratios . One of the possibilities is that sedimentary rocks derived from the Shan-Thai Terrane which has signature of continental crust are situated beneath the Chatree mining area, and the Au-bearing hydrothermal solution having high $^{87}Sr/^{86}Sr$ ratio could have formed by interaction between hydrothermal solution

and sedimentary rocks having higher $^{87}Sr/^{86}Sr$ ratios than the $^{87}Sr/^{86}Sr$ ratios of the Carboniferous siltstones and shale. An instance of such a case is the initial high $^{87}Sr/^{86}Sr$ ratios of Shimanto sedimentary rocks underlying the Hishikari deposit, which are in the range from 0.709651 to 0.725411 (Hosono et al., 2003).

The relation between initial $^{87}Sr/^{86}Sr$ ratios and Au contents of the Au-bearing quartz veins of Stage A1 and the Au-bearing network-type vein of Stage A4 at the A pit and the Au-bearing network-type vein of Stage Q4 at Q prospect are shown in Fig. 6.12. Except for the high $^{87}Sr/^{86}Sr$ ratios of network-type vein of Stage A4, the $^{87}Sr/^{86}Sr$ ratios of the other four veins are fairly constant without any particular relation to the Au contents. This suggests that (1) source of gold was from magma that was related volcanic activity of andesitic volcanics of the Chatree mining area (2) Au-bearing hydrothermal solution of high $^{87}Sr/^{86}Sr$ ratio was transported early and immediately after the formation of fracture. The Au-bearing hydrothermal solution having lower $^{87}Sr/^{86}Sr$ ratios that is similar to the $^{87}Sr/^{86}Sr$ ratios of andesite lava was transported in the period of intense Au-mineralization and (3) the hydrothermal solution forming the Au-bearing quartz veins was kept in deeper section for a while and then transported to shallow section intermittently as pulses.

$^{87}Sr/^{86}Sr$ ratios of calcite vein are lower than $^{87}Sr/^{86}Sr$ ratios of Au-bearing quartz veins. The lower $^{87}Sr/^{86}Sr$ ratios of calcite veins of Stage A5 and Stage Q5 suggest that the size of circulation of hydrothermal systems forming Au-bearing quartz veins and calcite veins is thought to be different. The hydrothermal solution forming the Au-bearing quartz veins were derived from the deeper section, while the hydrothermal system forming calcite veins is thought to be circulated in shallow strata around the Chatree deposit.

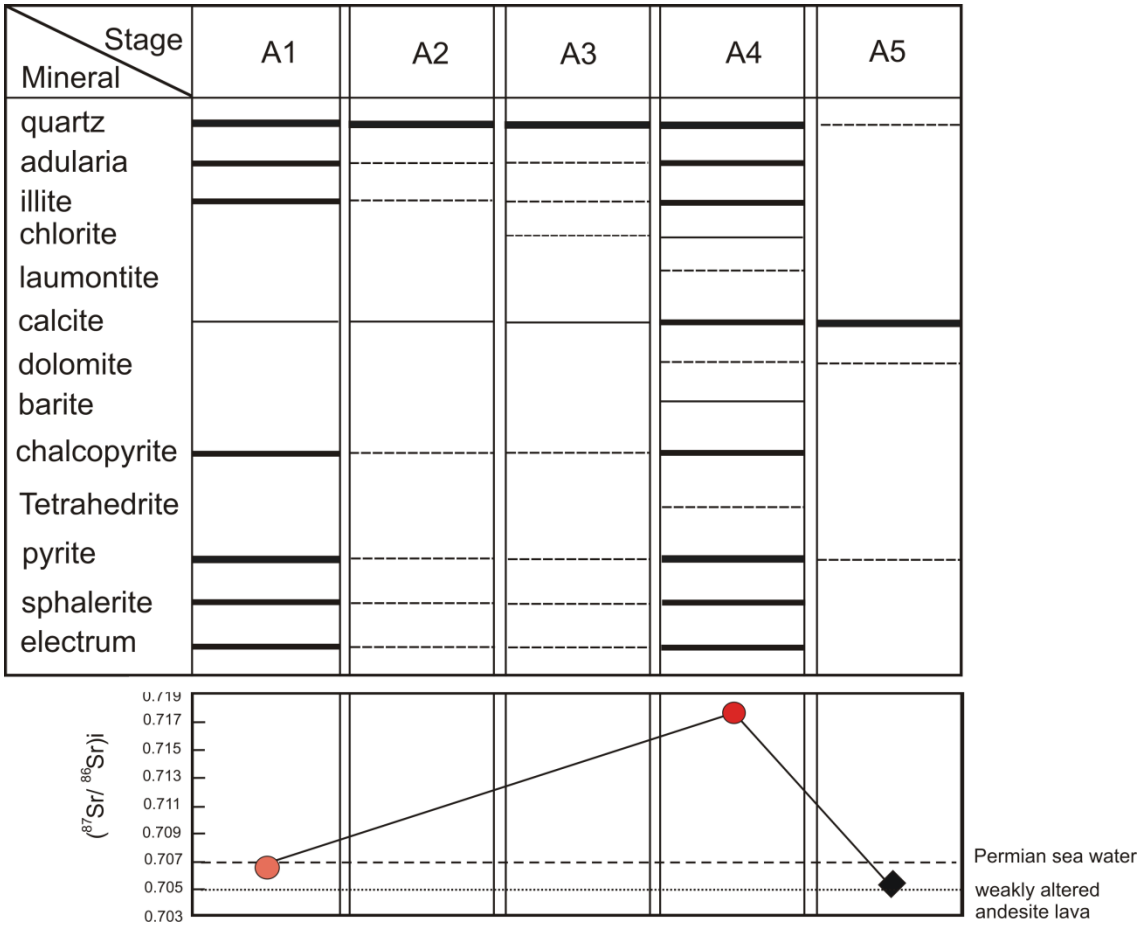

Figure 6.10 Variation of $^{87}Sr/^{86}Sr$ ratios from the Au-bearing quartz veins and calcite veins of Stage A1 to Stage A5 of A pit. The Au-bearing quartz veins of Stage A1 and Stage A4 have high Au contents and higher initial $^{87}Sr/^{86}Sr$ ratios, while calcite vein of Stage A5 has low initial $^{87}Sr/^{86}Sr$ ratio.

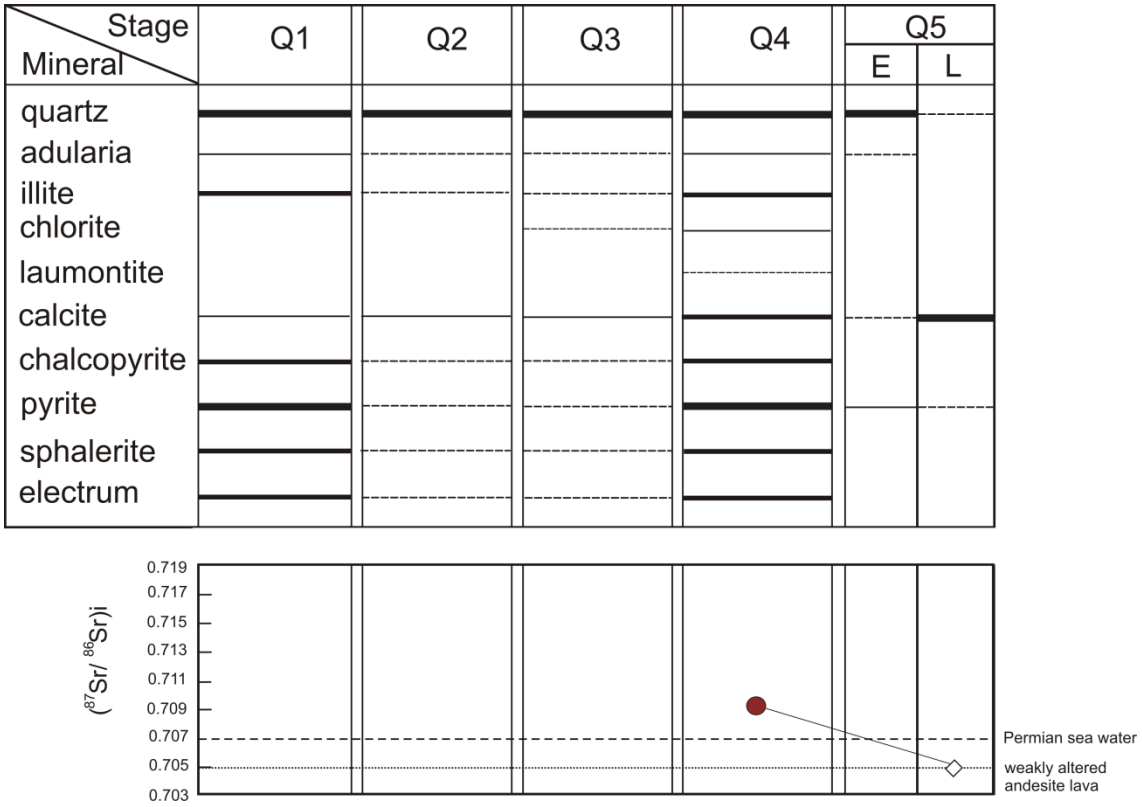

Figure 6.11 Variation of $^{87}Sr/^{86}Sr$ ratios of the Au-bearing quartz veins of Stage Q1 to Stage Q5 at the Q prospect. The $^{87}Sr/^{86}Sr$ ratios decrease from the Au-bearing quartz veins of Stage Q4 to the calcite vein of Stage Q5.

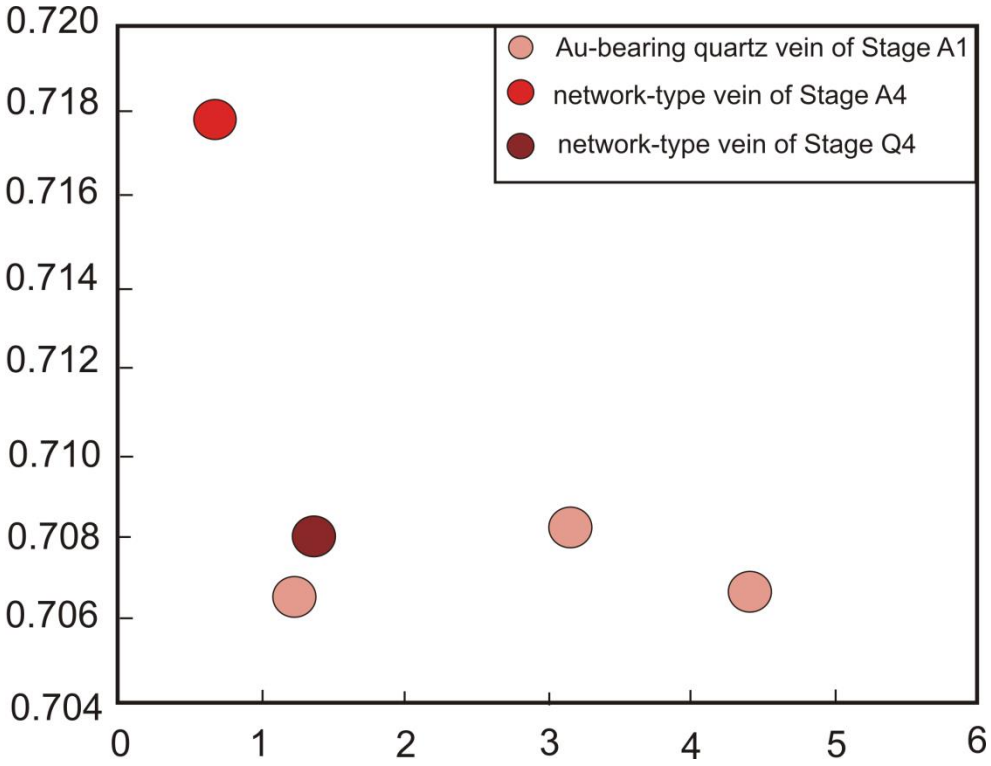

Figure 6.12 Diagram showing the relation between initial $^{87}Sr/^{86}Sr$ ratios and gold contents in the Au-bearing quartz veins of the A pit and Q prospect.

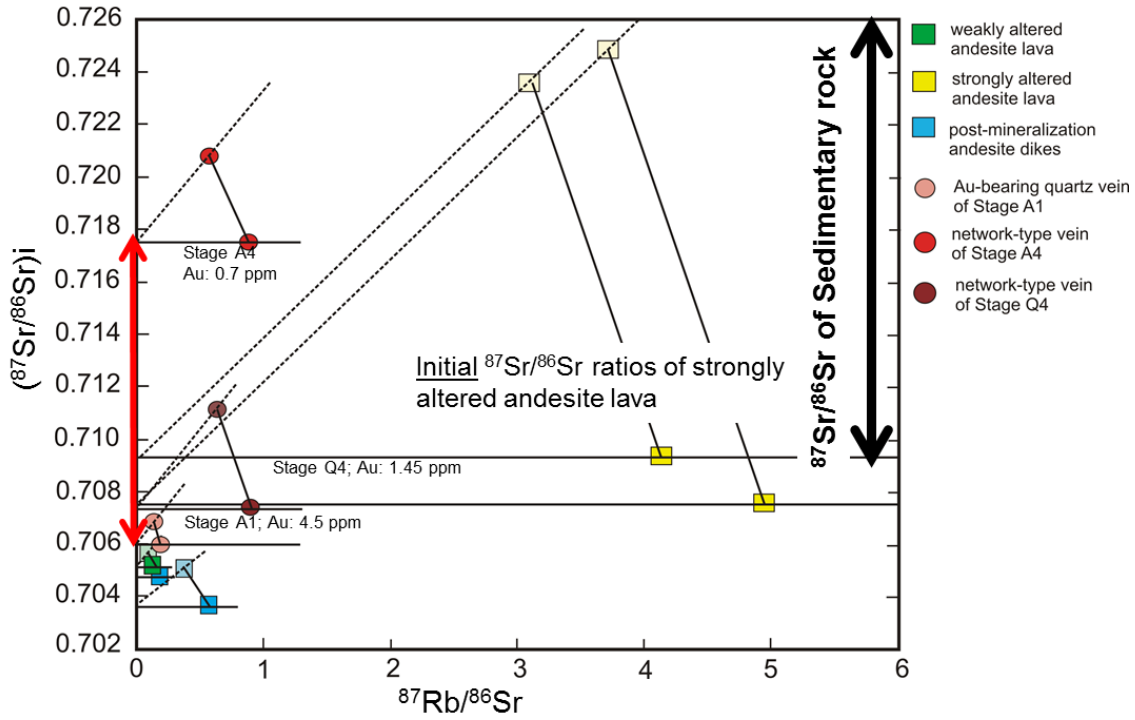

Figure 6.13 The initial $^{87}Sr/^{86}Sr$ and $^{87}Rb/^{86}Sr$ of the Au-bearing quartz veins of A1, A4, A5 at the A pit and Q4 and Q5 at the Q prospect are plotted. The $^{87}Sr/^{86}Sr$ ratios of sedimentary rocks in Hishikari gold-silver deposit range from 0.709 to 0.726 (Hosono et al., 2003)

6.7 Origin of the hydrothermal solution at the Chatree deposit

The $^{87}Sr/^{86}Sr$ ratio of the Au-bearing quartz veins and strongly altered andesite lava suggests that Carboniferous sedimentary strata were present near a magmatic environment. If it is the case, then there is a possibility that a fluid has higher $\delta^{18}O$ ratios under the magmatic environment. To estimate $\delta^{18}O$ ratio of fluid, a calculation was carried out assuming closed system and, where the initial $\delta^{18}O$ ratios of water and sedimentary rocks are +8‰ and +14‰, respectively. The final $\delta^{18}O$ ratio of fluid was estimated +14‰ at temperature of 500^0C under a rock-dominant condition (Fig. 6.14). If the fluid is transported to the shallow section of the Chatree deposit and precipitates quartz at 250^0C, the $\delta^{18}O$ ratios quartz is +24‰ because of fractionation between quartz and H_2O at temperature of 250^0C. However, the $\delta^{18}O$ ratios of quartz of the Au-bearing quartz veins of Stages 1 to 4 at the Chatree deposit range from +10.4 to +15.0‰. The fluid having high $\delta^{18}O$ ratio such as +14‰ is difficult to form the Au-bearing quartz veins of the Chatree deposit. Representative $\delta^{18}O$ ratios of quartz from the Chatree deposit is approximately +12‰. Based on the formation temperature of 250^0C and fractionation factor between quartz-H_2O, the $\delta^{18}O$ ratios of the hydrothermal solution is +2‰. Therefore, there is a possibility that the fluid of magmatic water derived from the deeper section mixed with water having low $\delta^{18}O$ ratio such as seawater or meteoric water (see Chapter 4). However, if the $^{87}Sr/^{86}Sr$ ratio of hydrothermal solution is controlled by the reaction with sedimentary rocks, as discussed above, the influence of such mixing of low $\delta^{18}O$ water on the $^{87}Sr/^{86}Sr$ ratio is left to be explained.

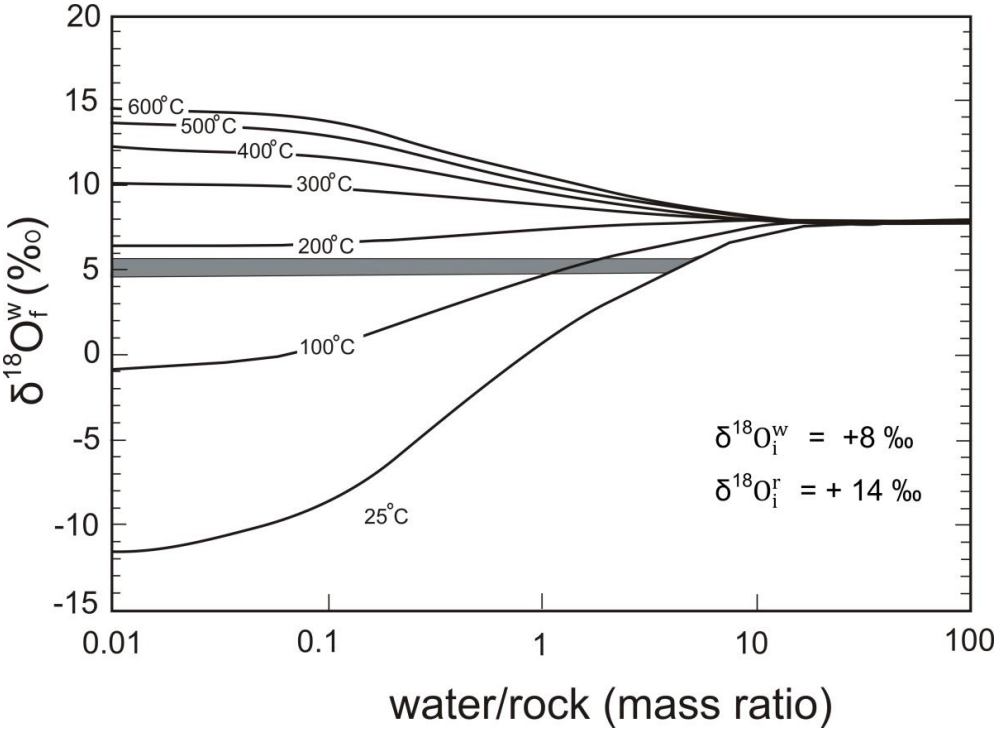

Figure 6.14 Calculation of the final $\delta^{18}O$ ratio of water based on initial water being +8‰ and initial sedimentary rocks being +14‰.

6.8 Strontium isotopic ratios of andesite lava and granodiorite porphyry at the N and V prospects

The measured and initial $^{87}Sr/^{86}Sr$ ratios of weakly altered andesite lavas, strongly altered granodiorite porphyry at the N and V prospects and least altered diorite are shown in Table 14. The initial $^{87}Sr/^{86}Sr$ ratios of weakly altered andesite lavas at the N and V prospects range from 0.705212 to 0.705309, respectively. The initial $^{87}Sr/^{86}Sr$ ratios of strongly altered granodiorite porphyry at the N prospect range from 0.704213 to 0.704219. The initial $^{87}Sr/^{86}Sr$ ratio of least altered diorite is 0.704187. The initial $^{87}Sr/^{86}Sr$ ratios of strongly altered granodiorite porphyry of the N prospect are similar to the initial $^{87}Sr/^{86}Sr$ ratios of fresh diorite (Fig. 6.14). The relation between initial $^{87}Sr/^{86}Sr$ ratios and degree of alteration of andesite lavas, granodiorite porphyry at the N and V prospects and fresh diorite away from the Chatree deposit is shown in Fig. 6.14. The weakly altered andesite lavas at the N and V prospects and weakly altered andesite lava at the Q prospect were plotted in the range of alteration index of least altered rocks of VMS deposit. The initial $^{87}Sr/^{86}Sr$ ratios of weakly altered andesite lavas at the N and V prospects are similar to the $^{87}Sr/^{86}Sr$ ratio of weakly altered andesite lava at the Q prospect and are higher than initial $^{87}Sr/^{86}Sr$ ratios of strongly altered granodiorite porphyry and least altered diorite. Relation between the $^{87}Sr/^{86}Sr$ ratio and $^{87}Rb/^{86}Sr$ ratio of weakly altered andesite lavas, strongly altered granodiorite porphyry at the N and V prospects, and least altered diorite is shown in Fig. 6.15. The weakly altered andesite lavas at the N and V prospects having high initial $^{87}Sr/^{86}Sr$ ratios have higher $^{87}Rb/^{86}Sr$ ratios compared with the strongly altered granodiorite porphyry and least altered diorite. The difference of initial $^{87}Sr/^{86}Sr$ ratios suggests that andesite lava and granodiorite porphyry are formed by different magmatic activities. This idea is supported by the relations of TiO_2 and Zr contents and REE patterns of weakly altered andesite lava and

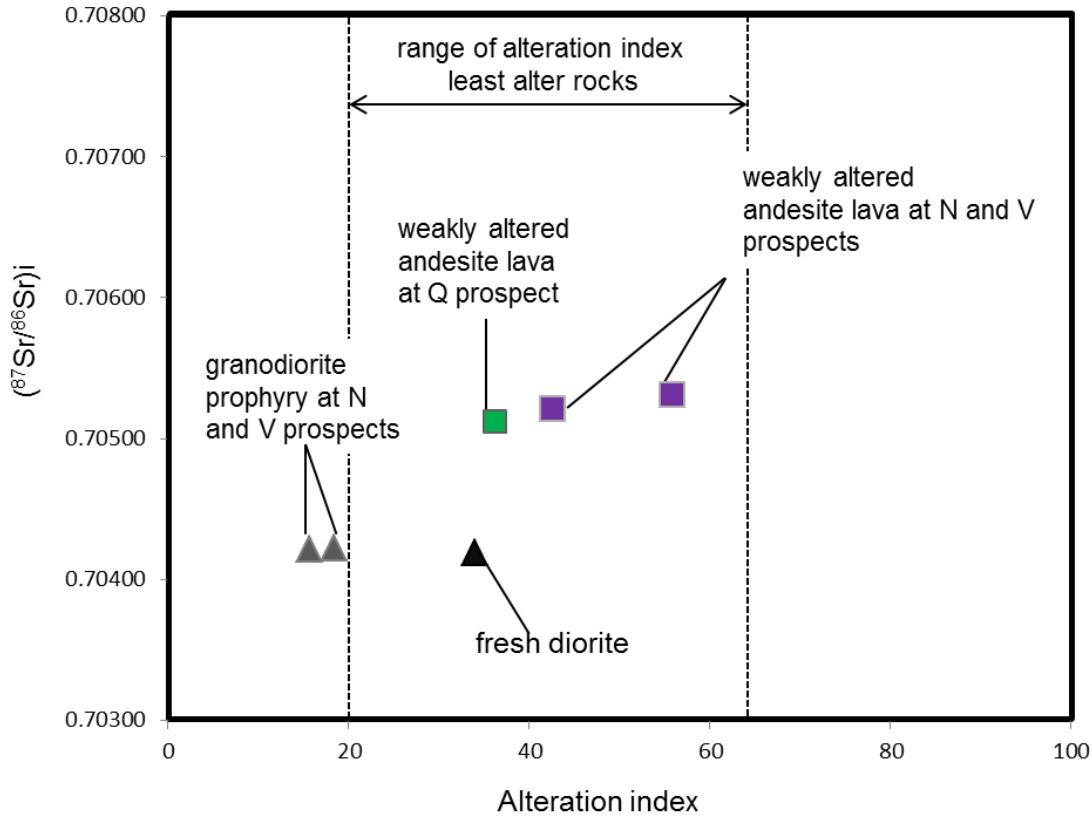

Figure 6.15 The relation of alteration index and initial $^{87}Sr/^{86}Sr$ ratios of andesite lavas, granodiorite porphyry at the N and V prospects, weakly altered andesite lava and fresh diorite.

strongly altered granodiorite porphyry (Chapter 3). Cu-Mo mineralization associated with granodiorite porphyry is different from the Au-mineralization associated with andesitic magma forming andesite lava.

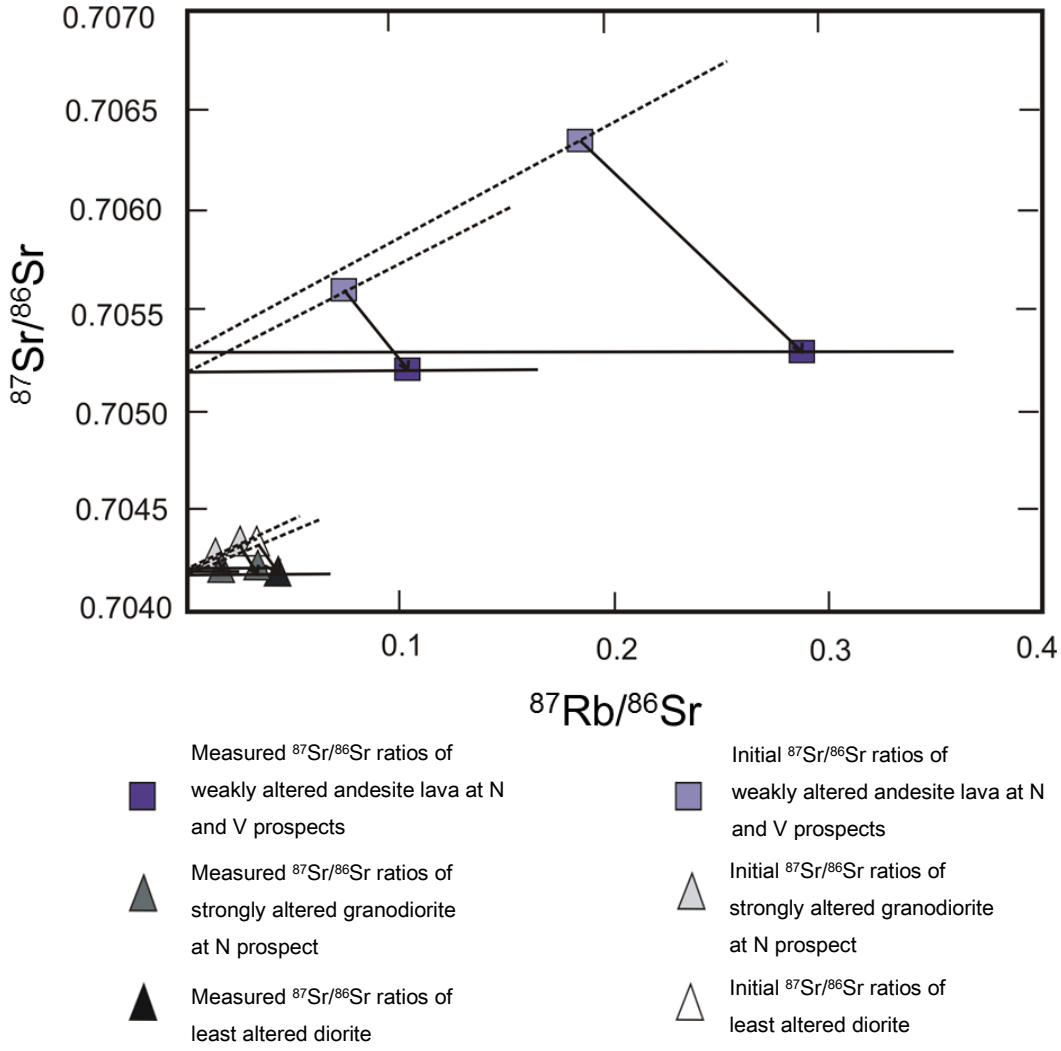

Figure 6.16 Diagram showing relation of $^{87}Rb/^{86}Sr$ and initial $^{87}Sr/^{86}Sr$ ratios among weakly altered andesite lavas, strongly altered granodiorite porphyry and least altered diorite.

6.9 Genetic model of the hydrothermal system of Au mineralization of the Chatree deposit

Model of the hydrothermal system of the Chatree gold deposit based on the initial $^{87}Sr/^{86}Sr$ ratios and Au contents of the strongly altered andesite lava, weakly altered andesite lava and Au-bearing quartz veins is shown in Fig. 6.16. The initial $^{87}Sr/^{86}Sr$ ratios of strongly altered andesite lava and the Au-bearing network-type veins of Stage A4 at the A pit are 0.708765 and 0.717607, respectively. The initial $^{87}Sr/^{86}Sr$ ratios of the strongly altered andesite lavas and the Au-bearing network-type veins of Stage A4 at the A pit are similar to the initial $^{87}Sr/^{86}Sr$ ratios of sedimentary or metamorphic rocks (0.709 to 0.726; Hosono et al., 2003). This suggests that the hydrothermal solution reacted with sedimentary rock or metamorphic rock having higher $^{87}Sr/^{86}Sr$ ratios in deeper section beneath the Chatree mining area. On the other hand, the initial $^{87}Sr/^{86}Sr$ ratios of the Au-bearing quartz veins of Stage A1 at the A pit are similar to the initial $^{87}Sr/^{86}Sr$ ratio of weakly altered andesite lava. If the Au-bearing hydrothermal fluid was derived from andesitic magma and reacted with the sedimentary strata, the hydrothermal solution could have high $^{87}Sr/^{86}Sr$ ratio. Fluid forming Au-mineralization of the Chatree deposit is thought to be formed under an environment where sediment strata and andesitic magma coexisted. Therefore, the fluid forming Au-mineralization of the Chatree deposit could be formed in magmatic environment in which andesitic magma was present with sedimentary strata. The Au-rich fluid was formed near magmatic environment before development of fracture (Fig. 6.16A). The portion that Au-rich fluid was kept near magmatic environment is thought to be storage of ore fluid. The fluid having high $^{87}Sr/^{86}Sr$ ratio and Au content was transported to shallow section by the development of fracture. The hydrothermal solution having high $^{87}Sr/^{86}Sr$ ratio reacted with fresh andesite lava to form strongly altered andesite lava having high $^{87}Sr/^{86}Sr$ ratio. The Au-

bearing quartz vein having high $^{87}Sr/^{86}Sr$ ratios was also formed by the hydrothermal solution having high $^{87}Sr/^{86}Sr$ ratio (Fig. 6.16B). After the Au-bearing quartz vein of Stage 1 was formed, there is a possibility that the fracture was sealed. Before development of new fractures, the fluid in storage near magmatic environment reacted with sedimentary strata in the deeper section again. Then the Au-bearing network-type veins of Stage 4 having high $^{87}Sr/^{86}Sr$ ratios of the Chatree deposit were formed immediately after the formation of new fractures (Fig. 6.16B). The fact that $^{87}Sr/^{86}Sr$ ratio decreased and Au content increased in the Au-bearing network-type veins from early to later periods in the formation of the network-type vein suggest that fluid reacted with the sedimentary rocks and were transported in early period. The Au-rich fluid derived from magma that was transported in later period. Fractures from the deeper to shallow sections were sealed at a certain point in the period of the Au-mineralization, the calcite veins was formed by the hydrothermal solution circulating a shallow section of the deposit(Fig. 6.16C).

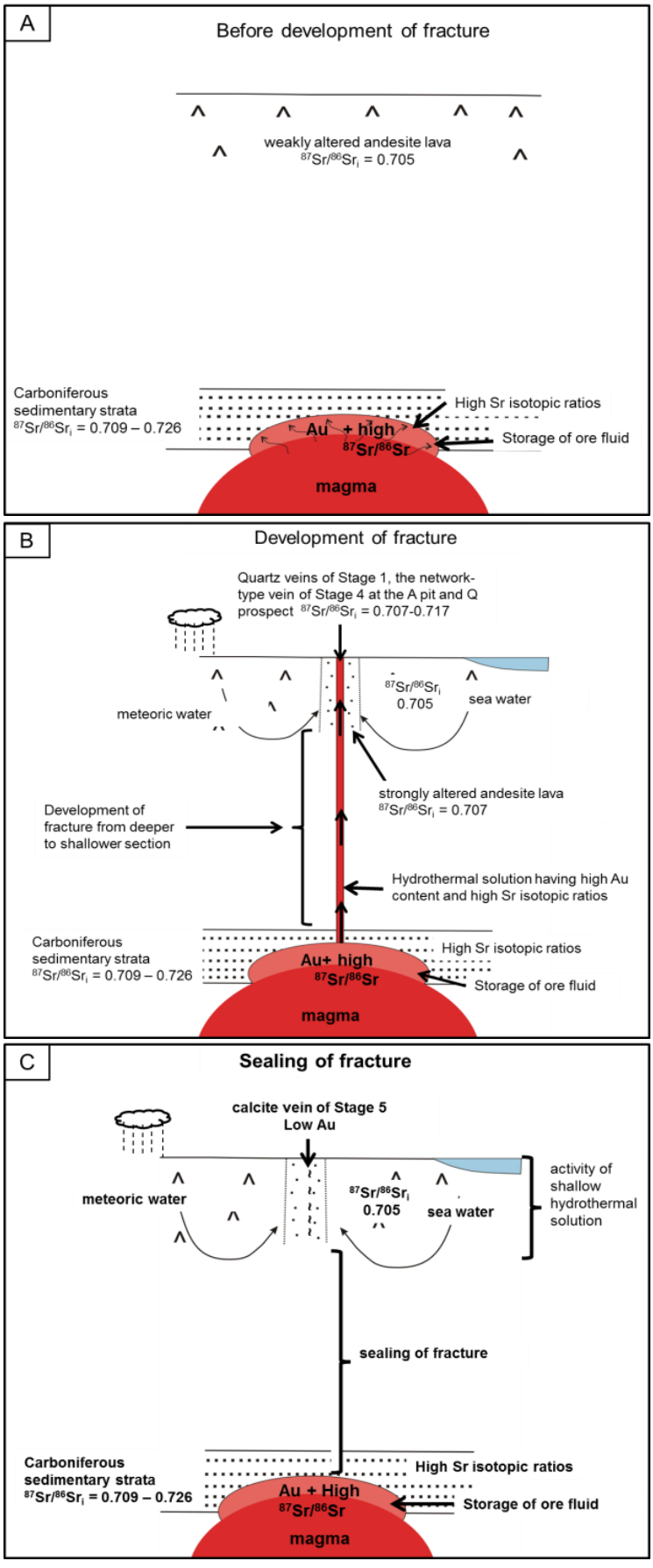
A
Before development of fracture
weakly altered andesite lava
$^{87}Sr/^{86}Sr_i$ = 0.705
Carboniferous sedimentary strata
$^{87}Sr/^{86}Sr_i$ = 0.709 – 0.726
High Sr isotopic ratios
Au + high $^{87}Sr/^{86}Sr$
Storage of ore fluid
magma
B
Development of fracture
Quartz veins of Stage 1, the network-type vein of Stage 4 at the A pit and Q prospect $^{87}Sr/^{86}Sr_i$ = 0.707-0.717
meteoric water
$^{87}Sr/^{86}Sr_i$ 0.705
sea water
strongly altered andesite lava
$^{87}Sr/^{86}Sr_i$ = 0.707
Development of fracture from deeper to shallower section
Hydrothermal solution having high Au content and high Sr isotopic ratios
Carboniferous sedimentary strata
$^{87}Sr/^{86}Sr_i$ = 0.709 – 0.726
High Sr isotopic ratios
Au+ high $^{87}Sr/^{86}Sr$
Storage of ore fluid
magma
C
Sealing of fracture
calcite vein of Stage 5
Low Au
meteoric water
$^{87}Sr/^{86}Sr_i$ 0.705
sea water
activity of shallow hydrothermal solution
sealing of fracture
Carboniferous sedimentary strata
$^{87}Sr/^{86}Sr_i$ = 0.709 – 0.726
High Sr isotopic ratios
Au + High $^{87}Sr/^{86}Sr$
Storage of ore fluid
magma

Figure 6.17 Genetic model of the Au-bearing quartz veins of Stage 1 to Stage 4 and calcite vein of Stage 5 at the A pit and the Q prospect. (A) The genetic model showing activity in the deeper section at the Chatree mining area before development of fracture. Sedimentary strata were formed near a magmatic environment. Au-rich fluid in the deeper section reacted with sedimentary strata to have high $^{87}Sr/^{86}Sr$ ratio. This portion is the storage of ore fluid. (B) Fractures were developed from the deeper section to shallow section at the Chatree mining area, allowing the hydrothermal solution having high $^{87}Sr/^{86}Sr$ ratios from the storage of ore fluid to be transported to shallow section. The hydrothermal solution interacted with fresh andesite lava at the A pit and Q prospect. The Au-bearing quartz veins of Stage 1, the Au-bearing network-type veins of Stage 4 at the A pit and Q prospect was formed by the hydrothermal solution having high$^{87}Sr/^{86}Sr$ ratios. (C) The genetic model showing sealed fracture. Calcite vein of Stage 5 at the A pit and Q prospect were formed by activity of hydrothermal solution in a shallow section.

Chapter 7: Conclusions

Characteristics of Au mineralization at the Chatree deposit are summarized as follows.

1. Andesite lava, post-mineralization andesite dike and granodiorite porphyry are thought to be of different igneous activities. Au-mineralization and Cu-Mo mineralization were associated with igneous activities related to andesite lava and granodiorite porphyry, respectively.
2. The Au-bearing quartz veins of the Chatree deposit can be separated into five stages. The Au-bearing quartz veins of Stages 1 and 4 are major Au-mineralization stage. The Au-bearing quartz veins of Stages 1 and 4 at the Q prospect are characterized by microcrystalline and flamboyant textures that suggest rapid crystal growth from supersaturated hydrothermal solution as a result of boiling. The formation temperature and depth are estimated to be around 200^{0}C and 200m below paleosurface, respectively.
3. The initial $^{87}Sr/^{86}Sr$ ratios of the Au-bearing quartz veins of Stage 1 and 4 are higher than initial $^{87}Sr/^{86}Sr$ ratios of barren calcite veins of Stage 5.
4. The initial $^{87}Sr/^{86}Sr$ ratios of the Au-bearing quartz network-type vein of Stage 4 and the strongly altered andesite lava at the A pit and Q prospect are similar to initial $^{87}Sr/^{86}Sr$ ratios of sedimentary and metamorphic rocks. The hydrothermal solution associated with Au-mineralization was reacted with sedimentary strata of Carboniferous and/or Permian age in deeper section of the Chatree mining area.
5. The Au-bearing hydrothermal solution was stored in deeper section of the Chatree deposit, under high pressure condition and also reacted with sedimentary strata of Carboniferous and/or Permian age. Then the hydrothermal solution in the deeper

section was intermittently transported to the shallow section as a result of development of fissures. In addition to the presence of a source of gold-bearing hydrothermal fluids, structural control such as the development of fissures from deeper to shallower sections is one of important factors for the formation of Au mineralization in the Chatree deposit,. The source of gold is thought to be andesitic magma.

Acknowledgements

This research could not have been possible without the financial support from the Monbunsho scholarship from the Japanese government since October 2009.

Great acknowledgement goes to my thesis supervisor, Professor Dr. Daizo Ishiyama, for his invaluable supervision and encouragement. His inspiration on scientific thinking is greatly appreciated. I am highly indebted to my thesis co-supervisor, Professor Dr. Osamu Matsubaya, for his invaluable advises and experience, especially on the oxygen isotope theories and technical experiment. Special recognition and thanks to Professor Dr. Toshio Mizuta for his invaluable advises. Also, I wish to acknowledge my former supervisor during undergraduate studies, Professor Dr. Punya Charusiri of the Department of Geology, Chulalongkorn University, for his consistent and invaluable help.

Acknowledgement is also made to Mr. Kyoji Sasaki of Akita University, for his technical support and introducing me to Akita life.

Special thanks go to the Issara Mining Co., Ltd exploration team and Akara Mining Co., Ltd team, for immense support during fieldwork in Thailand. Also, thanks go to Mr. Weerasak Lunwongsa, Mrs. Saranya Nuanla-ong and Miss Sasikan Janplook for their support and making me feel welcomed during my stayin Thailand.

Last but not the least, I would like to thank friends and my family. Mother, father, brothers and sister have given me with support and motivation through very trying times, and still do.

References

Barr, S. M and Macdonald, A. S. (1987) Nan River Suture Zone, northern Thailand. Geodesy, 15, 970-910.

Bence, A. F. and Albee, A. L. (1968) Empirical correction factors for the electron microanalysis of silicates and oxides. Jour. Geol., 76, 382-403.

Boyton, W. V. (1984) Geochemistry of the rare earth elements: meteorite studies. In: Henderson P. (ed.), Rare earth element geochemistry. Elsevier, 63-114.

Bunopas, S. and Vella, P. (1983) Tectonic and geologic evolution of Thailand. In: Nutalaya, P. (ed.), Proc. of the Workshop on Stratigraphic Correlation of Thailand and Malaysia. Geological Society of Thailand and Geological Society of Malaysia, 8th – 10th Sept., 1983, 212-232.

Charusiri, P., Daorerk, V., Archibald, D., Hisada, K. and Ampaiwan, T. (2002) Geotectonic evolution of Thailand: A new synthesis. Jour. Geol. Soc. Thailand, 1, 1-20.

Cumming, G.V. (2006) Volcanic facies architecture of the northern Chatree volcanic complex, central Thailand. A report prepared for Kingsgate Consolidated Limited., Report 4, 2006, 22.

Crossing, J. (2004) Geology of the Chatree District, Thailand, Unpublished technical report, Kingsgate Limited, 81p.

Cumming, G. V., James, R., Salam, A., Zaw, K., Meffre, S., Lunwongsa, W. and Nuanla-Ong, S. (2008) Geology and mineralisation of the Chatree epithermal Au-Ag deposit, Phetchabun and Phichit Provinces, central Thailand. PACRIM Congress 2008, 24th -

26th Nov., Extended Abstracts, Australian Institute of Mining and Metallurgy, Gold Coast, Australia, November, 409-416.

DePaolo, D. J. and Ingram, B. L. (1985) High-resolution stratigraphy with strontium isotopes. Science, 227, 938-941.

Diermar, M.G. and Diemar, V. A. (1999) Geology of the Chatree epithermal gold deposit, Thailand. Proceedings of the PACRIM' 99 International Congress, Bali, 11-13 October. 227-231.

Diemar, M. G., Diemar, V. and Udompornvirat, S. (2000) The Chatree epithermal gold-silver deposit, Phichit-Phetchabun Provinces, Thailand. In Symposium on Mineral, Energy, and Water Resources of Thailand, Toward the Year 2000, Bangkok, Oct., 227-231.

Dong, G., Morrison, G. and Jaireth, S. (1995) Quartz texture in epithermal veins, Queensland; classification, origin and implication. Econ. Geol., 90, 1841-1856.

DMR (Department of Mineral Resources) (1976) Geological Map of Phetchabun Area, Scale 1:250,000, Geological Survey Division. Department of Mineral Resources, Bangkok, Thailand.

Fontaine, H., Suteethorn, V. and Jongkanjanasoontorn, Y. (1991) Carboniferous corals of Thailand. CCOP Technical Bulletin, 22, 1-82

Fricke, H. C. and O'Neil, J. R. (1999) The correlation between $^{18}O/^{16}O$ ratios of meteoric water and surface temperature: Its use in investigating terrestrial climate change over geologic time. Earth Planet. Sci. Lett., 170, 181-191.

Gatinsky, Y. G., Mishima, A. V., Vinogradow, I. V. and Kovalev, A. A. (1978) The main metallognenic belts of Southeast Asia as a result of different geodynamic conditions

interference. In: Natalaya, P. (Ed.), Proceedings of the Third Regional Conference on Geology and Mineral Resources of Southeas Asia. Bangkok, AIT.

Grunow, A., Hanson, R. and Wilson, T. (1996) Were aspects of Pan-African deformation linked to lapetus opening. Geol., 24, 1063-1066.

Henley, R. W. and Ellis, A. J. (1983) Geothermal Systems, Ancient and Modern: a geological review. Earth Sci. Rev., 19, 50p.

Henley, R. W. (1984) Hydrolysis Reactions In Hydrothermal Fluids (ed.). Fluid-Mineral Equilibria in Hydrothermal Systems. Rev. Econ. Geol., 1, 65-82.

Hill, R. (2004) Interpretation of Aeromagneitc data, Thailand, Unpublished report, Kingsgate Limited, 53.

Hosono, T., Nakano, T. and Murakami, H. (2003) Sr-Nd-Pb isotopic compositions of volcanic rocks around the Hishikari gold deposit, southwest Japan: implications for the contribution of a felsic lower crust. Chem. Geol., 201, 19-36.

Ishikawa, Y., Sawaguchi, T., Iwaya, S. and Horiuchi, M. (1976) Delineation of prospecting targets for Kuroko deposits based on modes of volcanism of underlying dacite and alteration haloes, Mining Geology, 26, 105-117.

Hutchinson, C. S. (1989) Geology evolution of Southeast Asia, Oxford Monographs on Geology and Geophysics, No. 13, Oxford University, 368.

Inoue, A. (1995) Formation of clay minerals in hydrothermal environments. In Velde, B. (ed.), Origin and Mineral of Clays, Springer, Berlin Heidelverg New York, 268-329.

Intasopa, S. and Dunn, T. (1994) Petrography and Sr-Nd isotope systems of the basalts and rhyolites, Loei, Thailand. Jour. Southeast Asian Earth Sci., 9, 67-180.

Jame, R. and Cumming, G. V. (2010) Geology and mineralization of the Chatree epithermal Au-Ag deposit, Phetchabun province, central Thailand. GEOTHAI'07 International

Conference on Geology of Thailand: Towards sustainable development and sufficiency economic, Thailand, 378-390.

Johnson, J. W., Oelkers, E. H. and Helgeson, H. C. (1992) SUPCRT92: a software package for calculating the standard molar thermodynamic properties of minerals gases, aqueous species, and reactions from 1 to 5000 bar and 0 to 1000^{0}C. Computers & Geosciences, 18, 899-947.

Jungyusuk, N. and Khositanont, S. (1992) Volcanic rocks and associated mineralization in Thailand. Potential for future development, National conference on geologic resource of Thailand,17th - 24th Nov., 1992, Dept. Min. Res., Bangkok, 522-538.

Keenan, J. H., Keyes, F. G., Hill, P. G. and Moore, J. G. (1969) Steam table - Thermodynamic properties of water including vapor, liquid and solid phases (International edition – metric units). New York, John Wiley & Sons, Inc., 162p.

Kita, I. and Matsubaya, O. (1983) F_2-technique for the oxygen isotopic analysis of silica minerals. Rep. Res. Inst. Nat Resour. Min. Coll. Akita Univ., 48, 25-33.

Large, R. R., Gemmell, J. B. and Paulick, H. (2001) The alteration box plot: A simple approach to understanding the relationship between alteration mineralogy and lithogechemistry associated with volcanic-hosted massive sulfide deposits. Econ. Geol., 96, 957-971.

Lunwongsa, W., Garman, M., Davidson, F. and Circosta, G. (2010) Geology and mineralization model of the Chatree Epithermal Au-Ag deposit, Pichit-Phetchabun Province, central Thailand. Extended abstracts of Thai-Lao Technical Conference on Geology and Mineral Resource, 7th-8th Sep., Department of Mineral Resources of Thailand, Bangkok, Thailand, 1-13.

Marhotorn, S., Mizuta, T., Ishiyama, D., Takashima, I., Krit-Wonin, Nuanlaong, S. and Charusiri, P. (2008) Petrochemistry of igneous rocks in the southern parts of the Chatree gold mine, Pichit, Central Thailand. Proceedings of the International Symposia on Geoscience Resources and Environments of Asia Terranes (GREAT 2008), 4th IGCP 516, and 5th APSEG, 24th – 26th Nov., 2008, Bangkok, Thailand, 289-298.

Matsuhisa, Y., Goldsmith, J. R. and Clayton, R. N. (1979) Oxygen isotopic fractionation in the system quartz-albite-anorthite-water. Geochim. Cosmochim. Acta, 43, 1131-1140.

Metcalfe, I., Spiller, F.C.P, Benpei, L., Haoruo, W. and Sashida, K., (1999) The Paleo-Tethys in Mainland East and Southeast Asia: Contribution from radiolarian studies. Gonwana Dispersion and Asian Accretion, p. 259-280.

Metcalfe, I. (2006) Paleozoic and Mesozoic tectonic evolution and palaeogeography of East Asian crustal fragments: The Korean Peninsula in context. Gondwana Research, 9, 24-46

Na, C. K., Nakano, T., Tazawa, K., Sakagawa, M. and Ito, T. (1995) A systematic and practical method of liquid chromatography for the determination of Sr and Nd isotopic ratios and REE concentrations in geological samples. Chemical Geol., 123, 225-237.

Mizuta, T., Mori, Y., Fukushima, M., Ishiyama, D., Yoshida, H. and Charusiri, P. (2009) Geochemical characteristics of Chatree epithermal vein-type gold-silver deposit, Phetchabun Province, central Thailand. Abstract of annual meeting of Society of Resource Geology , 24th – 26th June., 2009, Tokyo, Japan, 29-30.

Mori, Y. (2009) Mineralization of the Chatree epithermal vein-type gold-silver deposit, and geochemical characteristics of their related igneous rock, central Thailand. Unpublished master thesis, , Akita University, 200p.

Morishita, Y. and Nakano, T. (2008) Role of basement in epithermal deposit: The Kushikino and Hishikari gold deposits, southwestern Japan. Ore Geology Reviews, 34, 597-609.

Panjasawatwong, Y., Zaw, K, Chantaramee, C., Limtrakun, P. and Pirarai, K. (2006) Geochemistry and tectonic setting of the central Loei volcanic rocks, Pak Chom area, Loei, northeastern Thailand. J. of Asian Earth Sci., 26, 77-90.

Roedder, E. (1984) Fluid Inclusions: Mineralogical Society of America, Reviews in Mineralogy, 12p.

Salam, A., Zaw, K., Meffre, S., James, R., Stein, H. and Vasconcelos, P. (2007) Geological setting, mineralization and geochronology of Chatree epithermal gold-silver deposit, Phetchabun province, central Thailand. In Proceedings of Asia Oceania Geosciences Society (AOGS), 4th Annual meeting, 3th – 4th Aug., 2007, Bangkok, 249.

Salam, A., Zaw, K., Meffre, S., Golding, S., McPhie, J., Suphananthi, S. and James, R. (2008) Mineralisation and oxygen isotope zonation of Chatree epithermal gold-silver deposit, Phetchabun province, central Thailand. PACRIM Congress 2008, 24th – 26th Nov., 2008, Gold Coast, Queensland, 123-131.

Salam, A., Zaw, K., Meffre, S., McPhie, J. and Chun-Kit, L. (2013) Geochemistry and geochronology of the Chatree epithermal gold-silver deposit: Implications for the tectonic setting of the Loei Fold Belt, central Thailand. Gondwana Research, 21p.

Satoh, H., Ishiyama, D. Mizuta, T. and Ishikawa Y. (1999) Rare earth element analysis of rock thermal water samples by inductively coupled plasma mass spectrometry (ICP-

MS). Scientific and Technical Reports Faculty of Engineering and Resource Geology, Akita University, Japan, 20, 8p.

Sera, K. and Yanagisawa, T. (1992) Bio-PIXE at the Takizawa facility (Bio-PIXE with a baby cyclotron). Jour. PIXE, 2, 325-330.

Shimizu, T., Matsueda, H., Ishiyama, D. and Matsubaya, O. (1998) Genesis of epithermal Au-Ag mineralization of the Koryu mine, Hokkaido, Japan. Econ. Geol., 93, 303-325.

Sourirajan, S., and Kennedy, G.C. (1962) The system H_2O-NaCl at elevated temperatures and pressures: American Journal of Science, v. 260, 115-141.

Tangwattananukul, L., Ishiyama, D., Matsubaya, O., Mizuta, T., Charusiri, P., Sato, H. and Sera, K. (2014) Characteristics of Triassic epithermal Au mineralization at the Q prospect, Chatree mining area, Central Thailand. Resour. Geol., 64, 164-181.

Taylor, H. P., Jr. (1971) Oxygen isotope evidence of large-scale interaction between meteoric ground waters and Tertiary granodiorite intrusions, western Cascade Range, Oregon. Jour. Geophy. Res., 76, 7855-7874.

Truesdell, A.H., Nathenson, M. and Rye, R. O. (1977) The effects of subsurface boiling and dilution on the isotopic compositions of Yellowstone thermal waters: Jour. Geophy. Res., 80, 3694-3704.

White, N. C. and Hedenquist, J. W. (1995) Epithermal gold deposit: styles, characteristics and exploration. SEG Newsletter, 23, 1, 9-13.

Zaw, K. and Meffre, S. (2007) Metallogenic relations and deposits scale studies, final report, Geochronology, Metallogenesis and Deposit Styles of Loei Fold Belt in Thailand and Laos PDR, ARC Linkage Project.